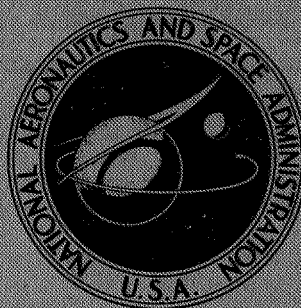


N74-10019

**NASA CONTRACTOR
REPORT**



NASA CR-2344

NASA CR-2344

**CASE FILE
COPY**

**THE EFFECTS OF LEADING-EDGE SERRATIONS
ON REDUCING FLOW UNSTEADINESS
ABOUT AIRFOILS - AN EXPERIMENTAL
AND ANALYTICAL INVESTIGATION**

by R. G. Schwind and H. J. Allen

Prepared by

NIELSEN ENGINEERING & RESEARCH, INC.

Mountain View, Calif. 94040

for Ames Research Center

NATIONAL AERONAUTICS AND SPACE ADMINISTRATION • WASHINGTON, D. C. • NOVEMBER 1973

1. Report No. NASA CR-2344	2. Government Accession No.	3. Recipient's Catalog No.	
4. Title and Subtitle "The Effects of Leading-Edge Serrations on Reducing Flow Unsteadiness About Airfoils - An Experimental and Analytical Investigation"		5. Report Date November 1973	
		6. Performing Organization Code	
7. Author(s) R. G. Schwind and H. J. Allen		8. Performing Organization Report No.	
9. Performing Organization Name and Address Nielsen Engineering and Research, Inc. 850 Maude Avenue Mountain View, California 94040		10. Work Unit No.	
		11. Contract or Grant No. NAS 2-6010	
12. Sponsoring Agency Name and Address National Aeronautics & Space Administration Washington, D.C. 20546		13. Type of Report and Period Covered Final Report Contractor Report	
		14. Sponsoring Agency Code	
15. Supplementary Notes			
16. Abstract <p>High frequency surface pressure measurements were obtained from wind-tunnel tests over the Reynolds number range $1.2 \cdot 10^6$ to $6.2 \cdot 10^6$ on a rectangular wing of NACA 63-009 airfoil section. Measurements were also obtained with a wide selection of leading-edge serrations added to the basic airfoil. Under a two-dimensional laminar bubble very close to the leading edge of the basic airfoil there is a large apatial peak in rms pressure. Frequency analysis of the pressure signals in this region show a large, high-frequency energy peak which is interpreted as an oscillation in size and position of the bubble. The serrations divide the bubble into segments and reduce the peak rms pressures. A low Reynolds number flow visualization test on a hydrofoil in water was also conducted. A von Karman vortex street was found trailing from the rear of the foil. Its frequency is at a much lower Strouhal number than in the high Reynolds number experiment, and is related to the trailing-edge and boundary-layer thicknesses.</p>			
17. Key Words (Suggested by Author(s)) Leading-edge serration Airfoils; Laminar bubble Aerodynamic noise Surface pressure fluctuations		18. Distribution Statement UNCLASSIFIED-UNLIMITED	
19. Security Classif. (of this report) UNCLASSIFIED	20. Security Classif. (of this page) UNCLASSIFIED	21. No. of Pages 97	22. Price* Domestic, \$3.75 Foreign, \$6.25

* For sale by the National Technical Information Service, Springfield, Virginia 22151

TABLE OF CONTENTS

	Page No.
SUMMARY	1
1. INTRODUCTION	2
2. SYMBOLS	4
3. PAST INVESTIGATIONS OF SERRATED-EDGE EFFECTS	5
4. APPARATUS	7
4.1 Model and Serrated Edges	7
4.2 Transducers and Instrumentation	10
4.3 Procedures	11
5. EXPERIMENTAL RESULTS FOR HIGH REYNOLDS NUMBER FLOWS	12
5.1 Basic Airfoil Lift, Drag, and Stall	12
5.2 General Tests of Twelve Serrations	13
5.3 Airfoil Static Pressure Distributions	14
5.4 Surface Flow Visualization	15
5.5 Airfoil Surface Pressure Fluctuations	16
5.6 Frequency Analysis of Surface Pressure Fluctuations	19
5.7 Summary of Wind-Tunnel Results	21
6. THEORY AND EXPERIMENT FOR LOW REYNOLDS NUMBER FLOWS	22
6.1 With No Leading-Edge Serrations	22
6.2 With Leading-Edge Serrations	27
6.3 Summary of Low Reynolds Number Flow Results	28
7. THEORY FOR HIGH REYNOLDS NUMBER FLOWS	29
7.1 Strouhal Number Comparison	29
7.2 First Hypothesis	30
7.3 Second Hypothesis	30
7.4 Summary of High Reynolds Number Flow Theory	35
8. LEADING-EDGE REGION FLOW GEOMETRY CAUSED BY SERRATIONS	36
8.1 Introduction	36
8.2 Construction of the Local Flow Geometry	37
8.3 Summary of the Leading-Edge Region Flow Description	40
9. CONCLUDING REMARKS	40
APPENDIX - DEFINITIONS OF STATISTICAL FUNCTIONS	42
REFERENCES	44
TABLES I THROUGH VII	45
FIGURES 1 THROUGH 49	53

THE EFFECTS OF LEADING-EDGE SERRATIONS ON
REDUCING FLOW UNSTEADINESS ABOUT AIRFOILS -
AN EXPERIMENTAL AND ANALYTICAL INVESTIGATION

By R. G. Schwind and H. J. Allen*
Nielsen Engineering & Research, Inc.

SUMMARY

The purpose of the present investigation has been to study the surface flow on an airfoil, with and without serrated edges, and to attempt explanations of the flow mechanisms involved in both cases. A 0.9144-meter (3-foot) chord by 1.524-meter (5-foot) span rectangular wing with an NACA 63-009 airfoil section was tested in the Ames Research Center 7- by 10-Foot Wind Tunnel No. 1 over the Reynolds number range 1.2×10^6 to 6.2×10^6 . The basic configuration was modified with the addition of small serrated edges of various design to the pressure side of the airfoil near the leading edge. In addition to standard wind-tunnel instrumentation, surface flow visualization techniques and high-frequency-response pressure transducers which sensed surface pressure fluctuations were used in the tests.

For the basic airfoil, surface flow visualization showed a two-dimensional laminar bubble which moved forward toward the leading edge with increasing angle of attack. The serrated edges divided the bubble into segments of the same width as the serration tooth spacing. A three-dimensional separated flow is proposed to explain the steady bubble pattern which involves the interaction of trailing vortex pairs streaming from each serration tooth with the boundary layer.

Under the bubble there is a large peak in the root-mean-square pressure fluctuation versus chordwise position. This peak decays over a distance of several bubble lengths. Frequency analysis of the pressure fluctuations show a high-frequency peak in the spectra, the intensity of the peak also decaying with distance from the average position of the bubble. This evidence indicates, it is believed, that the bubble is oscillating in size and position. A quasi-steady hypothesis is proposed to explain the motion of the two-dimensional bubble for high Reynolds number flows. The most effective serrated edge reduced the largest peak intensity of the root-mean-

*Consultant to Nielsen Engineering & Research, Inc.

square pressure coefficient from 0.41 to 0.24 at $Re = 1.75 \times 10^6$ and an angle of attack of 8° . For the serrated edges tested, there was a clear correlation of tooth spacing upon pressure fluctuations.

A low Reynolds number flow visualization experiment was performed using a 6.7-percent thick hydrofoil towed through calm water. A von Karman vortex street was found trailing from the rear of the airfoil, and this was directly related to the laminar bubble oscillations, which were of the same frequency. A theory, which is in agreement with experiment, is proposed for predicting the frequency of this oscillation for the low Reynolds number flow case. It relates the vortex shedding frequency to the airfoil trailing edge thickness and upper and lower surface boundary-layer thicknesses.

1. INTRODUCTION

In reference 1, Hertel discusses, among other things, the quiet flight of owls. He explains that the phenomenon is due to (a) the downy feathers on owls, and (b) the rake on the leading edge of the first (and sometimes the first two) feathers on the owl's wing, apparently unique with these birds. The first argument is reasonable, but the second seemed a matter of conjecture since Hertel presented no actual evidence to support this contention. At the suggestion of one of the authors (H. J. A.), Mr. Paul Soderman of the Ames Research Center tested serrated leading edges on a propeller and on an airfoil for changes in radiated noise and in lift-drag characteristics. The results showed, indeed, that a rake on the propeller did reduce the radiated noise, mainly by eliminating one pronounced tone in the energy spectrum (ref. 2). Wind-tunnel tests showed a considerable increase in maximum lift (ref. 3). These results and other research of the owl wing effects are reviewed in section 3.

Following these preliminary experiments, Bolt, Beranek & Newman, Inc., of Canoga Park, California, under contract to the Ames Research Center, made further definitive experiments in their acoustic wind tunnel. Results of this investigation, reported by Herish and Hayden (ref. 4), showed that with a rake of suitable dimension located close to the stagnation point on an airfoil and on a propeller, dramatic reductions in the intensity of emitted noise were achieved, again at particular tones of the spectrum.

Both of the previous tests involving radiated noise measurements were conducted at low Reynolds numbers where laminar boundary layers would be expected. The present investigation has been conducted at higher Reynolds numbers where a turbulent boundary layer was to be expected on the aft surfaces of the wing. Its purpose has been to determine the effect of the serrations on the fluid flow at the surface of a wing and to attempt an explanation of the mechanisms by which the serrations modify the flow over the airfoil and thus, the stall and acoustic characteristics of the airfoil. For this purpose, a wing was designed, instrumented, and tested in the Ames 7- by 10-Foot Wind Tunnel No. 1. Data have been obtained from high-frequency-response pressure transducers, static pressure taps, surface-flow visualization, and the lift and drag determined from the wind-tunnel scales to aid in defining the flow characteristics. Various serrated edge configurations and locations were used in an attempt to optimize the shape and location of a serrated leading edge. The apparatus and procedure of these tests are presented in section 4 and the results in section 5.

To visualize the flow about an airfoil, the second author performed an originally unplanned second experiment using water. These tests are described in section 6 along with a theoretical explanation for the unsteady flows near an airfoil that led to peaks in the radiated noise in previous low-Reynolds-number flow experiments. A boundary layer-laminar bubble interaction is described in section 7 to explain a mechanism for the observed unsteady flows at high Reynolds numbers. These two sections are a condensation of the work reported in reference 5. A construction of the flow interaction between the serrated edges and separation bubble is given in section 8.

The assistance of Mr. Richard D. Hanly, Aeronautical Structures Branch, is gratefully acknowledged for installation and calibration of the pressure transducers and the associated data acquisition system. This effort was essential to the success of the experiment.

2. SYMBOLS

c	chord, meters (feet)
c_l	section lift coefficient
C_p	pressure coefficient, $(p - p_\infty)/\frac{1}{2} \rho V_o^2$
C_D	drag coefficient
C_L	lift coefficient
d	diameter of a circular cylinder, meters (feet)
d'	distance between the rows of vortices shed from trailing edge of airfoil, meters (feet)
dB	decibel
f	frequency, Hz
G_x	power spectral density function (see Appendix)
h	maximum displacement thickness of a separation bubble
k	constant which with Reynolds number defines the boundary-layer contribution to the width of the trailing vortex street, dimensionless
p	local pressure, kilograms/meter ² (lbs/ft ²)
p_∞	free-stream pressure, kilograms/meter ² (lbs/ft ²)
q	dynamic pressure, kilograms/meter ² (lbs/ft ²)
$r_{l.e.}$	leading-edge radius of the airfoil, meters (feet)
Re	Reynolds number ($V_o c/\nu$)
RMS C_p	root mean square of C_p fluctuations about the mean value
s	wing semispan, meters (feet)
S	Strouhal number (fc/V_o or fd/V_o)
S^*	universal Strouhal number of the wake
V_a	additional velocity determined by the lift coefficient, meter/sec (feet/sec)
V_c	narrow band convection velocity, meter/sec (ft/sec)

V_f	velocity on the basic profile, meters/sec (ft/sec)
V_L	lower surface velocity, meters/sec (ft/sec)
V_S	velocity at separation, meters/sec (ft/sec)
$V_{t.e.}$	trailing-edge velocity outside the boundary layer, meters/sec (ft/sec)
$V'_{t.e.}$	effective velocity at the trailing edge within the boundary layer, meters/sec (ft/sec)
V_U	upper surface velocity, meters/sec (ft/sec)
V_V	velocity of the vortices in the vortex street, meters/sec (ft/sec)
V_O	stream velocity, meters/sec (ft/sec)
x	length measured along the chord, meters (feet)
x_a	position at the end of separation bubble (reattachment), meters (feet)
x_s	position of separation, meters (feet)
x_t	position of transition, meters (feet)
y	ordinate to airfoil surface measured normal to the chord, meters (feet)
$y_{t.e.}$	half the trailing-edge thickness, meters (feet)
β	angle of attack of leading-edge serration, with respect to airfoil centerline
γ	coherence function (see Appendix)
δ^*	boundary-layer displacement thickness, meters (feet)
θ	phase angle
λ	length of a separation bubble, meters (feet)
ν	kinematic viscosity, meter ² /sec (ft ² /sec)
ρ	density, kilograms/meter ³ (slugs/ft ³)

3. PAST INVESTIGATIONS OF SERRATED-EDGE EFFECTS

Soderman (ref. 2) measured radiated noise from two helicopter rotors operating in hover condition with various serrations attached on the lower surface between the stagnation point, when at a positive angle of attack,

and the leading edge. The small-scale rotor, 1.52 meters (5.0 feet) in diameter, had an NACA 0012 airfoil section, and the larger rotor of 2.59 meters (8.5 feet) diameter had an NACA 0015 section. (Meter, centimeter, foot, and inch are abbreviated m, cm, ft, and in, respectively.) The rotors were operated at speeds up to 1440 rpm for Reynolds number $Re = 0.55 \times 10^6$, and to 1600 rpm for $Re = 3.18 \times 10^6$, respectively. With the serrated edges the smaller rotor acoustic performance improved greatly, particularly in the higher octave bands (up to 17 dB less noise radiation) but only a small improvement occurred for the larger rotor. Aerodynamic performance was essentially unchanged.

Soderman then tested an NACA 66-012 airfoil in the Ames Research Center 7- by 10-Foot Wind Tunnel (ref. 3), the same tunnel as used for the present tests. It had a 0.762 m (30 in) chord and 1.016 m (40 in) span with large end plates attached. However, even with these plates there was still a considerable amount of premature separation on the airfoil near them at the higher lift coefficients. Various combinations of 14 serrations were tested in four positions between the stagnation point at an angle of attack and the leading edge. A wide range of serration geometry was included, the height varying from 0.127 cm (0.05 in) to 0.94 cm (0.37 in) and the spacing between the tips, from 0.254 cm (0.1 in) to 4.06 cm (1.6 in). The effects of the serrations ranged from as much as a 10-percent decrease in maximum lift to a 21-percent increase. The increase was created by delaying stall. Lift and drag were measured using the tunnel scales, and the tare for end-plate drag was deducted. A serration with 0.254 cm (0.1 in) height and 0.508 cm (0.2 in) spacing produced the best improvement. The results were very sensitive to the location of the serrated edge. Soderman also performed flow visualization using titanium dioxide painted on the wing. Alternate light and dark bands were etched in the oil behind each prong of the serration from the airfoil leading edge toward the trailing edge. The Reynolds number for this study varied between 1.0×10^6 and 2.3×10^6 .

As part of a study on aerodynamic sound radiation from lifting surfaces, Hersch and Hayden (ref. 4) tested an NACA 0012 airfoil of 15.2 cm (6 in) chord by 76.2 cm (30 in) span in the Bolt, Beranek & Newman free jet acoustic wind tunnel for $Re = 0.2 \times 10^6$ to 0.33×10^6 . Four serrated edges were tested in several positions. Again, the radiated sound was very sensitive to size and location of the edges. The best edge was the largest with a tip height of

0.169 cm (0.0665 in) and the spacing of 0.338 cm (0.133 in). For the basic airfoil (no serration) there was a peak in the radiated acoustic power spectrum of 85 dB at 1.7 KHz between angles of attack of 0° and 8° . The best serration reduced this peak at 0° , 4° , and 8° by 11, 30, and 24 dB, respectively. From acoustic measurements at 0.083×10^6 Reynolds number, a dipole source of acoustic power was found to be located at the airfoil trailing edge. Hot wire measurements in the airfoil wake located two spatial peaks in turbulence energy just as if von Karman vortex pairs were being shed from the airfoil. The authors concluded that the peaks in the energy spectra are generated by periodic, or near-periodic, fluctuating forces located on the airfoil near the trailing edge and induced by laminar wake vortex shedding. They curve fitted the Strouhal number S , based on airfoil thickness, of these tones with the expression $S = 0.6 \log (Re) - 2.35$.

Propeller tests were made in the same free jet acoustic wind tunnel using the same shape airfoil with a 5.08 cm (2 in) chord and 35.6 cm (14 in) diameter over the Reynolds number range 0.11×10^6 to 0.22×10^6 . Again, the energy spectrum showed a large peak, and the serrated edges reduced this peak by as much as 18 dB. The characteristic frequencies also fit the above expression. Pertinent data on airfoil shapes and dimensions, test conditions, and the Strouhal numbers based on the frequency of the peaks in the energy spectra are given in Table I.

4. APPARATUS

4.1 Model and Serrated Edges

A survey of aerodynamic data was made in order to select a suitable test airfoil for this study. An airfoil section typical of those in current use and for which test data on pressure distributions and boundary layers are available was considered desirable. Gault (ref. 6) gives very detailed measurements on a two-dimensional NACA 63-009 airfoil section, and this shape was selected for the tests. Thirteen pressure taps were located in the first one percent of the chord of Gault's airfoil. Pressure probe traverses were made in this region to obtain boundary-layer velocity profiles and the shape of a laminar separated bubble at six angles of attack with section lift coefficients between 0.48 and 1.02. The latter value is immediately before stall. McCullough and Gault (ref. 7) made

further measurements on the same airfoil at the same Reynolds number of 5.8×10^6 . Both tests were in the same wind tunnel as the present tests. The mechanism by which the serrated edge affects the flow over the airfoil is thought to be intimately connected with the behavior of the laminar bubble.

Coordinates and V_a/V_o , the additional velocity ratio due to lift for the NACA 63-009 airfoil are given in Table II. This is a combination of the data in Abbott and von Doenhoff (ref. 8) and additional data for the leading-edge region, which are derived in reference 5.

A 0.9144 m (3 ft) chord was selected so as to have adequate space in a leading-edge region for instrumentation. Since it was desired to design a model that could be operated in the future in more than one wind tunnel, a semispan configuration was selected. Load limitations on the semispan mounting arrangement dictated a span of 1.524 m (5 ft). The model, mounted in the Ames Research Center 7- by 10-Foot Wind Tunnel No. 1, is shown in figure 1. End plates extend 0.6096 m (2 ft) out each side of the airfoil at the bottom and have the same chord as the airfoil. These plates were mounted to the airfoil 10.17 cm (4 in) above the wall. On the upper surface they have the same shape as the airfoil, and the bottom is flat except near the leading edge. The top end of the airfoil was capped with a half round section with a radius distribution the same as the airfoil half-thickness distribution. The airfoil was machined from aluminum in two halves, split on the centerline to 69.5 percent of the chord. Channels were cut out for instrumentation and pressure tubing. Since this airfoil tapers to a knife edge the last 0.61 cm (0.24 in) were removed so the trailing-edge thickness is 0.048 cm (0.019 in). The surface was polished to approximately a 16 micro finish. However, this finish was somewhat degraded locally by slight corrosion around some of the pressure taps.

The serrated edges tested are shown in figure 2. The designs were selected based on Soderman's results (ref. 3). Shapes both larger and smaller than his optimum were selected and fabricated of the same material, 0.025 cm (0.010 in) brass shim stock. Soderman also found that the results were very sensitive to serration position. He attached the serrations in any one of four positions to the model with wood screws. To speed the process of finding any optimum position, the serrated edges were mounted in a 0.795 cm (0.3125 in) diameter rotatable brass rod. This rod was embedded in the lower surface of the airfoil as shown in figure 3. Running the full

length of the rod is a 0.030 cm slot. The serrated edges were placed into the slot and slid down over pins in the rod every 7.62 cm (3 in) that locked into cut-outs on the back side of the serrated edges. The rod was driven remotely by a small gear motor located under the tunnel and its angle sensed by a precision potentiometer. For the bent edges, most testing was done with the serration in the most forward position in figure 3. The most rearward position is shown dotted. Unless otherwise indicated in the results, the serration angle is for this most forward position with $\beta = 38^\circ$ for the bent serrated edges (patterns A and B). Since serration position is important, the rod position was carefully selected to place the tips of the serrated edge most like the serration Soderman found best in the same part of the pressure field where he got his best results. The stagnation point is on the undersurface downstream of the serrations even when they are rotated into the most rearward position at an airfoil angle of attack as low as 3° , based on the measurements of the stagnation point in reference 7. For the basic airfoil condition, grooves cut out around the serration rod were filled with wax and smoothed and shaped with a template. Three straight serrated edges were also tested. The angle they made to the airfoil chord, β , is indicated in the results of tests performed with them.

A total of 78 pressure taps were located in rows at 40, 65, and 85 percent of the semispan with nearly half of these at the 40-percent location, the major instrumentation position. A total of 25 pressure transducers were located in rows 2.03 cm (0.80 in) inboard of the pressure tap rows and several more were placed between the two rows. The spanwise spacing between the rows of pressure transducers and pressure taps was chosen to be a multiple of the basic unit of 0.508 cm (0.2 in) for the serration tip spacing. Earlier experience in pressure transducer mounting holes was followed, and dimensions are shown in figure 3. Because of the fine holes and close tolerances, the holes were drilled into small inserts and these mounted into the airfoil before final finishing. A close-up of the suction-side leading edge at the 40-percent span region is shown in figure 4. A serrated edge in the most forward position shows in the photograph, but because of the lighting the tips appear as pointed voids, and the shiny segmented line between these is the edge of the base between the serrations.

4.2 Transducers and Instrumentation

Pressure lines conducted the surface static pressures to a manometer board where the values were recorded on film. The miniature differential pressure transducers are manufactured by Kulite Semiconductor Products, Inc. The model used, XC QL7-093-4, has a nominal sensitivity of 55 millivolts per psi at 20 volts excitation and a natural frequency of 65 KHz. The reference pressure tube at the rear of the transducer was connected through at least three meters of 0.159 cm (1/16 in) tubing to the static tap at the same chordwise position.

Two accelerometers, Endevco Model 2264-150 with nominal sensitivity of 2.6 millivolt/g and flat response with no phase shift to 800 Hz were mounted in the model at the 85-percent span station, one at 35.7 percent of the chord near the calculated torsional axis, and the other at 67.7 percent of the chord.

Three strain gages were mounted below the end plate immediately above the tunnel balance support brackets at the 36.4-percent chord location. One gage was of the foil type and the other two were semiconductors. One of the latter was installed to measure pitching moment strain about the torsional axis of the airfoil, and the other two strain gages sensed the root bending moment of the airfoil. Unfortunately, no high stress area was accessible for mounting the gages, and 90 percent of the testing was performed with less than 100 μcm per cm strain in bending at the gages. This small strain limited the accuracy of the signals obtained.

The signals from the pressure transducers, accelerometers, and strain gages were amplified and recorded on the data acquisition system of the Aircraft Structures Branch of the Ames Research Center. Their sophisticated apparatus, shown in figure 5, automatically sets the gain amplitude and records the calibration signal gain, a calibration sine wave, and the test signal in a preprogrammed routine. For all signals except the foil strain gage, ac amplification was used. The signals were recorded on an Ampex Model FR-1800 32-channel fm tape recorder operating with double bandwidth at 60 in/sec.

4.3 Procedures

High pass filters were switched out of the electrical circuit to take advantage of the zero frequency response capability of the pressure instrumentation system for sensitivity calibrations. Checks of the transducer sensitivities were made by applying ± 1 psi gage pressures through the reference pressure tubing before, several times during, and after the test program. The calibrations were very stable. Laboratory checks of the transducers prior to model installation showed that thermal effects on the sensitivity could be expected to be less than 2 percent for the temperature range of the tests. Several pressure transducers broke during the course of tests, apparently by impingement of dirt particles at the higher speeds. Fortunately, past experience had shown that the calibration of the transducers would remain valid to the point where they broke, at which time the signal became very noisy and it was obvious that they were ruined.

During most of the tests, the root-mean-square output from some of the transducers and strain gages were read directly on Disa Model 55-D35 RMS Voltmeters, generally using a 10-second time constant. The bandwidth of these signals was limited by the 50 KHz filters in the amplifiers. After the tests were completed, nearly all of the magnetic tape data were played back and the rms values read. These signal levels were limited in bandwidth by the 20 KHz frequency response limit of the playback electronics.

Two methods of frequency analysis of the pressure fluctuations were performed after the completion of the test program. The first used a Spectral Dynamics Real Time Analyzer Model SD301B set to average the analyses of 256 ensembles. The second method used was the comprehensive combination analog-digital method described by Lim and Cameron in reference 9. This hybrid computing process produces a total of 106 frequency points for spectrum measurement. Cross spectral densities, phase angles, and convection velocities were also obtained. The definitions of these quantities are given in the Appendix.

For both of the above methods of analysis, the frequency response was limited to 20 KHz by the tape playback electronics.

Of three flow visualization methods tried, carbon black and oil, ablation, phosphorescent oil with black light, the last gave superior results at the Reynolds numbers tested. The leading and trailing edges of the

leading-edge separation region generally became well defined in about a minute, long enough so that tunnel starting transients were not bothersome. A photograph would be taken and the angle of attack increased. Some of the fluid in the separation zone would be shed and the remainder would move forward. At the Re of 1.75×10^6 the method worked very well, but at Re of 3.5×10^6 the optimum viscosity was thick grease. The results were reproducible but not considered as reliable as those obtained at the lower Reynolds number. A photograph of a flexible ruler laid around the leading edge at several angles of attack provided the basis for the interpretation of the photographs.

5. EXPERIMENTAL RESULTS FOR HIGH REYNOLDS NUMBER FLOW

5.1 Basic Airfoil Lift, Drag, and Stall

As noted in the previous section, the basic airfoil was obtained by filling in the grooves around the serration rod with wax and smoothing it with a template. Figure 6 shows lift and drag curves for the wing as determined from the tunnel scales at two Reynolds numbers. Values throughout the report are uncorrected for tunnel wall constraint since comparisons are made with section data and with the uncorrected data obtained previously in the same wind tunnel (refs. 6 and 7). With increasing angle of attack, stall occurs abruptly at lift coefficients of 1.02 and 0.88 for Reynolds numbers of 3.5×10^6 and 1.75×10^6 , respectively. The angle of attack at which stall occurs does depend on the time duration at that angle. These values are representative of ones at which one can still obtain data for an unstalled condition which would usually last for at least 1/2 minute. Occasionally the wing would stall at an angle of nearly one degree less. Section lift coefficient at 40-percent span is also shown in figure 6 and is slightly greater than total lift coefficient. The ratio of the section lift to the wing lift coefficient is shown in figure 7 for values at 40-, 65-, and 85-percent semispan, and they are compared with the finite wing theory of reference 10. The theory does not include wind-tunnel wall interference. Since the area under the curve must equal 1.0 for both theoretical and experimental cases, the measured value at 40-percent span appears low.

Static pressure tap pressure coefficient data over 90 percent of the chord at the 40-percent span location are presented in figure 8 for two

Reynolds numbers at an angle of 9.4° . Included in the figure are data from McCullough and Gault, reference 7, presented at the same section lift coefficient of 0.665 obtained by interpolation from their tables.

Photographs of the suction side of the airfoil at 9° , 12° , and 14.1° with tufts taped to the surface are shown in figure 9. The flow is from right to left. At 9° only the bottom trailing-edge corner shows separated flow. The trailing vortex effect shows on the top rear tuft. Over the upper 25 percent of the airfoil there is a modest spanwise component in the flow near the surface. At 12° the stall region has spread across the second row of tufts and possibly a little way into the third row. The fourth row is close to the 40-percent span taps and transducers, and at 14.1° angle of attack, which is just before stall occurred over the entire wing, there is some stall occurring in the fourth row. Flow visualization over the first 2 percent of the chord, presented in section 5.4, shows no noticeable spanwise flow up to 13° angle of attack.

5.2 General Tests of Twelve Serrations

Twelve serrations were tested near the beginning of the test program for their effects on drag and lift, airfoil vibration, moment fluctuations, and pressure fluctuations at the first and fifth pressure transducers, which were located at 0.83- and 3.5-percent chord, respectively. Root-mean-square output from these two pressure transducers, the two accelerometers, and the semiconductor strain gage sensing aerodynamic moment fluctuations were read directly on RMS voltmeters. Composite plots for the effects of the twelve serrations on lift curve, lift-drag curve, the aerodynamic moment RMS, and the first pressure transducer signal RMS are presented in figures 10, 11, 12, and 13, respectively. All curves are for a Reynolds number of 3.5×10^6 . The results are presented in the same order as the serrations are presented in figure 2. The solid line in each plot represents the data for the basic airfoil. The RMS values were limited to minimum and maximum frequencies by the amplifier filters of 10 Hz to 50 KHz for the pressure transducer, and 10 Hz to 5 KHz for the aerodynamic moment strain gage.

Unlike Soderman's results, the serrations generally caused no change in maximum C_L , as seen in figure 10. Only for serration A3-8 is there a possible lift increase of 4 percent, but this could be within the accuracy

for determining the maximum C_L as explained in section 5.1. For serration Al-8, the largest serration tested, there is possibly a 9-percent decrease in maximum lift, but there is only one data point that definitely supports this result. Generally the serrations decrease the severity or eliminate the sudden stall that occurs on the basic airfoil. No definite trend with spacing or serration height is found on the modification of these lift curves in the stalled region. The airfoil drag remains unchanged by the serrations up to the stall limit of the basic airfoil, as noted from figure 11.

Figure 12 shows the effects of the various serrations on the aerodynamic moment RMS signal. Due to the low signal levels, some results show considerable scatter. The strain gages were uncalibrated, but the vertical scale should be linear. There was no response from these gages corresponding to the peak signal from the pressure transducer, which is discussed in the next paragraph. This, however, is related to the low signal cut-off frequency of 5 KHz. Half of the serrations greatly reduced the strain gage signal at higher angles of attack.

Pressure RMS C_p values for the first transducer, which is located at x/c of 0.83 percent, are presented in figure 13. For the basic airfoil there is a very large peak value at $8\text{-}1/2^\circ$ angle of attack, 7.3 times greater (17.3 dB greater) than if the RMS C_p varied linearly between its values at angles of 0° and 13° . All serrations reduced this peak value by one-half to three-fourths of the absolute values and shifted the angle of attack at the peak. A clear correlation with spacing exists and this is shown in figure 14. The basic airfoil is taken to be the case with infinite spacing, so in this plot RMS C_p is plotted versus the inverse of spacing. There is no minimum in the curve so the optimum spacing may be smaller than any tested. A shift in angle of attack for the peak RMS is also shown.

5.3 Airfoil Static Pressure Distributions

As noted in the previous section, the serrations had no effect on the lift curve until near the maximum C_L , and no overall effect on C_p was observed except near the leading edge. Examined in this section are the pressure effects near the leading edge that are caused by Reynolds number variation and by the two serrations tested in considerable detail. Surface pressure coefficient versus chord for the first $3\text{-}1/2$ percent is presented in figure 15 for the basic airfoil for five Reynolds numbers

along with experimental values from McCullough and Gault (ref. 7) and theoretical inviscid flow results from section 6. Peak minimum C_p values occur for the Reynolds number 1.75×10^6 . Downstream of the usual peak in airfoil pressure distributions there are in all cases bumps in the pressure distribution. The position of the bump moves forward with Reynolds number and the deviation from a smooth curve, the "severity" of the bump, appears to be essentially independent of Reynolds number. However, the data from reference 7 show a smaller bump and it is located further downstream than those in the present tests at highest Reynolds number. Three pressure taps at $x/c = 0.0083$ show considerable variation in their values. The bump is associated with a region of leading-edge separation, and the leading and trailing edges of the separation zone from the flow visualization results of the next section are marked on two of the pressure curves.

In figure 16 the effect of two different serrated edges is shown to greatly reduce the pressure bump of the basic airfoil. The pressure distributions have been continued around onto the pressure side of the airfoil toward the stagnation point, and the serration tip positions are indicated. In figure 17 the average of the three pressures at $x/c = 0.0083$ are plotted versus angle of attack for two Reynolds numbers and three configurations: basic, and B1-2 and B3-2 serrations. Generally, the curves deviate from a smooth monotonically increasing curve by an amount approximating a sine wave. The amplitude of this deviation is greatly reduced by the serrations.

5.4 Surface Flow Visualization

Phosphorescent oil and black light surface flow visualization photographs are shown in figures 18 and 19. The flow is from left to right, and the oil shows as white on the black airfoil, which is invisible in these photographs. The vertical white band is the separation bubble, which was stationary, and the oil downstream of it, to the right, was slowly moving downstream. Figure 18 shows representative results at $Re = 1.75 \times 10^6$ for the basic airfoil and with serration B1-2. The position of the leading edge which has been drawn onto the photographs on the left, was determined from other photographs in which the airfoil was visible. For the basic airfoil results are shown for two oils of greatly different

viscosity. There is a moderate difference in the trailing-edge positions of the oil patterns, but the oil in the region of the bubble in the lower half, which has the greater viscosity, has not yet reached equilibrium. The right half of figure 18, and figure 19 show the effects of two serrated edges at two Reynolds numbers. At all angles for both configurations the serration spacing was observed as a pattern imposed on the separation region as oil wiped from the surface in narrow wedges into the separation region from the left and corresponding bumps or trails of oil leaked from the bubbles at the trailing edge of the separation region. This pattern was centered directly downstream from the serration tips. Fluid left the separation region when changing angle of attack by bleeding out through the trailing-edge bump or trail. This was particularly obvious for the serration B2-8 (fig. 19). In fact, bleeding from these points for that serration continued for a long time before equilibrium appeared to be reached.

The influence of the configurations and the angle of attack, or lift coefficient, on the position of the bubble separation and attachment is shown in figure 20. The bubble gradually moves forward almost to the leading edge with increasing α . There appears to be a Reynolds number influence (for the two values tested) only on the separation line for the basic airfoil. The serrations moved the reattachment line forward. The bubble position from the work of Gault, reference 6, is indicated in the figure.

5.5 Airfoil Surface Pressure Fluctuations

For the basic airfoil and serrations B1-2 and B3-2, root-mean-square (RMS) values from the fifteen most significant transducers were determined for a total of 198 test conditions by varying angle of attack and velocity (Reynolds number). The results are presented here. The RMS pressure fluctuations are made dimensionless by the free-stream dynamic head and the resulting pressure coefficient is denoted $RMS C_p$. The $RMS C_p$ is a function of position on the airfoil, angle of attack, Reynolds number, and geometry. The effects of these variables are presented in figures 21 to 28. All data in this section were obtained from tape records, and frequency response is limited to 20 KHz. The data for all curves presented in this section are for the 40-percent spanwise position on the airfoil.

Figures 21 and 22 show $RMS C_p$ versus x/c for the basic airfoil over the first 30 percent of the airfoil chord for various angles of attack for Reynolds numbers of 1.75×10^6 and 3.5×10^6 , respectively. For angles of 0° and greater, there is a significant sharp peak in $RMS C_p$ in the first 2 percent of the airfoil chord. Progressing downstream, usually there is a minimum between 3 and 5 percent of the chord followed by a slight rise and then a minimum $RMS C_p$ at about 20 percent of the chord. Only one pressure transducer was located further downstream that was in working condition; it was at 50-percent chord. In 90 percent of the cases, its $RMS C_p$ readings varied from -15 percent to +50 percent of the $RMS C_p$ values at 30-percent chord, and the average value was a 16-percent increase over that at 30-percent chord. As many transducers as there were located near the leading edge, they were not close enough to define completely the peak in the $RMS C_p$ values, but a reasonable approximation to the maximum can usually be made. This peak is very sensitive to angle of attack. Starting at a high value for an angle of 0° in figure 21, it drops to a minimum at about 2° , then rises again. The effects of angle of attack on $RMS C_p$ are discussed more completely below.

Curves of $RMS C_p$ versus x/c are shown in figures 23 and 24 for an angle of attack of 9° at various Reynolds numbers for the basic airfoil and with serration B1-2, respectively. Both plots show generally decreasing $RMS C_p$ values with increasing Reynolds numbers, but peaks for the clean airfoil do not decrease monotonically with Reynolds number. The peak value is usually at 1.36 percent of the chord, and these values are cross-plotted versus Reynolds number in figure 25 for angles of attack of 0° , 4° , 6.5° , and 9° . A consistent oscillation with Reynolds number at the three nonzero angles is noted. It appears to be damped out at the highest Reynolds number, and could be partially due to a chordwise shift in the position of the $RMS C_p$ peak. With the serration B1-2 this oscillation does not occur, and there is a monotonic decrease in $RMS C_p$ with increasing Reynolds number.

The last three $RMS C_p$ curves, figures 26, 27, and 28, are plots for the first four pressure transducers closest to the leading edge versus angle of attack for the basic airfoil and with serration B1-2. The three curves are for Reynolds numbers 1.75×10^6 , 3.5×10^6 , and 6.2×10^6 , respectively.

These are the same type of plots as in figure 13, but there only the pressure transducer at 0.83 percent of the chord was plotted to show the effect of the various serrations. Generally, the curves for these four pressure transducers start high at 0° angle of attack then drop to a minimum between 1° and 2° , then rise monotonically with angle of attack to stall, except for the first, and sometimes the second transducer. Between 7° and 9° there is in all cases a sharp peak in the RMS C_p curve for the first transducer at 0.83-percent chord. For the clean airfoil this reaches the highest RMS C_p value. This curve for figure 27 is the same as that for the basic airfoil in figure 13, but the later results were not limited in frequency response. As is noted in section 5.6, there is considerable energy in the spectrum at very high frequencies. This accounts for the difference in the heights of these peaks in figures 13 and 27.

The effects of the serration B1-2 are now considered. For the lower two Reynolds numbers, figures 26 and 27, the peak values for the first pressure transducer is greatly reduced but the values for the second transducer are greatly increased, generally with a maximum at an angle of $7\text{-}1/2^\circ$. The peak values, though, for the first transducer are the greatest in the region of 8° . The serrated edge only has a very small effect at the highest Reynolds number, but frequency limitations of the tape recordings may severely affect these results because of the higher velocity. Changing β , the angle of the serration, has a large (factor of 2 or 3) effect on the first transducer at an angle of attack of $6\text{-}1/2^\circ$, a 15-percent effect at 9° , and at β angles outside this sensitive region, the effect was negligible. In this sensitive range of angle of attack, $6\text{-}1/2^\circ$ to 9° , no consistent effects of β variation could be noted with either serration, B1-2 or B3-2. Data for the latter serration are not presented, since they contain no significant differences from the results of the other serration. There is only a very small difference in the RMS C_p value of the second transducer between serrated edges B1-2 and B3-2 and no difference in these values at the third and fourth transducer positions. Both serrations cause these latter two transducers to indicate somewhat higher RMS C_p values than for the clean airfoil.

The RMS C_p values for the pressure transducer at $x/c = 0.0083$ chord and 85-percent span are essentially the same as for those of the transducer at the same chordwise position at 40 percent span, though values for the former tend to average about 10 percent greater. Thus, spanwise variations near the leading edge, other than possible cyclic ones due to serrated edges, appear to have been minimal over most of the airfoil span.

5.6 Frequency Analysis of Surface Pressure Fluctuations

As noted in section 4.3, two methods of analysis of the pressure fluctuations were used, both based on the tape recordings. The first employed a Spectral Dynamics Analyzer set to average the spectra of 256 ensembles. The second method, which produced correlations between signals, used the hybrid analog-digital method described earlier. While only a small amount of data was analyzed, the essentials of the pressure fluctuation process near the airfoil leading edge were determined and are presented here. All data presented in this section are from the 40-percent spanwise location.

Figure 29 is a composite of oscilloscope traces from seven pressure transducers. Both pressure versus time and corresponding energy spectra from the first of the above methods of analysis are included. Flow conditions are for the basic airfoil at an angle of attack of 9° and Re of 1.2×10^6 . Some of the samples of the traces show a large sine wave component with a wave length of roughly 1 cm, which would result in a frequency of 8 KHz. It should be noted that the vertical scale factors, C_p/cm , listed with the photos vary by as much as an order of magnitude due to the differing transducer amplifier gains. If all these sensitivities were the same as that for any of the last four traces, the top trace in figure 29(a) would have 10 times, and the next two, about 3 times larger oscillations. The RMS C_p values were measured independently using a much larger time segment than in the traces, as is also the case for the spectra. (Also, it should be noted that these seven time traces were taken independently of each other, so they cannot be examined visually for correlations between them.) The spectra in figure 29(b) are presented as log (energy) versus log (frequency). The vertical calibration is approximately 10 dB/cm and the energy levels are based on the same amplifier gain as the pressure signals. The first

four spectra show a high frequency peak. For the first three spectra this peak is at 7.0 KHz, and so is due to the sine wave noted in the pressure signal traces. There is still an appreciable bump in the spectrum at about this frequency at the 5-percent chord position. Two additional, higher frequency peaks are observed in the first spectrum at 46 and 95 percent greater frequencies than that of the fundamental peak.

The simultaneous traces for the first and second transducers ($x/c = 0.0083$ and 0.0136 , respectively) are shown in figure 30(a) for the basic airfoil at the same 9.4° angle of attack, but at twice the Reynolds number. The top trace shows exceptionally well a sine wave component in the signal at 3 cycles/cm, which is a frequency of 24 KHz. Spectra are shown for the first transducer in the top photo and for the next two transducers in the lower photo of figure 30(b). The abscissa extends to twice as great a value, 40 KHz, for these spectra as compared to those in figure 29(b). However, while the original tape recording included full response to 40 KHz, the electronics in the playback system started to roll off at 20 KHz, so the last 1-1/4 cm (grid is 10 cm long) of spectrum becomes more attenuated. All three spectra show a sharp peak at 17.5 KHz, and the first transducer has three peaks at higher frequencies of 20, 23-1/2, and 26-1/2 KHz besides several peaks at lower frequencies.

Spectra for the same set of transducers in figure 29 are shown in figure 31 for angles of attack of 4° and $6\text{-}1/2^\circ$ for the basic airfoil at $Re = 1.2 \times 10^6$. With figure 29, which is for the same conditions but at 9° , the combined effects of angle of attack and chordwise position upon the shape of the power spectra are presented. Only at the lowest angle of attack are there no high frequency peaks in the spectra from the first transducer. There is a single peak in the spectra of the following transducers which decreases in intensity until it appears as only a broad hump.

Spectra for the second and third transducers ($x/c = 0.0136$ and 0.0189 , respectively) as obtained from the analog-digital analysis technique are presented in figure 32 on log-log scales. The angle of attack for both figures is 9° . Results are shown for the basic airfoil at various Reynolds numbers, and for the B1-2 serrated edge at one Reynolds number. It is impractical to present the data points associated with the curves as there are 106 points per curve. However, for the curves presented the scatter is

seldom more than 1 dB. All curves show the high frequency peak observed above, and the amplitude is a strong function of Reynolds number. The serrated edge reduced the peak by 3.5 dB.

The coherence of the cross-spectral density function (see the Appendix for definitions) of the second and third pressure transducers are shown in figure 33. There is significant coherence in the signals at a single high Strouhal number which is the same as for the peak in the spectra in figure 33 for $Re = 1.2 \times 10^6$. Data points in the peak region are included for the dashed curve, $Re = 1.2 \times 10^6$ as they showed the greatest scatter. The other curves, where drawn, are all very well defined with very little scatter of the data points.

Convection velocity, normalized by the free-stream value, and the phase angle for the above coherence curves are very sensitive to frequency, but at the peaks of the coherence curves the angles are all $2\pi \pm 0.4$ radians. Thus the wavelength which correlates best between the second and third transducers has essentially the length of the spacing between them, which is 0.508 cm (0.2 in). The average ratio of local to free-stream velocity between these two points is 1.62. This results in a ratio of narrow-band convection velocity to local velocity of 0.90 at the frequency parameter fc/V_0 of about 250, where the coherence functions are greatest. For the basic airfoil the Strouhal number fc/\dot{V}_0 of the peaks in the spectra in figure 32 increases with increasing Reynolds number. These values are listed in Table I. Starting at $Re = 2.7 \times 10^6$ the peak is at a greater frequency than 20 KHz and off scale in the hybrid analyses.

5.7 Summary of Wind-Tunnel Results

The visualization of the airfoil leading-edge surface flow in figures 18 and 19 shows that for the basic airfoil there exists a two-dimensional bubble. The serrations divided this bubble into segments, and they changed its axial position by a small amount. In both cases the bubble moves far forward with increasing angle of attack.

Twelve serrated edges were tested. They did not produce, as in the earlier tests of reference 2, any appreciable change in the maximum lift coefficient. They did not add any measurable drag and tended to make the stall less violent. A bump in the surface static pressure distribution

due to the bubble was greatly reduced by the serrations. The unsteady signal from the pressure transducer most sensitive to the serration, generally in the center of the bubble, and the airfoil moment strain fluctuation were monitored for the twelve serrations. The moment root-mean-square signal was reduced at higher angles of attack. A very large peak in the pressure transducer signal at a lift coefficient of 0.6 was reduced in varying amounts by the various serrations. This latter reduction was insensitive to serration position but correlated well with serration spacing, the maximum reduction corresponding to the smallest spacing of 0.508 cm (0.2 in). There was a monotonic decrease towards this value, and a smaller serration size may produce further reduction.

The basic airfoil and the airfoil with the two best serrated edges (reduced peak pressure fluctuations the most) were tested in more detail for $1.2 \times 10^6 \leq Re \leq 6.2 \times 10^6$. The very large peak in $RMS C_p$ under the laminar bubble or near its trailing edge extends on downstream. At about three bubble lengths the peak RMS value is reduced 90 percent toward the slowly changing value over the rest of the airfoil. Large effects on $RMS C_p$ were observed with only small changes in Reynolds number. For the best case, at $Re = 1.75 \times 10^6$, the peak $RMS C_p$ was reduced from 0.41 to 0.24 with the serrated edge B1-2.

From the signal of the first few transducers an intense, high frequency peak in the power spectra was observed, which weakens with increasing x/c . The frequency of this peak is a function of Reynolds number, and a sine wave component at this frequency is easily recognizable in fast oscilloscope traces of the signal. The first transducer also contained other discrete energy components. Between the second and third transducers there was excellent correlation in the signals at or near this frequency. The serration B1-2 considerably reduced this energy peak.

6. THEORY AND EXPERIMENT FOR LOW REYNOLDS NUMBER FLOWS

6.1 With No Leading-edge Serrations

Since the origin of this investigation is the owl's silent flight, it is well to consider the owl wing at the onset. The basic facts are

(1) The owl, which feeds on small rodents, etc., must be unseen and unheard by its prey during its approach. Its remarkable night vision

apparently assures the "unseen" requirement. The downy feathers and the leading-edge rake (or rakes) apparently assures the "unheard" requirement.

(2) The Reynolds number of the owl is so low (of the order of 5×10^4 , more or less) that completely laminar flow would be expected for a conventional wing. The presence of the leading-edge rake is apparently to promote some turbulent flow on the wing.

For such a low Reynolds number, tests in water are ideal for flow visualization because only a very low velocity is required. An old test airfoil¹ of 30.48 cm (1 ft) chord was available from Ames Research Center. A wheeled carriage was constructed to operate on tracks mounted on a bathtub (see fig. 34) and to carry the airfoil in a vertical position. A constant-speed electric motor was used to drive a capstan which served to tow the carriage at a constant speed of 7.62 cm/sec (3 in/sec) after the initial release. This gave a test Reynolds number of 2.5×10^4 . The object in these tests was to observe and photograph the flow after introducing a red dye (Schilling's red food coloring) on the hydrofoil surface near the stagnation point just prior to release of the carriage. The camera was located so that a section view was available in the lower part of the photograph while, using an inclined mirror above the water surface a plan view was available in the upper part of the same photograph.

The boundary-layer flow on the airfoil was laminar, as expected. Figure 35 is the best photograph obtained showing the flow on the suction surface of the hydrofoil, though considerably better flow visualization was observed. This photograph is for an angle of attack of about 7° ($C_L \approx 0.6$). Both chordwise and spanwise bands of dye can be noted. Because of the inevitable nonuniformities in manually depositing the line of dye using a hypodermic tube, the chordwise dye pattern would develop, but it was determined from other flow visualization runs not to be due to any spanwise nonuniformity in the flow. In one test some dye accidentally introduced

¹This airfoil of maximum thickness somewhat less than 7 percent of the chord did not appear to be any particular NACA section. The ordinates measured and the computed velocity characteristics are given in Table III. The velocity characteristics were calculated in a similar manner to those for the 63-009 airfoil in reference 5.

near the trailing edge showed that a von Karman vortex street had formed in the wake. In figure 35, the first chordwise band is an oscillating separation bubble. The downstream bands are concentrations of dye-marked fluid created by the alternate acceleration and deceleration of the flow over the surface. The unsteadiness of these bands and the separation bubble was caused by the changing lift, or bound vorticity of the hydrofoil, as vortices were shed to form the von Karman vortex street. In some cases the downstream bands degenerated into vortices with spanwise alignment of their cores. Observations at small angle of attack (0.5°) showed no distinct bands to be present at least over the forward 50 percent of the surface. At moderate angles of attack (3° , corresponding to $C_L \approx 0.25$) up to the maximum studied (7°) the banded pattern appeared and the spacing of the bands was, as best could be observed, the same.

Roshko (ref. 11) has considered in great detail both by calculations and experiment shedding frequencies for a number of shapes including the classic case of the circular cylinder. For a circular cylinder of diameter d of 0.638 cm (0.25 in) over a range of Reynolds numbers from 880 to 4,870 he gives average values for 14 cases for Strouhal number S , vortex street velocity V_V , vortex street width d' , and velocity at separation V_S :

$$S = \frac{fd}{V_O} = 0.208 \qquad \frac{V_V}{V_O} = 0.735$$

$$\frac{d'}{d} = 1.202 \qquad \frac{V_S}{V_O} = 1.336$$

where the free-stream velocity is V_O and vortex shedding frequency, f . In figure 36(a) is diagrammed the wake vortex flow as Roshko defines it for a circular cylinder.

Of particular importance is Roshko's employment of the concept of the "universal Strouhal number of the wake" which, he argues, should be essentially independent of the shape of the bluff body which promotes the wake. If the velocity outside the wake is, on the average, the "separation" velocity V_S , then the wake Strouhal number is defined as

$$S^* = \frac{fd'}{V_S}$$

For a circular cylinder, the average value he finds is

$$S^* = 0.187$$

but it does change slightly with Reynolds number. Moreover, it is somewhat less for blunt bodies with flat forward faces.

For a blunt base hydrofoil or airfoil, the concept of the wake Strouhal number can again be of value in formulating the mathematical model (see fig. 36(b)). However, it must be recognized that flow from the blunt trailing edge of the foil must differ from a blunt cylinder in several important respects.

First, for the cylinder the effects of viscosity on the wake flow are essentially confined to the shear layer containing the vortices. That is, the flow is nearly an inviscid one except in the shear layer. Thus, the ratio of vortex street width, d' , to the cylinder diameter, d , should be fixed. For the foil, the vortices must originate within the relatively thick trailing-edge, upper-and-lower-surface boundary layers, and the thicknesses of these layers must be added to the physical thickness of the trailing edge to obtain the effective thickness of this blunt body.

Now, it is well known that for a laminar flow the boundary-layer thickness varies inversely with the square root of the Reynolds number. For example, for one side of a flat plate the displacement thickness, δ^* , in terms of the chord, c , is

$$\frac{\delta^*}{c} = \frac{1.73}{\sqrt{Re}}$$

so that for the two surfaces (upper and lower) of a wing the total displacement thickness would be twice this value.

It is expected that vortices which originate within the trailing-edge boundary layers will be formed at some multiple of δ^* from the surface. Therefore, it has been assumed that the width of the vortex street can be found as the sum of the actual trailing-edge thickness and a factor $k/1.73$ of the two (upper and lower surface) displacement thicknesses, or

$$\frac{d'}{c} = 2 \frac{y_{t.e.}}{c} + \frac{k}{\sqrt{Re}}$$

Second, it is to be expected that the velocity corresponding to the separation velocity, V_s , for the cylinder will be an effective trailing-edge velocity, $V'_{t.e.}$, something less than the velocity outside the boundary layer, $V_{t.e.}$, but bearing a fixed relation with $V_{t.e.}$.

Given the experimental Strouhal number for an airfoil

$$S = \frac{fc}{V_o}$$

it can be related to $V'_{t.e.}/V_{t.e.}$ with the expression ($V'_{t.e.}$ is interchanged with V_s):

$$\frac{V'_{t.e.}}{V_{t.e.}} = \frac{S}{S^*} \left(\frac{d'}{c} \right) \left(\frac{V_o}{V_{t.e.}} \right)$$

Rearranging the above equation and substituting for (d'/c) on the previous page,

$$S^* \left(\frac{V'_{t.e.}}{V_{t.e.}} \right) \left/ \left(\frac{V_o}{V_{t.e.}} \right) \right. = S \frac{d'}{c} = S \left(0.00917 + \frac{k}{\sqrt{Re}} \right)$$

The terms on the far left-hand side should all be constants. Assuming this, the data for the NACA 0012 wing test (see Table I)² were used to determine that the best value for k is 7.3. Finally, using this value, the value of S^* for the circular cylinder (0.187) and $V_{t.e.}/V_o$ for the NACA 0012 (0.936),

$$\frac{V'_{t.e.}}{V_{t.e.}} = 5.71 S \left(0.00917 + \frac{7.3}{\sqrt{Re}} \right)$$

The following table gives the values for the needed velocity ratio.

V_o , ft/sec	\sqrt{Re}	S_{exp}	$V'_{t.e.}/V_{t.e.}$
25	287	5.00	0.989
60	447	6.67	.972
100	580	8.00	.994

²It should be noted that the physical thickness for the trailing edge of this wing is considerably greater than it should be for a true NACA 0012 section. The actual thicknesses were provided by the Bolt, Beranek & Newman Company.

These results are very gratifying in that they indicate nearly the same value of $V'_{t.e.}/V_{t.e.}$ for all Reynolds numbers (well within the experimental scatter for S which is about 10 percent). Using the average of the values, the equation for the Strouhal number of any wing (based on chord) becomes

$$S = \frac{0.171(V_{t.e.}/V_o)}{\left(2 \frac{y_{t.e.}}{c} + \frac{7.3}{\sqrt{Re}}\right)} = \frac{fc}{V_o}$$

If now we calculate S for the NACA 0012 propeller tests of reference 4 (for which $2(y_{t.e.}/c) = 0.0275$; $V_{t.e.}/V_o = 0.936$), we get poor agreement with experiment as indicated by the following:

V_o , ft/sec	\sqrt{Re}	S_{calc}	S_{exp}
104	335	3.25	6.41
196	467	3.71	6.80

This kind of disagreement could be expected for the following reason: in the laminar boundary layer of a rotating airfoil (propeller) the laminar sublayers are nearly stopped relative to the blade. Hence they are subject to the centrifugal force which draws this low-energy flow to the propeller tip. Then, if all the laminar layers were drained away, the Strouhal number should be the limiting value

$$S = S^* \left(\frac{V_{t.e.}/V_o}{2y_{t.e.}/c} \right) = \frac{0.187(0.936)}{0.0275} = 6.36$$

which, within the limits of accuracy of the tests, is what was measured.

6.2 With Leading-Edge Serrations

The hydrofoil and the NACA 0012 wing and propeller tests agree in several important aspects.

1. At very low angles no fluctuations at a single frequency were observed.
2. At modest angles of attack (say 4° to 8°) the single frequency of the vortex shedding usually appeared for the basic foil.
3. With properly placed and shaped leading-edge serrations the single frequency of the vortex shedding usually disappeared.

With the hydrofoil the following leading-edge rakes were tried:

	<u>Spacing</u>		<u>Tip Height</u>	
	cm	in	cm	in
(1) A twisted V-tooth rake	0.508	0.20	0.508	0.20
(2) A wire tine rake	0.127	0.050	0.25	0.1
(3) Two artificial eyelashes (typical)	0.013	0.005	0.8	0.3

These are shown approximately full size in figure 37. The upper surface spanwise pattern was not completely eliminated by the streamwise vortices generated by the V-tooth rake as seen in figure 38. The pattern was improved with the wire tine rake but was not perfect (fig. 39). The pattern seemed to be eliminated by the eyelashes with which the flow appeared to be turbulent (fig. 40).

It is of interest to note that the eyelashes, which appeared most effectively to destroy the spanwise vortices, are most nearly the type of leading-edge rake with which the owls are equipped.

It is believed that the most effective length of leading-edge serration should be related to the length of the owl's serrations through some function of the Reynolds number, the parameter which controls the boundary-layer behavior.

6.3 Summary of Low Reynolds Number Flow Results

A low Reynolds number flow visualization experiment was performed using a 6.7-percent thick hydrofoil towed through calm water. A von Karman vortex street was found trailing from the rear of the airfoil, and this was directly related to the laminar bubble oscillations, which were of the same frequency. A theory, which is in agreement with experiment, is proposed for predicting the frequency of this oscillation for the low Reynolds number flow case. It relates the vortex shedding frequency to the airfoil trailing edge thickness and upper and lower surface boundary-layer thicknesses.

Three serrations were tested. The one with closest spacing, artificial eyelashes, performed best in eliminating the bubble by producing turbulence on the upper surface of the airfoil.

7. THEORY FOR HIGH REYNOLDS NUMBER FLOW

7.1 Strouhal Number Comparison

At high Reynolds number the discharge of a uniform vortex street at the wing trailing edge is not possible since the boundary layer is turbulent on most of the aft portions of the wing surface. Notwithstanding, present wind-tunnel tests showed that a dominant, very high frequency pressure fluctuation was evident to high lift coefficients at the airfoil surface in the vicinity of the laminar boundary-layer separation.

For the low Reynolds number flows it was shown that the Strouhal number based on chord is

$$S = \frac{0.171 (V_{t.e.}/V_o)}{2 \left(\frac{y_{t.e.}}{c} + \frac{7.3}{\sqrt{Re}} \right)}$$

This equation gives for the present NACA 63-009 airfoil tests at the lowest Reynolds number, 1.22×10^6 , the value

$$S_{calc} = 21.7$$

and at the highest Reynolds number, 7.6×10^6 , the value

$$S_{calc} = 48.8$$

As noted in section 5.6, the Strouhal number increased with Reynolds number, and it had a minimum value of (see Table I)

$$S \geq 300$$

There is clearly no evident connection between the observed behavior of the high and low Reynolds number cases. This is expected to be due to the basic differences in the flow at the trailing edge of the airfoil. In the discussion to follow, two hypotheses are examined in an attempt to explain the observed facts for the high Reynolds number case.

7.2 First Hypothesis

If one assumes that the separation bubble is essentially fixed in position relative to the airfoil surface but that vortices are shed within the unstable laminar region, one might explain the single frequency fluctuations which the present experiments show occur under the bubble at the position indicated by the flow visualization of the present experiment and by Gault's (ref. 6) detailed boundary-layer measurements through the bubble. These pertinent profiles are reproduced here in figure 41 together with the shape of the reverse flow. With a fixed position for the bubble and for the turbulent boundary layer downstream, if a vortex street were shed in the laminar boundary layer it would almost immediately lose its identity in the turbulent boundary layer. That is, the turbulent eddies would destroy such a uniform street in a short distance. The wind-tunnel test shows somewhat to the contrary that the dominant single frequency fluctuation can still be identified at the airfoil surface in the pressure-time traces of figure 29 at $x/c = 0.05$, while the bubble ends at $x/c = 0.01$. The difference in these distances represents about 100 boundary-layer thicknesses. The assumption that the separation bubble is essentially fixed in position is consistent with the experimental results. Note, however, that the concept of a moving position for the separation bubble is not necessarily inconsistent with the Gault boundary-layer measurements since his measurements were made with very slow response manometers. Accordingly, a second hypothesis is the favored explanation of the observed facts.

7.3 Second Hypothesis

Separation of a laminar boundary layer occurs when, in the adverse pressure gradient, the velocity gradient normal to the wall falls to zero. The separation streamline is modeled here as starting tangent to the surface at x_s/c . The concave surface moves away from the tangent so that the boundary layer near the surface must have a negative velocity gradient. Velocity profiles of the type shown in figure 41 result. Such a separated profile is known to be unstable to disturbances so that transition to turbulent flow is initiated at some station, x_t/c . The turbulent eddies introduce high-energy air from the outer reaches of the boundary layer into the region near the wall so that some distance downstream, at x_a/c , the reattachment occurs.

An important factor to be noted here is that a boundary-layer thickness, which very gradually increases with increasing x/c , has only a minor influence on the velocity distribution outside the boundary layer so that a theoretical velocity distribution assuming an inviscid flow is in excellent agreement with experiment in these cases. When a separation bubble occurs this is not the case if the ratio of height of the bubble to its length becomes important. Under these circumstances, the theoretical velocity must be slowed ahead and behind the bubble and must be speeded up on top of the bubble. The pressure distributions of figures 15 and 16 show this distortion when a separation bubble is present. This distortion is, of course, dependent on the shape of the bubble. The displacement thickness at a lift coefficient of 0.72 was calculated by

$$\delta^* = \int_0^{\delta} \left(1 - \frac{V_U'}{V_U} \right) dy'$$

where V_U' and V_U are the velocities inside and outside the boundary layer, respectively, y' is any point above the surface within the layer, and δ is the total height of the boundary layer. To obtain the necessary accuracy, the velocity profiles were replotted. See reference 5.

The resulting δ^* distribution is shown in figure 42 along with a cosine bump for comparison.

When a bump of a flat surface has a cosine shape, as shown in figure 43, the distortion to the velocity on the surface is that shown in the figure. The derivation of this velocity function is given in reference 12. We may find the height and wavelength of the bump by reference to the diagram of figure 44. Over the interval of x/c from the separation point, x_s/c , to the reattachment point, x_a/c , we assume that the transition point, x_t/c , is where the bump height, h , is a maximum. The wavelength is

$$\frac{\lambda}{c} = 2 \left(\frac{x_t}{c} - \frac{x_s}{c} \right)$$

and the height-to-length ratio is

$$\frac{h}{\lambda} = \frac{1}{2} (\beta_s - \beta_t)$$

where β is the angle between the surface tangent and the x -axis. The values of β as a function of x/c for the NACA 63-009 airfoil section were measured and are included in Table II.

We are now ready to proceed with the fundamental argument of this second hypothesis which is that:

(a) The bubble velocity profiles such as measured by Gault (using very slow response manometers) is not necessarily fixed in the indicated position given by such measurements, but

(b) Such profiles may only be the time average of an unstable oscillating system wherein the bubble at any instance may be moving fore and aft and changing in both wavelength and height.

(c) Something must be capable of forcing an initial bubble motion, and

(d) There must be two degrees of freedom which have a phase lag between them. These are the potential flow, which adjusts very rapidly, and the viscous flow, which develops much more slowly.

Now, let us consider the flow over a NACA 63-009 airfoil at $C_L = 0.72$. The theoretical upper-surface velocity ratio, V_U/V_O , is given by

$$\frac{V_U}{V_O} = \frac{V_f}{V_O} + C_L \left(\frac{V_a}{V_O} \right)$$

and is shown as the solid line in figure 45.

If the flow over this airfoil were abruptly started, this velocity distribution would be obtained, and the flow would for the moment be all laminar. However, the laminar boundary layer cannot remain attached far from the leading edge. In fact, separation will occur where

$$\frac{V_S}{V_{U_{\max}}} \approx 0.9$$

From figure 45, this occurs when

$$\frac{x}{c} = \frac{x_S}{c} = 0.0046$$

As noted earlier this layer is unstable so at some point, x_t/c , transition to turbulent will start. If we assume that

$$\frac{x_t}{c} = 0.0090$$

a separation bubble³ having

$$\frac{h}{\lambda} = 0.073$$

will grow. The calculated details are given in Table IV and the resulting pressure distribution is shown in figure 45 as the first bubble position. The presence of the bubble now so alters the velocity distribution ahead of it that the separation must move forward to

$$\frac{x_s}{c} = 0.00342$$

Let us assume that the transition chases forward to

$$\frac{x_t}{c} = 0.00550$$

and repeat the calculation for the new bubble (see Table V). The velocity distribution for this second case is shown in the same figure as the second bubble position.

Again, however, the separation point must move ahead to

$$\frac{x_s}{c} = 0.00300$$

Let us assume that in this case the transition has moved to

$$\frac{x_t}{c} = 0.00380$$

³At this point, for simplicity, we will denote the δ^* distribution as the shape of the bubble even though a slight difference exists.

and repeat the calculation. Then the values in Table VI are obtained, which give the velocity distribution in the same figure as the third position. Again the bubble must move to

$$\frac{x_s}{c} = 0.00298$$

Here we assume

$$\frac{x_t}{c} = 0.00370$$

The resulting velocity distribution (Table VII) is shown in the same figure as the fourth position.

It is here that we come to the end of this computational process, for now the minimum in the velocity distribution is greater than $0.9V_{U_{max}}$ so the separation point would move to a point downstream of the separation bubble which, of course, is absurd. What would actually occur is that the laminar shear on this last bubble would become so large as to sweep this bubble down into the wake. Thus the whole process would start as before and be repeated again and again.

To effect this kind of instability it is only necessary to assume, as shown in figure 46, that the transition point essentially catches up to the separation point so that the velocity gradient ahead of the bubble cannot support the bubble position.

This analysis does not constitute a complete theory, but it shows the main features of a bubble oscillation mechanism. The correct and complete solution would have to be one which would agree with Gault's measured boundary layer as the time-averaged one, and the dynamics of the bubble movement must be included and result in the measured surface pressure oscillations.

It is instructive to compare the bubble position and magnitude of the velocity oscillation in figure 45 with the flow visualization results and the pressure traces from the present experiment. At $c_\ell = 0.7$ in figure 20 the separation and attachment positions are approximately $(x/c)_s = 0.004$ and $(x/c)_a = 0.010$. These values are a reasonable time average for the chordwise variation in position indicated in figure 45. At $x/c = 0.008$

in the same figure, instantaneous values of V_U/V_O would range between 2.7 and 2.0. This corresponds to a C_p difference of 3.4. For the first pressure transducer, which is at $x/c = 0.0083$, the amplitude of the oscillation in figures 29 and 30 is typically one-third this value.

Finally, the wind-tunnel experimental results show a large peak in fluctuation intensity at a moderate lift coefficient. An explanation for this behavior is suggested. At lower lift coefficients it is expected that the laminar layer is very thick when separation would begin and transition to turbulence occurs before separation, or so short a distance after separation that no important distortion to the inviscid velocity distribution can exist. At the higher lift coefficients, the theoretical pressure distribution for the inviscid flow becomes dominated by the "additional distribution" (corresponding to V_a/V_O in Table II) and perhaps these gradients are so steep that the type of instability discussed earlier cannot occur.

7.4 Summary of High Reynolds Number Flow Theory

When the relationship developed in section 6.1 for predicting the Strouhal number of bubble oscillation for low Reynolds number cases is applied to the present high Reynolds number wind-tunnel results, the predictions are an order of magnitude too low. It is concluded that there are at least two flow regimes and that their extent is a function of Reynolds number. A first hypothesis for the flow behavior is briefly examined which involves the possible existence of a vortex street in the shear layer above a stationary bubble, but it does not appear to conform to the experimental observations.

A second hypothesis models the flow near the wall as containing a bubble which is oscillating in size and position. By comparison with the time-averaged profiles through the bubble from Gault (ref. 6), it is determined that the shape of the bump (the displacement thickness distribution) is closely modeled by a cosine function. With the resulting pressure distribution superimposed on the theoretical pressure distribution of the upper surface of the airfoil, it is found that the separation and reattachment points, and thus the bubble, will move forward (the position of transition in the bubble must be assumed) until there is no separation. The bubble is thus convected away and a new one is then formed. The

analysis includes a mechanism to explain the bubble oscillations in size and position.

8. LEADING-EDGE REGION FLOW GEOMETRY CAUSED BY SERRATIONS

8.1 Introduction

The rake on the leading edge of an owl's wing has a fine spacing of about 20 serration points per inch. The authors believe that its serrations create turbulence which prevents trailing-edge vortex shedding. However, at high Reynolds number the flow visualization of figures 18 and 19 shows a regular, highly structured pattern that is not expected to be due to turbulence. Similarly, using titanium dioxide, Soderman (ref. 3) produced the spectacular surface flow visualization result shown in figure 47. In this photograph, which is looking directly at the leading edge of his airfoil, the serration is seen screwed to the wing with the tips pointing to the left, the suction side. In subsonic flows two-dimensional separations can be unsteady, and one mechanism for unsteadiness was presented in section 7.3. Three-dimensional separations that are steady have been reported in the literature. These invariably involve a three-dimensional vortex like that on a leading edge of a delta wing or a trailing vortex. The serrated edge tips shed shear layers that roll up into vortices. A flow for the leading-edge region is proposed herein that may create a steady three-dimensional separation.

Before proceeding, the photographs of figures 19 and 47 are examined for the information they contain. In both cases, the laminar bubble is divided into segments the width (distance in spanwise direction) of which is the same as the spacing of the serrated-edge tips. In figure 19, the oil is swept clean in a line directly downstream of the serration tip, generally past most of the bubble, then the fluid leaking from the corners of adjacent bubbles joins and continues along the same line. In figure 47 the bubble segments are more clearly divided, do not have the sharp corners of those in the previous photograph, and the perimeters are very sharply outlined in a heart-like shape. Moreover, in this photograph the clean area between bubbles continues on past the separation bubbles and far downstream.

8.2 Construction of the Local Flow Geometry

Figures 48 and 49 show various schematic views of the proposed interpretation of the flow in the leading-edge region. For these views, the leading edge of the airfoil surface has been unwrapped from the airfoil and flattened to simplify visualization. Figure 48 is a perspective view looking forward toward the serrated edge. Using this view the essential features of the flow are first outlined, and then, using the views of figure 49 the details of the flow are developed.

In figure 48, symmetric vortex pairs originate from each serration tip since the tips are being pushed toward the airfoil surface. Trailing downstream, they lie very close together and are of a rotational sense that induces mutual upward movement from the surface. However, these pairs start separating and thus each vortex moves toward the adjacent vortex from the next serration tip. These new vortex pairs induce movement in each other downward, and this new pair comes close enough to the surface to dominate completely the flow there over a short length. This region is the separation bubble. As the new vortex pairs approach the wall, their images drive them apart. As they separate, the back end of the bubble forms and inviscid fluid that has flowed over the separation bubble is induced down to the surface to start a new boundary layer, most of the severe adverse pressure gradient along the wall now lying upstream of this chordwise position.

Figure 49(a), a top view, shows the tip of a serrated edge with vortices (dotted) trailing downstream and those streamlines which are immediately adjacent to the surface, which are denoted as limiting streamlines. The principles given by Maskell (ref. 13) for constructing limiting streamlines are used here along with his terminology. It is to be noted that in figure 49(a) the B1-2 serration tip, the resulting bubble, and the distance between are to scale for the present NACA 63-009 flow visualization tests. The distance to the bubble from the serration tips in figure 49 appears to be about the same in figure 47. Figure 49(b) is a side view of a serration tip, trailing vortex (dotted) and separation bubble, while the crossflow movement of the vortices and their images is indicated in the end view in figure 49(c). The numbers on the vortices correspond to the numbers on the cross sections in figure 49(a).

We now examine the flow in more detail. The correct positioning of the trailing vortices leaving the serration tip is unknown. It is expected, however, to be unimportant, as the original vortex pair (fig. 48, 49(a)) will rise from the surface immediately if close together compared to their distance from their images. If they lie closer to the surface than indicated in position 1 of figure 49(c), so that they are each very close to their images, they are induced by their images to approach each other, then rise. A plausible argument is necessary to show that while rising, the vortex pairs also separate. The external flow is two-dimensional and cannot be the cause. The infinite rows of vortices and their images are not expected to cause this splitting, though this has not been checked in great detail. However, there are two mechanisms available to accomplish this. The vortex pairs cause the boundary layer to become three-dimensional and when this occurs there is boundary-layer vorticity (note the dotted arrow in fig. 49(a)) with a vector component in the axial direction. It is of the correct rotational sense to cause the vortex pairs to split. Also, the external potential flow causes these trailing vortices to curve around the leading edge from lower to upper side, approximately following the surface. They then can induce crossflow velocities upon themselves. Consider the symmetric vortex pair from a serration tip to remain at constant spacing, but bent into a circular arc as an approximation of the flow around the nose of the airfoil. At any cross section that part of each vortex line which is upstream is inducing its own vortex to approach the other one; and that part which is downstream does the opposite. It is believed that the initial upward induction of the vortices and acceleration and turning of the flow around the airfoil nose will cause the divergence of the vortex pair.

When the original vortex pairs diverge enough to form new vortex pairs (fig. 48 and 49(c), position 3), the recirculating flow associated with each vortex pair will be approximately as shown schematically in figure 49(d). The boundary-layer flow at the surface, which has suffered a strong adverse pressure gradient and is nearly ready to separate as it approaches the bubble, will be strongly influenced by the pressure fields of the vortex pair and the bubble and will tend to diverge from the vortex pair centerline. When the recirculating flow in figure 49(d) attaches to the surface, the outer streamlines which radiate out from the centerline, actually a

stream sheet, will come tangent to the separation lines, which are labeled "S" in figure 49(a), on the inside of the bubble, while the limiting streamlines on the upstream surface will come tangent to this separation line on the other side. The resulting stream sheet will flow up over the bubble, swirl inward toward the vortex core (fig. 48(e) and follow the vortex core on downstream. This is the key to the mechanism of a steady separated flow. Low energy fluid is removed from near the wall and conducted out of the critical region and on downstream around the vortex in a steady manner.

Above the separation stream sheet, made up of the separation streamlines, is the stream sheet labeled "Attachment Stream Sheet" in figure 49(b); it is the top of the bubble. The fluid in it flows down the center plane, attaches to the wall at the attachment line (labeled "A") and then flows underneath the vortex as the limiting streamlines in the separation bubble to the separation line. (These limiting streamlines are the same ones inside the bubble described in the previous paragraph.) This completes the circuit around the separation bubble as viewed in cross section. The flow into the gap between the separation stream sheet and the attachment stream sheet is composed of the low-energy boundary-layer fluid that spirals on downstream around the vortex core.

At the rear of the bubble the attachment line splits and becomes the attachment lines (labeled "A") for the new wall flow downstream of the bubble. This completes the flow structure. It is noted that the beginning and end of the attachment line on the new centerline are singular points; the flow direction there is undefined.

In figure 49(a) the separation streamline is brought tangent to the separation tip centerline and the original vortex pairing has reoccurred. This agrees with the flow visualization of figure 19. However, for Soderman's flow picture, figure 47, this may not happen. The vortices may not rejoin since the wall flow piercing between the separation bubbles apparently continues on downstream. The separation line in figure 49(a) need not reach the centerline. If the strong white perimeter line in figure 47 are separation and attachment lines all the way around the separation bubble, then it appears that for this flow the vortices must rise off the wall. This would require that the rear attachment lines connect to the separation lines at two more singular points. To understand this added complication more flow definition is required.

8.3 Summary of the Leading-Edge Region Flow Description

A flow model is constructed to explain the segmented bubbles that are evident in the surface flow visualization results of the leading-edge region in the present experiment and in that of Soderman (ref. 3). It is hypothesized that trailing vortex pairs from each serration tip gradually rise while being convected downstream, then separate and form new vortex pairs, each with its adjacent vortex from the next serration tip. These new vortex pairs are of opposite sense from the original pair and they sink very close to the surface to form the three-dimensional separation bubble pattern.

9. CONCLUDING REMARKS

Pressure and force measurements, steady and unsteady, have been made on a rectangular wing with an NACA 63-009 airfoil section over the Reynolds number range 1.2×10^6 to 6.2×10^6 . Flow visualization has been performed on this airfoil and on a 6.7-percent thick hydrofoil at a Reynolds number of 2.5×10^4 . A two-dimensional bubble fluctuating in size and position near the leading edge was observed on the hydrofoil, and its presence is deduced from the surface flow visualization and unsteady pressure measurements on the airfoil over a wide range of angle of attack. Low and high Reynolds number flow regimes are discerned, being characterized by the presence, or lack of, a trailing vortex street, respectively.

For the low Reynolds number experiment, the boundary layers at the trailing edge were laminar, and a von Karman vortex street was observed in the wake flow. It was noted that the bubble oscillated at the same frequency; thus the latter appeared to control the bubble. A theory for predicting the Strouhal number of this phenomenon, which is in good agreement with the experimental results in reference 4, is presented. It relates the shedding frequency to the airfoil trailing-edge thickness and upper and lower surface boundary-layer thicknesses.

In the high Reynolds number experiment, large, unsteady pressures were observed in the region of the bubble and for several bubble lengths downstream. Spectral analysis of these pressures show that there usually were large, high frequency peaks in the signal from the most forward pressure transducer, which was almost always under the bubble, and a

single high frequency peak in the spectra from the second transducer. The intensity of this peak decayed with increasing distance. The Strouhal number of this energy peak varies with Reynolds number, but is not given by the low Reynolds number theory. It is assumed that for this flow regime the turbulent boundary layers at the trailing edge prevent the shedding of vortices, and it is hypothesized that the bubble oscillation is controlled by an unstable laminar boundary-layer separation. By comparison with time-averaged velocity profiles through the bubble obtained by Gault (ref. 6) on the same section profile, it is determined that the shape of the bump (the displacement thickness distribution) is closely modeled by a cosine function. With the resulting pressure distribution superimposed on the theoretical pressure distribution of the upper surface of the airfoil, it is found that the separation and reattachment points, and thus the bubble, will move forward (the position of transition in the bubble must be assumed) until there is no separation. The bubble is thus convected away and a new one is then formed. The analysis includes a mechanism to explain the bubble oscillations in size and position.

Three serrations were tested in the low Reynolds number experiment. The one with closest spacing, artificial eyelashes, performed best in eliminating the bubble by producing turbulence on the upper surface of the airfoil.

Twelve serrations were tested in the high Reynolds number experiment. The large peak in the root-mean-square signal from the most forward pressure transducer at a lift coefficient of 0.6 was reduced by 41 percent by the best serration. This reduction was insensitive to serration position, but correlated well with serration spacing, the maximum reduction corresponding to the smallest spacing of 0.508 cm (0.2 in). There was a monotonic decrease towards this value, and a smaller serration size may produce further reduction. A flow model is constructed to explain the segmented bubbles that are evident in the surface flow visualization results of the leading-edge region in the present experiment and in that of Soderman (ref. 3). It is hypothesized that trailing vortex pairs from each serration tip interact with the boundary layer flow to form these bubbles.

Nielsen Engineering & Research, Inc.
Mountain View, California
March 31, 1972

APPENDIX

DEFINITIONS OF STATISTICAL FUNCTIONS

The definitions and methods for acquisition of the statistical functions used to describe the properties of random pressure fluctuations are summarized below:

The power- and cross-spectral densities in the frequency range from 10 Hz to 20 kHz were obtained by a hybrid analog-digital computing process (ref. 9) for a total of 106 frequency points per spectrum measurement. They are defined as follows:

(a) Power-spectral-density function

$$G_x(f) = \lim_{\substack{\Delta f \rightarrow 0 \\ \bar{T} \rightarrow \infty}} \frac{1}{(\Delta f) \bar{T}} \int_0^{\bar{T}} p_x^2(t; f, \Delta f) dt$$

where $p_x(t)$ denotes time history record of pressure fluctuations measured at location \underline{x} ; and $p(t; f, \Delta f)$ is that portion of $p(t)$ in a frequency range from $f - \Delta f/2$ to $f + \Delta f/2$.

(b) Cross-spectral-density function

$$G(\underline{\xi}, f) = C(\underline{\xi}, f) - jQ(\underline{\xi}, f)$$

where $\underline{\xi}$ is the position vector between the points of the correlation. The cospectral density C and quadspectral density Q are defined as

$$C(\underline{\xi}, f) = \lim_{\substack{\Delta f \rightarrow 0 \\ \bar{T} \rightarrow \infty}} \frac{1}{\Delta f \bar{T}} \int_0^{\bar{T}} p_x(t; f, \Delta f) p_{x+\underline{\xi}}(t; f, \Delta f) dt$$

and

$$Q(\underline{\xi}, f) = \lim_{\substack{\Delta f \rightarrow 0 \\ \bar{T} \rightarrow \infty}} \frac{1}{\Delta f \bar{T}} \int_0^{\bar{T}} p_x(t; f, \Delta f) p_{x+\underline{\xi}}^0(t; f, \Delta f) dt$$

where $p_{x+\underline{\xi}}^0(t; f, \Delta f)$ denotes a 90° phase shift from $p_{x+\underline{\xi}}(t; f, \Delta f)$.

The component of the power spectrum of one pressure signal that is correlated to a second signal can be depicted by the coherence function .

$$\gamma(\underline{\xi}, f) = \frac{|G(\underline{\xi}, f)|^2}{|G_x(f)| |G_{x+\underline{\xi}}(f)|}$$

and the phase angle is given by

$$\theta(\underline{\xi}, f) = \tan^{-1} [Q(\underline{\xi}, f) / C(\underline{\xi}, f)]$$

The narrow band convection velocity is defined as

$$U_c = 2\pi f \underline{\xi} / \theta(\underline{\xi}, f)$$

REFERENCES

1. Hertel, Heinrich: Structure, Form and Movement. Reinhold Publishers, 1966.
2. Soderman, Paul T.: Leading-Edge Serrations which Reduce the Noise of Low-Speed Rotors. NASA TN D-7371, Aug. 1973.
3. Soderman, Paul T.: Aerodynamic Effects of Leading-Edge Serrations on a Two-Dimensional Airfoil. NASA TM X-2643, Sept. 1972.
4. Hersh, Alan S. and Hayden, Richard E.: Aerodynamic Sound Radiation From Lifting Surfaces with and without Leading-Edge Serrations. NASA-CR- 114370, 1971.
5. Allen, H. Julian: Progress Report on the Owl Wing as a Noise Suppressor. Nielsen Engineering & Research, Inc., NEAR TR 40, Jan. 1972.
6. Gault, Donald E.: Boundary Layer and Stalling Characteristics of the NACA 63-009 Airfoil Section. NACA TN 1894, 1949.
7. McCullough, George B. and Gault, Donald E.: Examples of Three Representative Types of Airfoil Section Stall at Low Speed. NACA TN 2502, Sept. 1951.
8. Abbott, Ira H. and von Doenhoff, Albert E.: Theory of Wing Sections. Dover Press, 1958.
9. Lim, Raymond S. and Cameron, William D.: Power and Cross-Power Spectrum Analysis by Hybrid Computers. NASA TM X-1324, Dec. 1966.
10. Lamar, J. E.: A Modified Multhopp Approach for Predicting Lifting Pressures and Camber Shape for Composite Planforms in Subsonic Flow. NASA TN D-4427. July 1968.
11. Roshko, Anatole: On the Drag and Shedding Frequency of Two-Dimensional Bluff Bodies. NACA TN 3169, 1954.
12. Allen, H. Julian: Notes on the Effect of Surface Distortions on the Drag and Critical Mach Number of Airfoils. NACA ACR-3129, Sept. 1943.
13. Maskell, E. C.: Flow Separation in Three Dimensions. Royal Aircraft Establishment Farnborough Rep. No. Aero. 2565, 1955.

TABLE I
DATA FOR VARIOUS WING MODELS

$\nu = 1.5 \times 10^{-5} \text{ m}^2/\text{sec}$ ($1.6 \times 10^{-4} \text{ ft}^2/\text{sec}$) unless otherwise stated.

Owl: Darwinian

$$c = 0.013 \text{ m (0.42 ft)}; 2y_{t.e.}/c = 0.0012$$

$$V_o = 6.1 \text{ m/sec (20 ft/sec) (assumed flight speed)}$$

$$Re = 5.2 \times 10^4$$

Serration: Tip spacing: 16/cm (41/in); Height: 0.28 cm (0.11 in)

NACA 0012 Wing Test: Hersh and Hayden (ref. 4)

$$c = 0.152 \text{ m (0.5 ft)}; 2y_{t.e.}/c = 0.00917$$

V_o		Re	$S \pm \Delta S^*$
<u>m/sec</u>	<u>ft/sec</u>		
7.62	25	8.33×10^4	5.00 ± 0.50
18.3	60	2.00×10^5	6.67 ± 0.67
30.5	100	3.33×10^5	8.00 ± 0.80

NACA 0012 Propeller Test: Hersh and Hayden (ref. 4)

$$c = 0.0508 \text{ m (0.167 ft)}; 2y_{t.e.}/c = 0.02750$$

V_o		Re	$S \pm \Delta S$	<u>RPM</u>
<u>m/sec</u>	<u>ft/sec</u>			
31.7	104	1.16×10^5	6.41 ± 0.64	2000
59.8	196	2.18×10^5	6.80 ± 0.68	4000

Hydrofoil Test: Present Study

$$c = 0.3048 \text{ m (1 ft)}; 2y_{t.e.}/c = 0.00324$$

$$V_o = 0.0762 \text{ m/sec (0.25 ft/sec)}$$

$$\nu = 0.093 \times 10^{-5} \text{ m}^2/\text{sec} (0.10 \times 10^{-4} \text{ ft}^2/\text{sec})$$

$$Re = 2.5 \times 10^4$$

*S is the center frequency of the 1/3 octave band frequency analyzer, and ΔS is the possible approximate spread within that band.

TABLE I (CONC.)

NACA 63-009 Wing Test: Present Study

$c = 0.9144 \text{ m (3 ft)}$; $2y_{t.e.}/c = 0.000555$

$\underline{m/sec}$	$\underline{ft/sec}$	\underline{Re}	\underline{S}
20.4	67.5	1.2×10^6	302
28.6	94	1.75×10^6	342
40.5	133	2.45×10^6	406
57.4	188	3.50×10^6	
81.2	266	4.9×10^6	
103.4	339	7.60×10^6	

TABLE II
NACA 63-009 PROFILE CHARACTERISTICS
 $r_{l.e.}/c = 0.00631$

x/c	y/c	V_f/V_o	V_a/V_o	β (rad.)
0	0	0	3.058	1.571
0.001	0.00365	0.578	2.787	1.050
.002	.00490	.732	2.496	.87
.003	.00591	.844	2.242	.75
.004	.00674	.902	2.033	.67
.005	.00749	.941	1.889	.61
.006	.00812	.972	1.778	.57
.007	.00872	.992	1.686	.54
.0075	.00906	1.001	1.647	.525
.009	.00986	1.012	1.543	.485
.010	.01037	1.016	1.480	.465
.0125	.01151	1.025	1.339	
.025	.01582	1.063	.961	
.050	.02196	1.086	.689	
.075	.02655	1.098	.560	
.100	.03024	1.105	.484	
.150	.03591	1.114	.386	
.200	.03997	1.120	.324	
.250	.04275	1.124	.281	
.300	.04442	1.126	.248	
.350	.04500	1.125	.220	
.400	.04447	1.120	.196	
.450	.04296	1.111	.175	
.500	.04056	1.099	.156	
.550	.03739	1.084	.140	
.600	.03358	1.068	.124	
.650	.02928	1.051	.109	
.700	.02458	1.032	.095	
.750	.01966	1.012	.082	
.800	.01471	.994	.069	
.850	.00990	.971	.057	
.900	.00550	.950	.044	
.950	.00196	.932	.030	
1.000	.00056	.915	0	

TABLE III
HYDROFOIL PROFILE CHARACTERISTICS
 $r_{l.e.}/c = 0.00667$

x/c	y/c	v_f/v_o	v_a/v_o
0	0	0	2.952
0.001	-	-	-
.002	-	-	-
.003	-	-	-
.005	-	0.898	1.795
.0075	-	0.969	1.592
.0125	0.01041	1.041	1.357
.025	.01250	1.105	0.988
.050	.01625	1.137	.724
.075	.01908	1.144	.583
.100	.02087	1.144	.500
.150	.02446	1.138	.430
.200	.02804	1.128	.359
.250	.02988	1.119	.309
.300	.03208	1.107	.269
.400	.03333	1.084	.212
.500	.03296	1.061	.169
.600	.02979	1.038	.135
.700	.02500	1.014	.106
.800	.01846	0.990	.078
.900	.01083	0.965	.051
.950	.00700	0.952	.022
1.000	.00162	0.938	0

TABLE IV
CALCULATION OF INSTABILITY
NACA 63-009; $C_L = 0.72$

First Bubble Position

$$V_s/V_o = 0.9 (2.583) = 2.325$$

$$x_s/c = 0.0046 \quad \beta_s = 0.631$$

$$x_t/c = 0.0090 \quad \beta_t = 0.485$$

$$\frac{\lambda}{c} = 2 \left(\frac{x_t}{c} - \frac{x_s}{c} \right) = 0.0088$$

$$\frac{h}{\lambda} = \frac{\beta_s - \beta_t}{2} = 0.073$$

$\frac{\Delta x/c}{\lambda/c}$	$\Delta x/c$	x/c	$\left(\frac{V_U}{V_o} \right)_o$	$\frac{\Delta V_U}{V_U} \left(\frac{\lambda}{h} \right)$	$\frac{\Delta V_U}{V_U}$	$\frac{\Delta V_U}{V_o}$	$\left(\frac{V_U}{V_o} \right)_1$
-0.5	-0.00440	0.00020	2.401	-0.21	-0.015	-.036	2.365
-0.4	-0.00352	0.00108	2.580	-0.33	-0.024	-.062	2.518
-0.3	-0.00272	0.00196	2.530	-0.48	-0.035	-.089	2.441
-0.2	-0.00192	0.00284	2.463	-0.68	-0.050	-.123	2.340
-0.15	-0.00123	0.00328	2.428	-0.82	-0.060	-.146	2.282
-0.1	-0.00088	0.00372	2.391	-1.05	-0.077	-.184	2.207
-0.05	-0.00044	0.00416	2.360	-1.27	-0.093	-.219	2.141
0	0	0.00460	2.325	-1.54	-0.112	-.260	2.065
+0.05	+0.00044	0.00504	2.300	-1.75	-0.128	-.294	2.006
+0.25	+0.00220	0.00680	2.215	+0.68	+0.050	+.111	2.326
+0.5	+0.00440	0.00900	2.125	+3.70	+0.270	+.574	2.699
+0.75	+0.00660	0.01120	2.040	+0.68	+0.050	+.102	2.142
+1.0	+0.00880	0.01340	1.953	-1.54	-0.112	-.219	1.734
+1.5	+0.01320	0.01780	--	--	--	--	--

TABLE V
CALCULATION OF INSTABILITY
NACA 63-009; $C_L = 0.72$

Second Bubble Position

$$V_s/V_o = 0.9(2.520) = 2.268$$

$$x_s/c = 0.00342 \quad \beta_s = 0.708$$

$$x_t/c = 0.00550 \quad \beta_t = 0.590$$

$$\frac{\lambda}{c} = 2 \left(\frac{x_t}{c} - \frac{x_s}{c} \right) = 0.00416$$

$$\frac{h}{\lambda} = \frac{\beta_s - \beta_t}{2} = 0.056$$

$\frac{\Delta x/c}{\lambda/c}$	$\Delta x/c$	x/c	$\left(\frac{V_U}{V_o}\right)$	$\frac{\Delta V_U}{V_U} \left(\frac{\lambda}{h}\right)$	$\frac{\Delta V_U}{V_U}$	$\frac{\Delta V_U}{V_o}$	$\left(\frac{V_U}{V_o}\right)_2$
-0.5	-0.00208	0.00134	2.572	-0.21	-0.012	-0.031	2.541
-0.4	-0.00166	0.00176	2.547	-0.33	-0.018	-0.046	2.501
-0.3	-0.00125	0.00217	2.517	-0.48	-0.027	-0.068	2.449
-0.2	-0.00083	0.00258	2.484	-0.68	-0.038	-0.094	2.390
-0.15	-0.00062	0.00279	2.469	-0.82	-0.046	-0.114	2.355
-0.10	-0.00042	0.00300	2.452	-1.05	-0.059	-0.145	2.307
-0.05	-0.00021	0.00321	2.435	-1.27	-0.071	-0.173	2.262
0	0	0.00342	2.417	-1.54	-0.086	-0.210	2.207
+0.05	+0.00021	0.00363	2.398	-1.75	-0.098	-0.235	2.163
+0.25	+0.00104	0.00446	2.335	+0.68	+0.038	+0.089	2.424
+0.50	+0.00208	0.00550	2.275	+3.70	+0.207	+0.471	2.746
+0.75	+0.00312	0.00654	2.225	+0.68	+0.038	+0.085	2.310
+1.00	+0.00416	0.00758	2.182	-1.54	-0.086	-0.186	1.996
+1.50	+0.00624	0.00966	2.099	-0.21	-0.012	-0.025	2.074

TABLE VI
CALCULATION OF INSTABILITY
NACA 63-009; $C_L = 0.72$

Third Bubble Position

$$V_s/V_o = 0.9(2.560) = 2.304$$

$$x_s/c = 0.00300 \quad \beta = 0.750$$

$$x_t/c = 0.00380 \quad \beta = 0.680$$

$$\frac{\lambda}{c} = 0.00160$$

$$\frac{h}{\lambda} = \frac{\beta_s - \beta_t}{2} = 0.035$$

$\frac{\Delta x/c}{\lambda/c}$	$\Delta x/c$	x/c	$\frac{V_U}{V_o}$	$\frac{\Delta V_U}{V_U} \left(\frac{\lambda}{h} \right)$	$\frac{\Delta V_U}{V_o}$	$\frac{\Delta u}{V_o}$	$\left(\frac{V_U}{V_o} \right)_3$
-1.0	-0.00160	0.00140	2.569	-0.13	-0.005	-0.013	2.556
-0.7	-0.00112	0.00188	2.536	-0.17	-0.006	-0.015	2.521
-0.5	-0.00080	0.00220	2.512	-0.21	-0.007	-0.018	2.494
-0.4	-0.00064	0.00236	2.500	-0.33	-0.012	-0.030	2.470
-0.3	-0.00048	0.00252	2.489	-0.48	-0.017	-0.042	2.447
-0.2	-0.00032	0.00268	2.476	-0.68	-0.024	-0.059	2.417
-0.15	-0.00024	0.00276	2.469	-0.82	-0.029	-0.072	2.397
-0.10	-0.00016	0.00284	2.463	-1.05	-0.037	-0.091	2.372
-0.05	-0.00008	0.00292	2.459	-1.27	-0.044	-0.108	2.351
0	0	0.00300	2.453	-1.54	-0.054	-0.132	2.321
+0.05	+0.00008	0.00308	2.446	-1.75	-0.061	-0.149	2.297
+0.25	+0.00040	0.00340	2.418	+0.68	+0.024	+0.058	2.476
+0.50	+0.00080	0.00380	2.384	+3.70	+0.130	+0.310	2.694
+0.75	+0.00120	0.00420	2.354	+0.68	+0.024	+0.056	2.410
+1.00	+0.00160	0.00460	2.325	-1.54	-0.054	-0.125	2.200
+1.50	+0.00240	0.00540	2.280	-0.21	-0.007	-0.016	2.264

TABLE VII
CALCULATION OF INSTABILITY
NACA 63-009; $C_L = 0.72$

Fourth Bubble Position

$$V_s/V_o = 0.9(2.572) = 2.315$$

$$x_s/c = 0.00298 \quad \beta = 0.750$$

$$x_t/c = 0.00370 \quad \beta = 0.686$$

$$\frac{\lambda}{c} = 0.00144$$

$$\frac{h}{\lambda} = 0.032$$

$\frac{\Delta x/c}{\lambda/c}$	$\Delta x/c$	x/c	$\frac{V_U}{V_o}$	$\frac{\Delta V_U}{V_o} \left(\frac{\lambda}{h} \right)$	$\frac{\Delta V_o}{V_U}$	$\frac{\Delta V_U}{V_o}$	$\left(\frac{V_U}{V_o} \right)_4$
-1.0	-0.00144	0.00154	2.562	-0.13	-0.004	-0.010	2.552
-0.7	-0.00101	0.00197	2.528	-0.17	-0.005	-0.013	2.515
-0.5	-0.00072	0.00228	2.505	-0.21	-0.007	-0.017	2.488
-0.4	-0.00060	0.00242	2.498	-0.33	-0.011	-0.027	2.471
-0.3	-0.0043	0.00256	2.484	-0.48	-0.015	-0.037	2.447
-0.2	-0.0029	0.00270	2.472	-0.68	-0.022	-0.054	2.418
-0.15	-0.0022	0.00277	2.469	-0.82	-0.026	-0.064	2.405
-0.10	-0.0014	0.00284	2.463	-1.05	-0.034	-0.084	2.379
-0.05	-0.0007	0.00291	2.459	-1.27	-0.041	-0.100	2.359
0	0	0.00298	2.455	-1.54	-0.049	-0.120	2.335
+0.05	+0.0007	0.00305	2.450	-1.75	-0.056	-0.137	2.313
+0.25	+0.0036	0.00334	2.425	+0.68	+0.022	+0.053	2.478
+0.50	+0.0070	0.00370	2.392	+3.70	+0.118	+0.282	2.674
+0.75	+0.0108	0.00406	2.363	+0.68	+0.022	+0.052	2.415
+1.00	+0.0144	0.00442	2.339	-1.54	-0.049	-0.115	2.224
+1.50	+0.0216	0.00514	2.296	-0.21	-0.007	-0.016	2.280

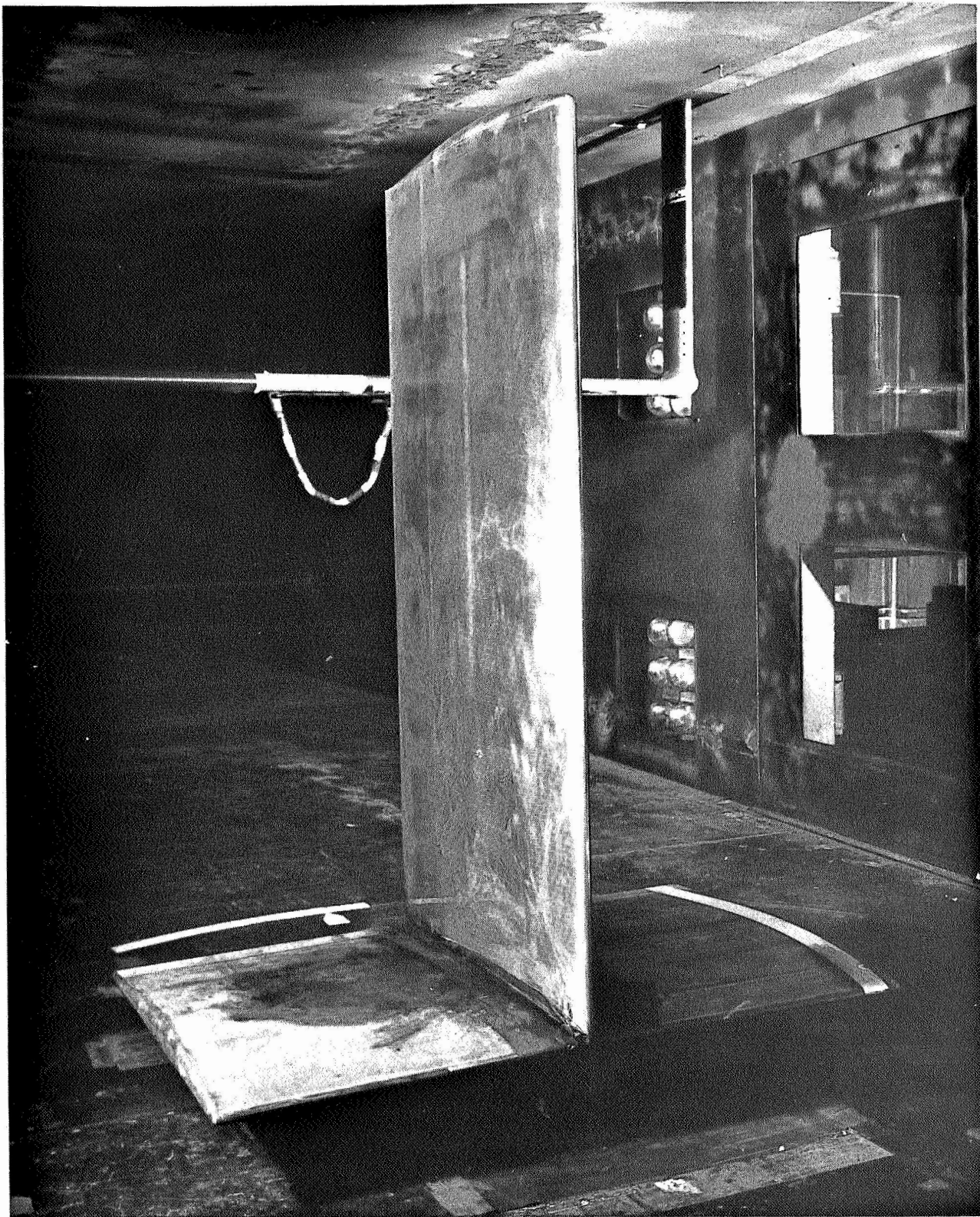
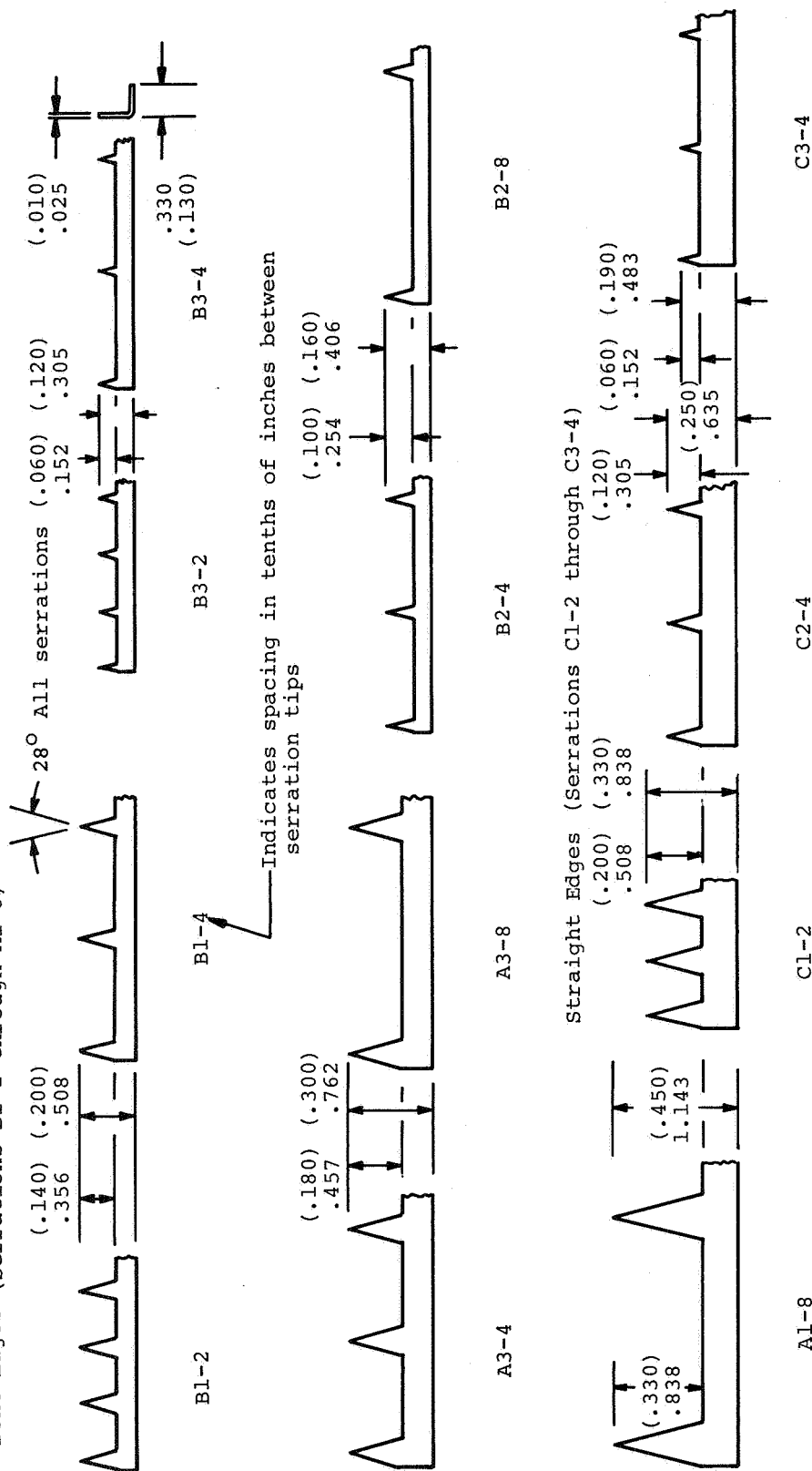


Figure 1.- Wing installed in Ames
7×10-Foot Wind Tunnel.

90° Bent Edges (Serrations B1-2 through A1-8)



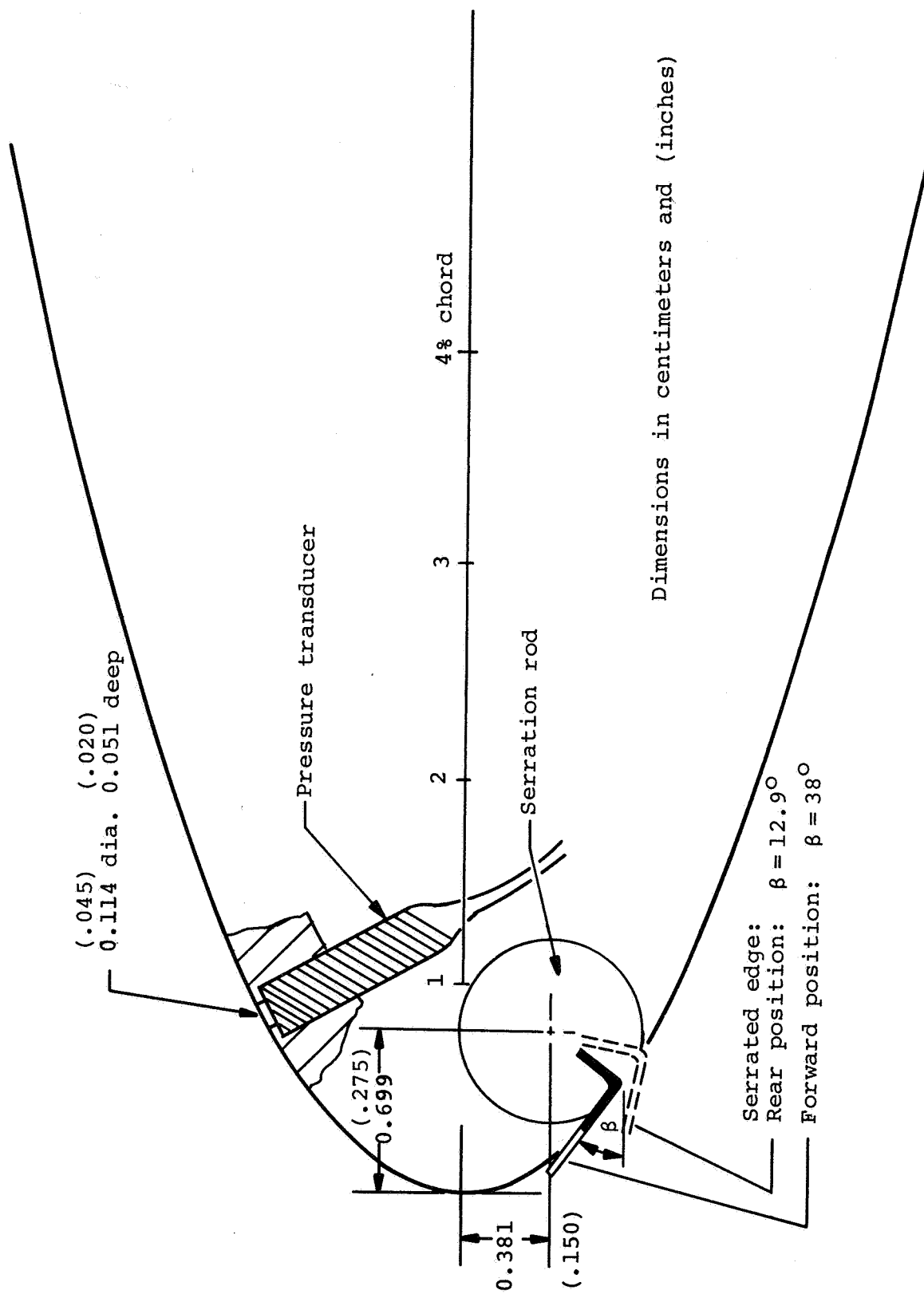


Figure 3.- Leading-edge cross section showing serrated edge .
and pressure transducer installation.

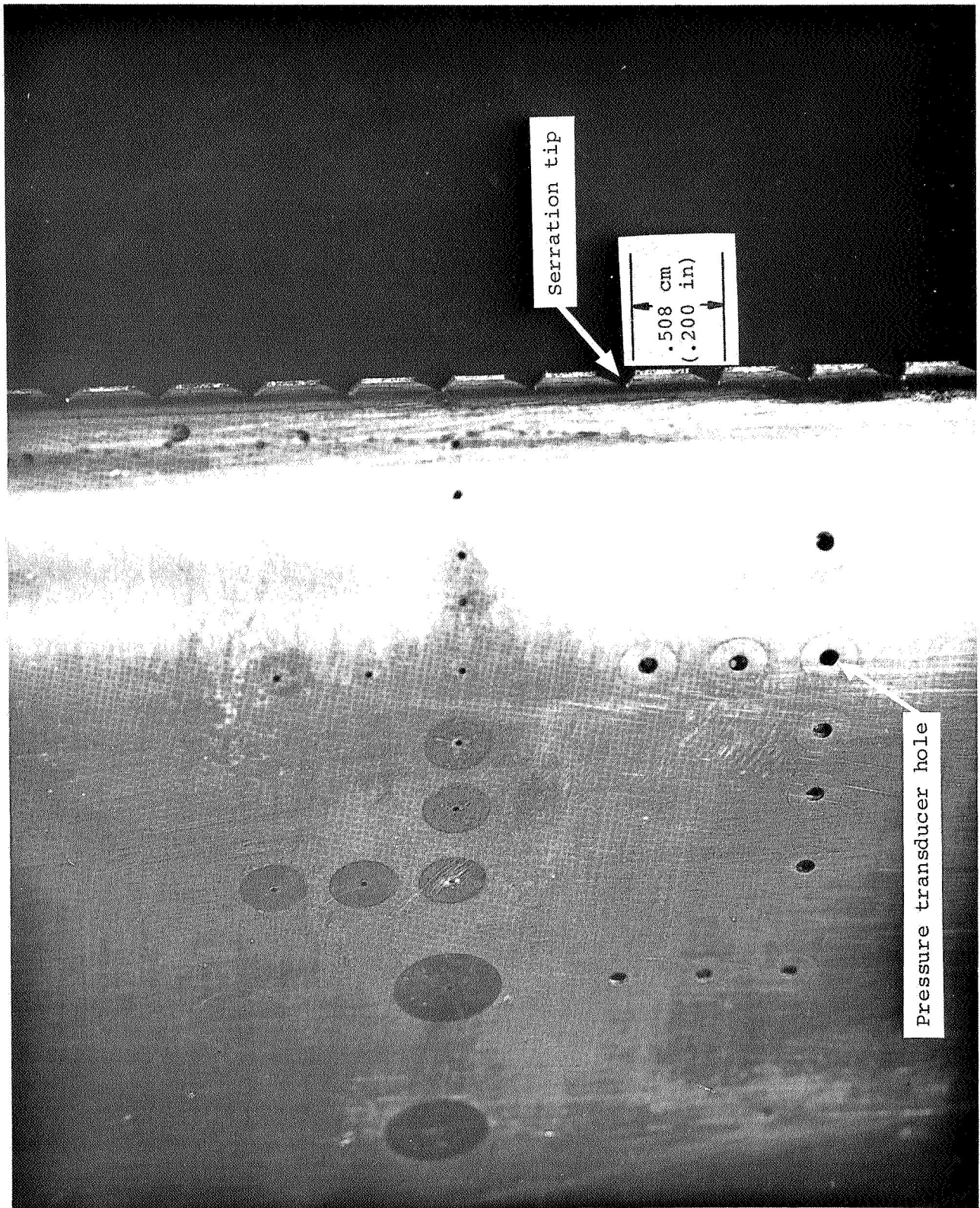


Figure 4.- Leading edge, 40 percent span region, serrated edge on right (see text).

Kulite Transducer

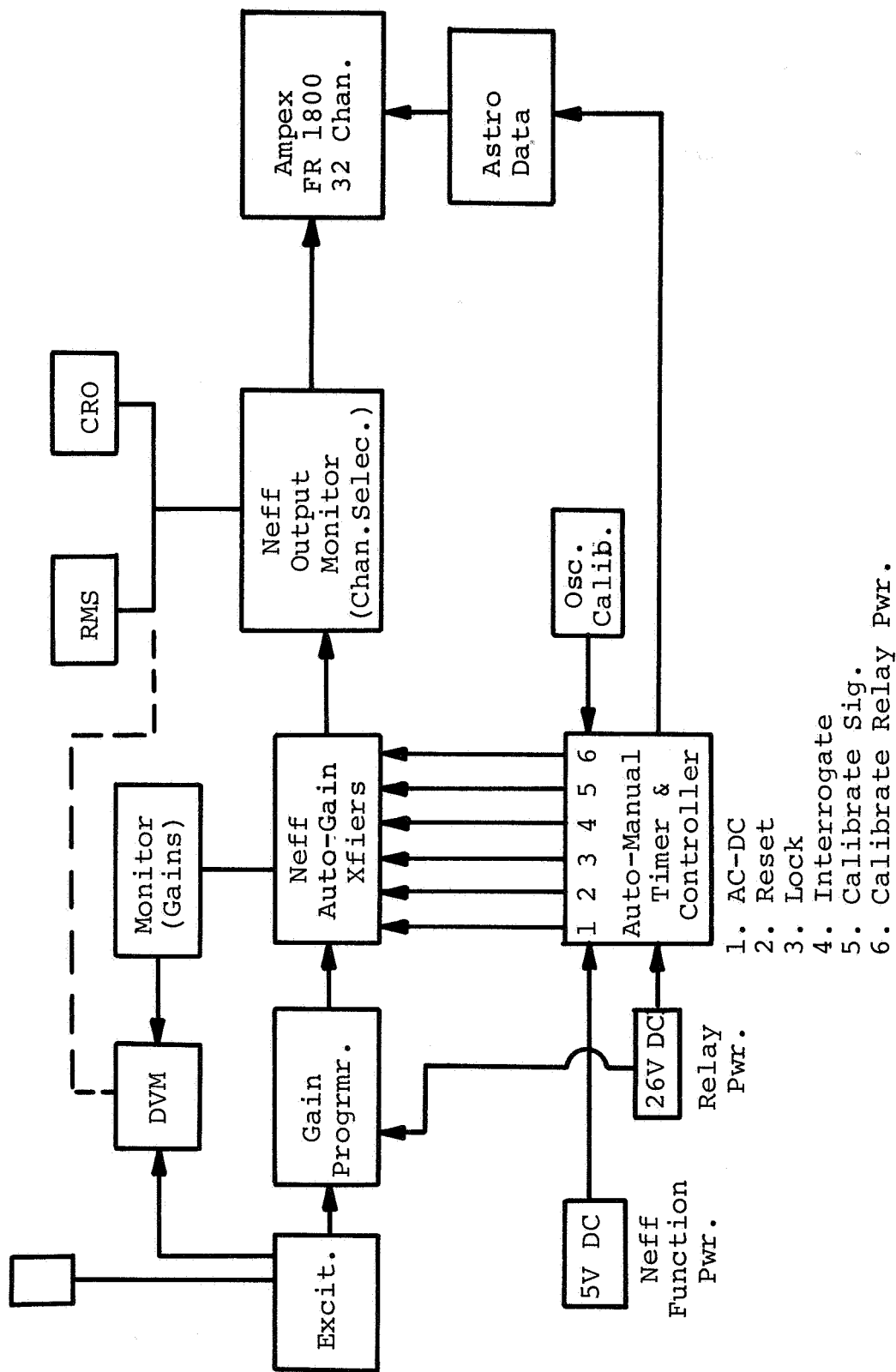


Figure 5.- Data acquisition system of Aircraft Structures Branch.

1. AC-DC
2. Reset
3. Lock
4. Interrogate
5. Calibrate Sig.
6. Calibrate Relay Pwr.

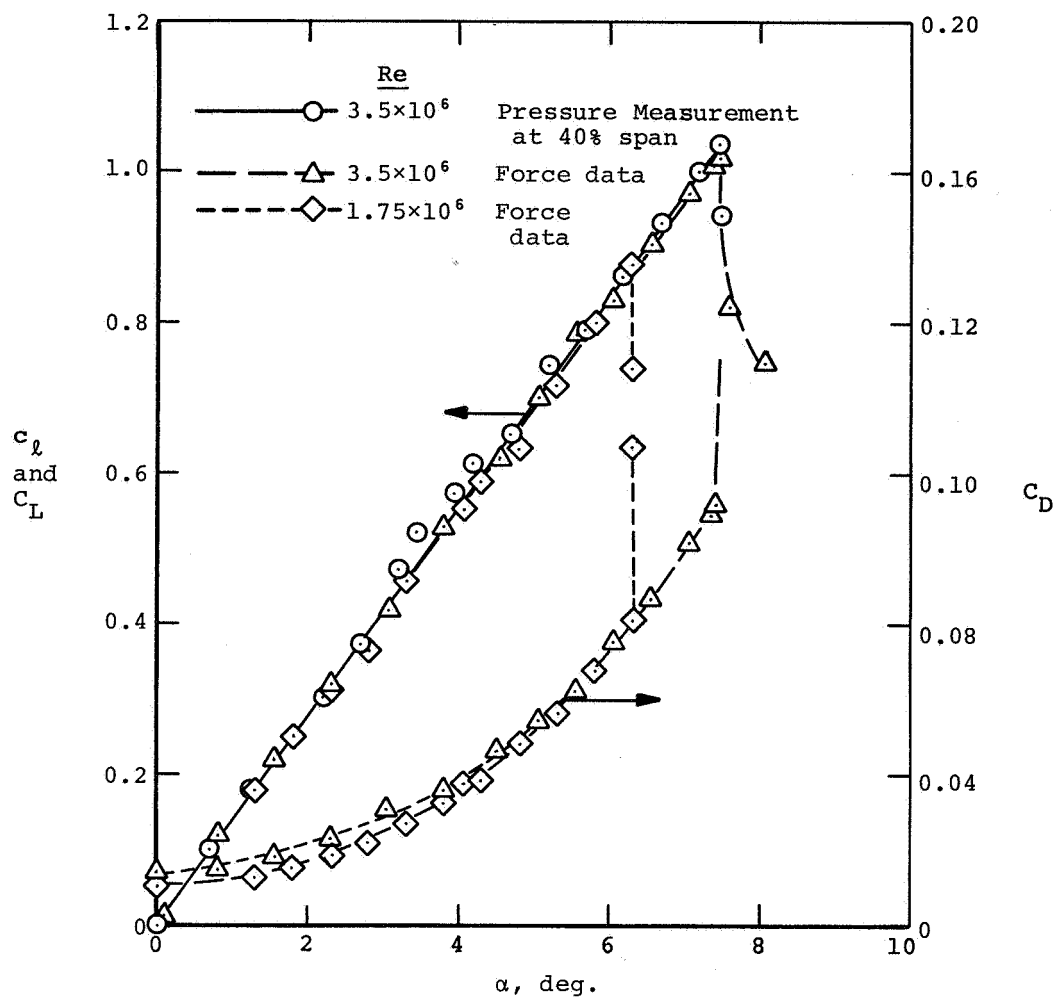


Figure 6.- Basic airfoil lift and drag.

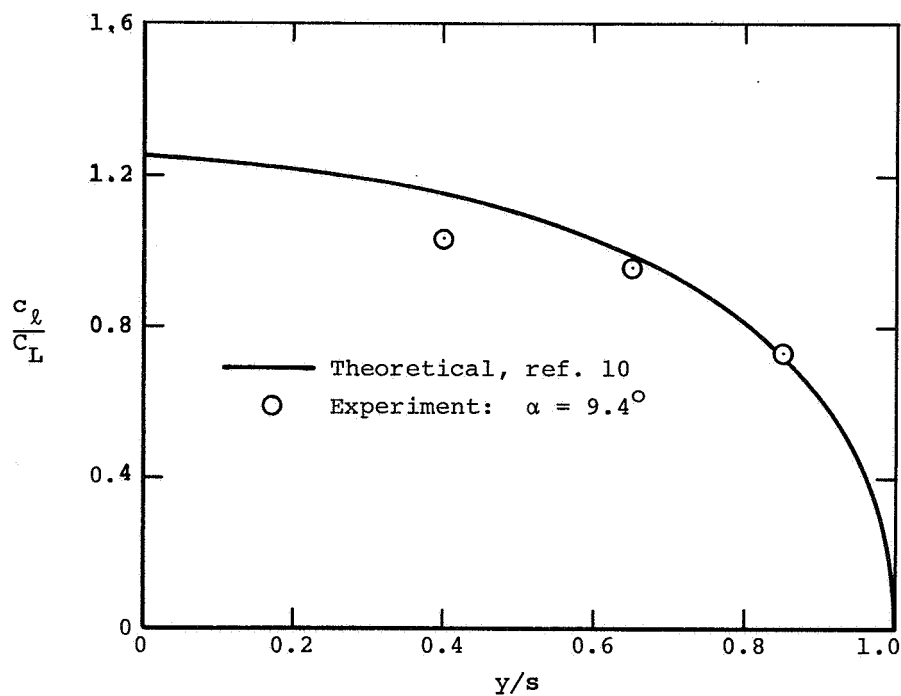


Figure 7.- Airfoil spanwise lift distribution.

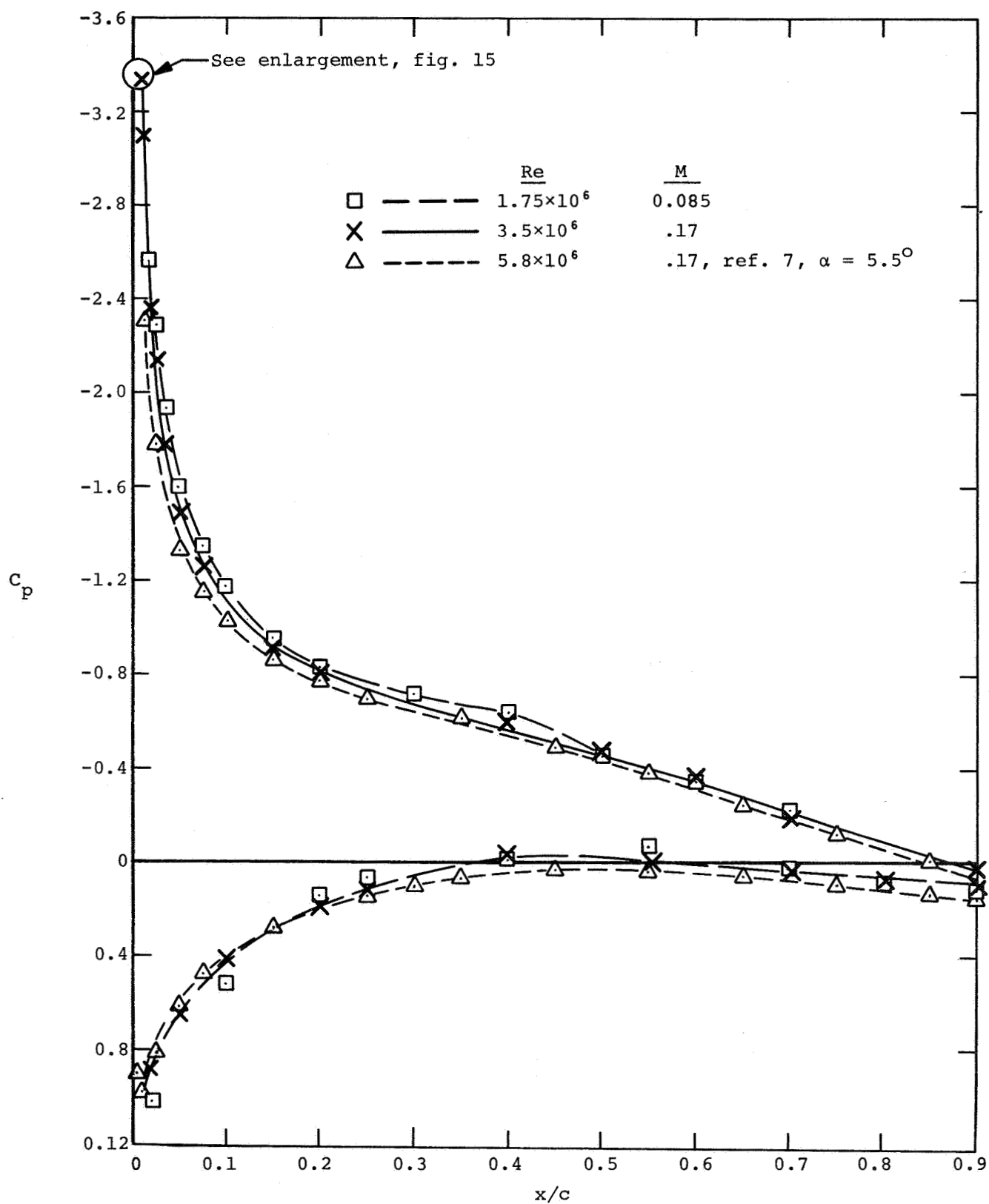
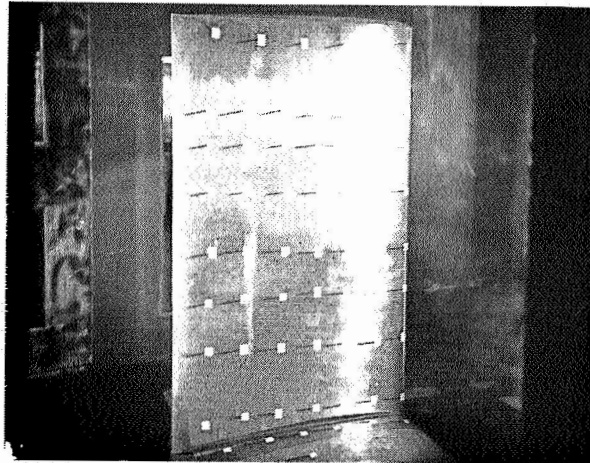
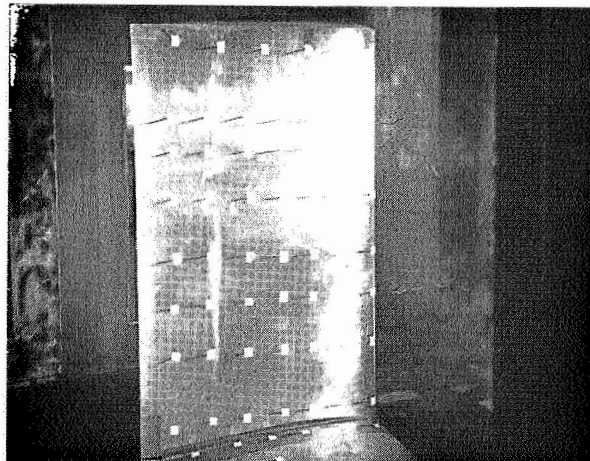


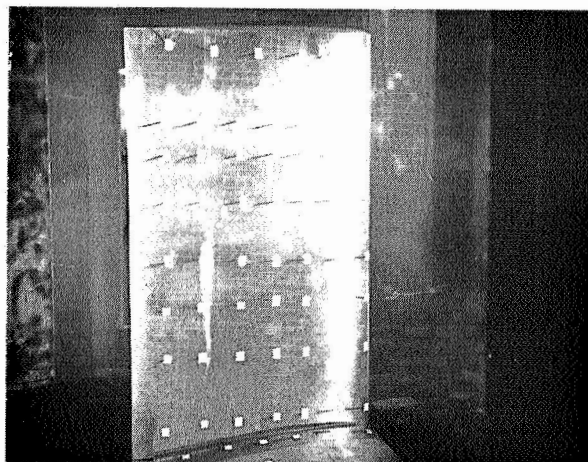
Figure 8.- Pressure distribution at 40% span; basic airfoil,
 $\alpha = 9.4^\circ$, $c_l = 0.665$.



$\alpha = 9^\circ$



$\alpha = 12^\circ$



$\alpha = 14.1^\circ$

Figure 9.- Suction side of airfoil with tufts,
 $Re = 3.5 \times 10^6$.

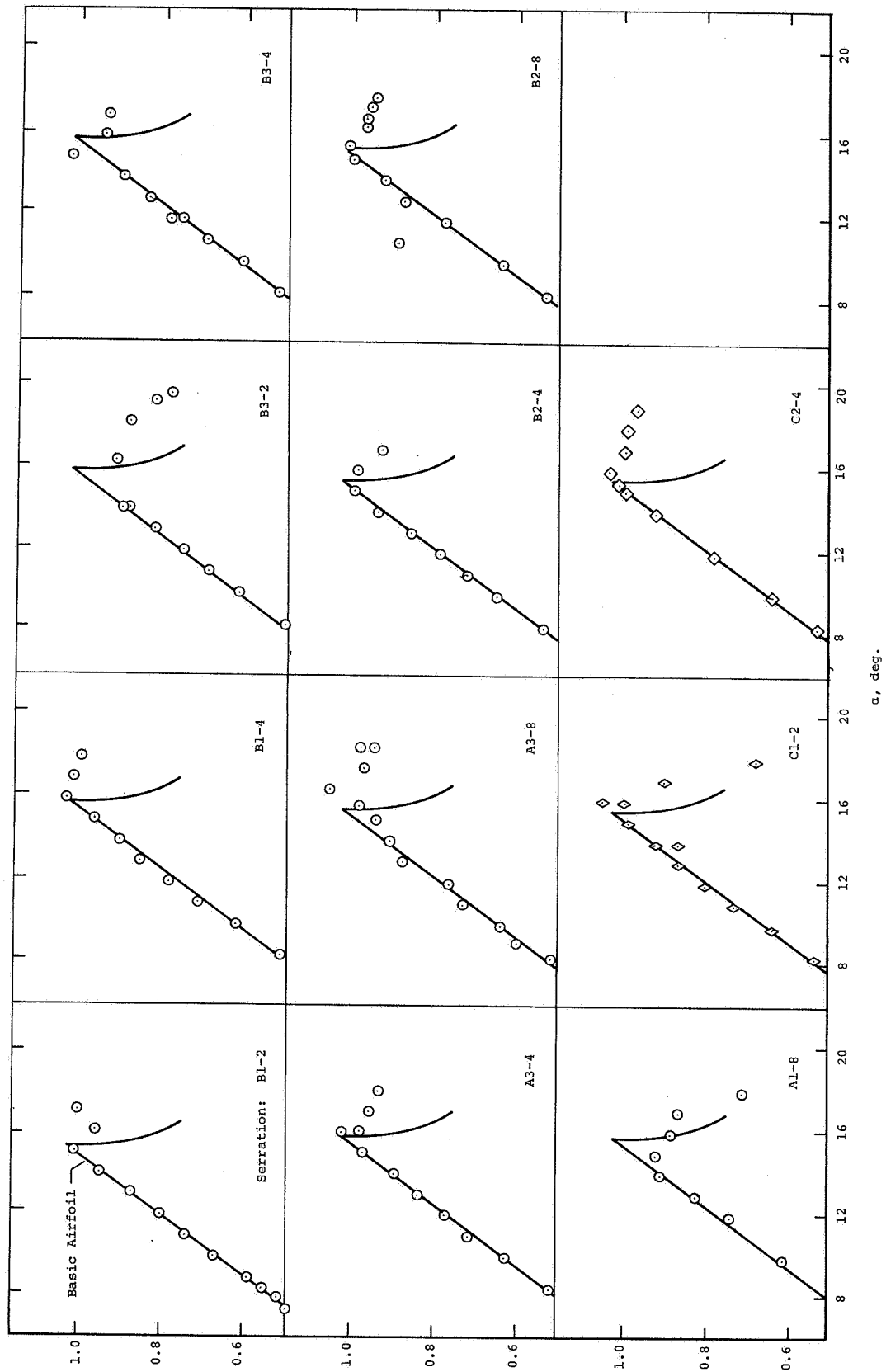


Figure 10.- Effects of serrations on lift vs. angle of attack.

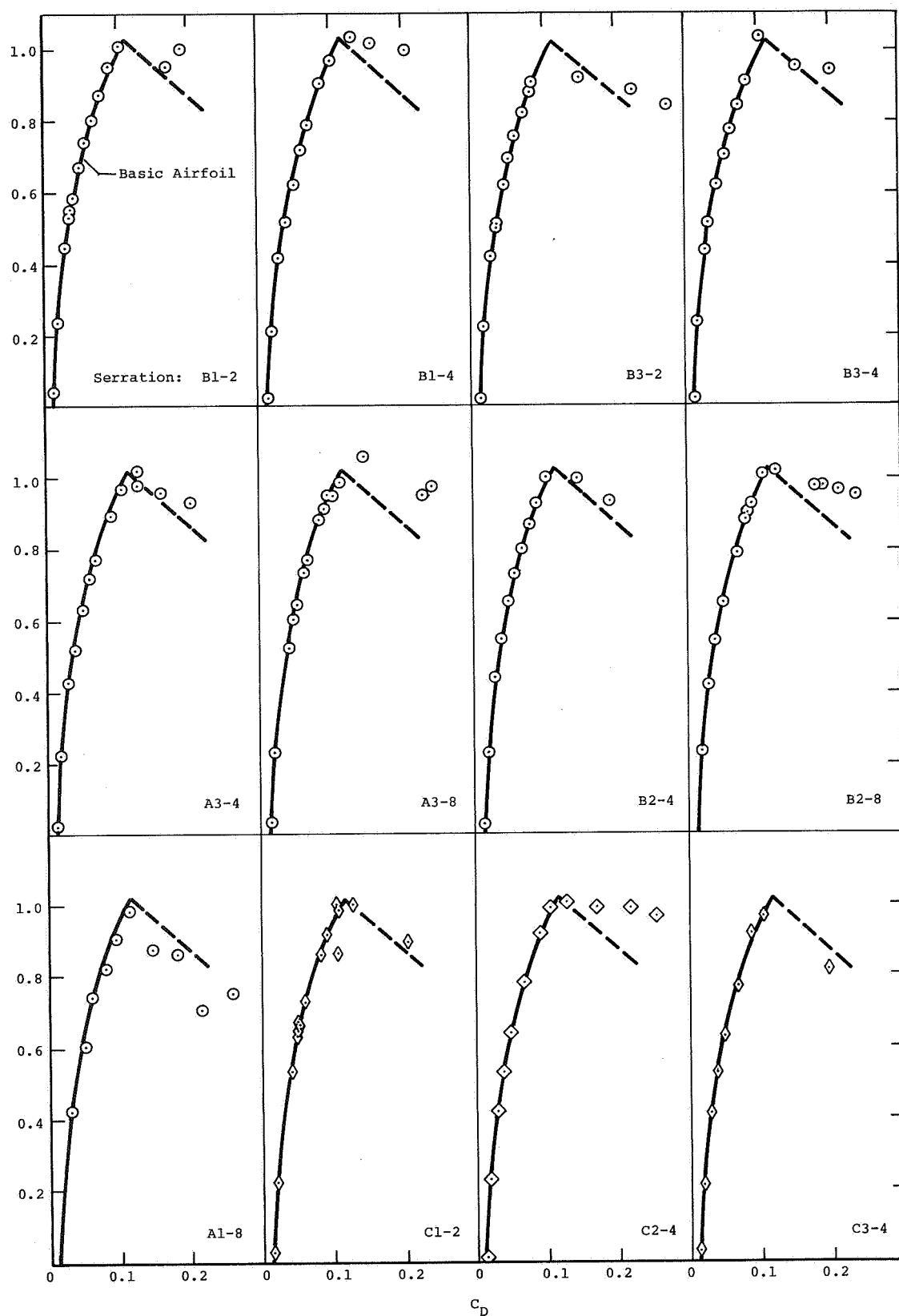


Figure 11.- Effects of serrations on lift-drag polar.

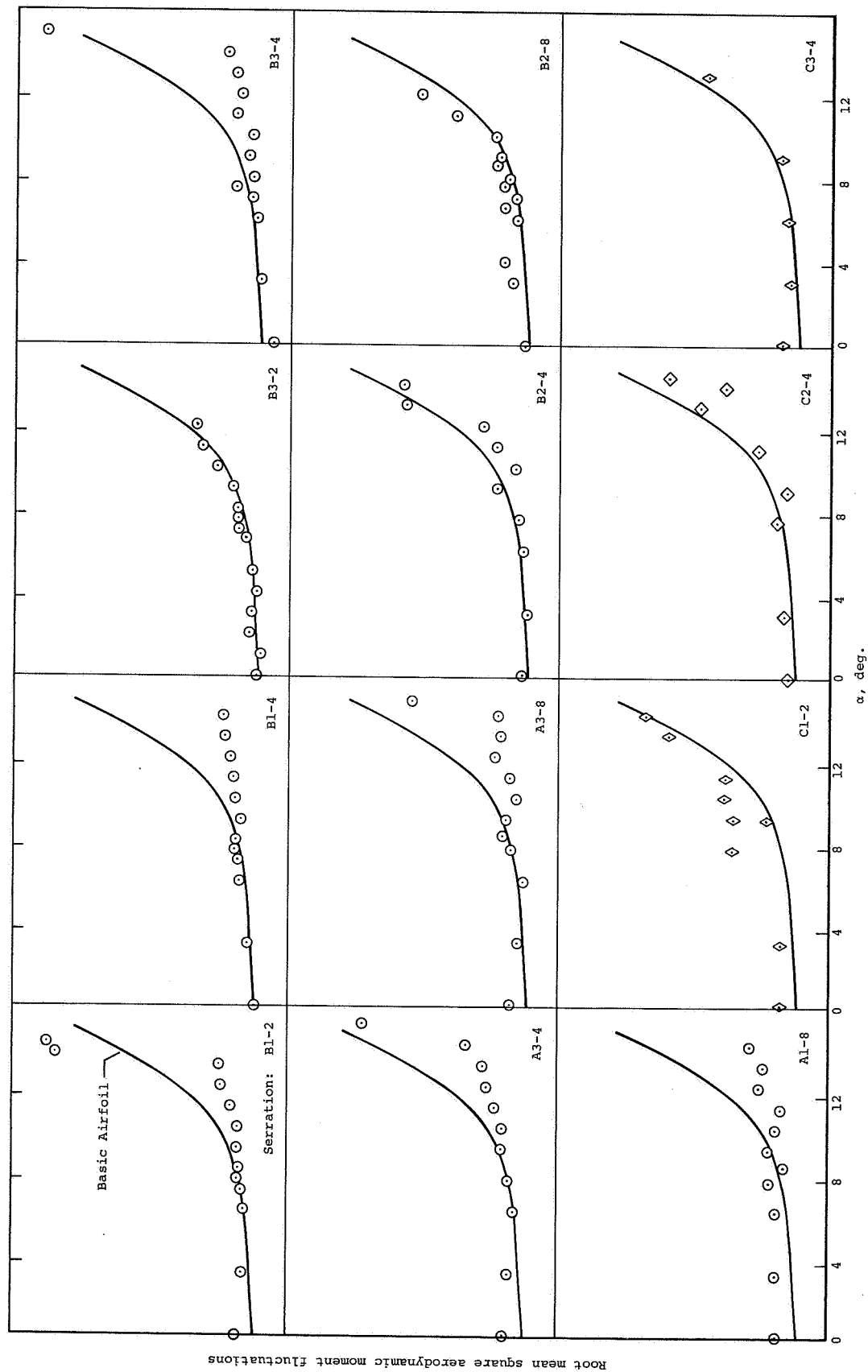


Figure 12.- Effects of serrations on root mean square of wing aerodynamic moment fluctuations about airfoil quarter-chord.

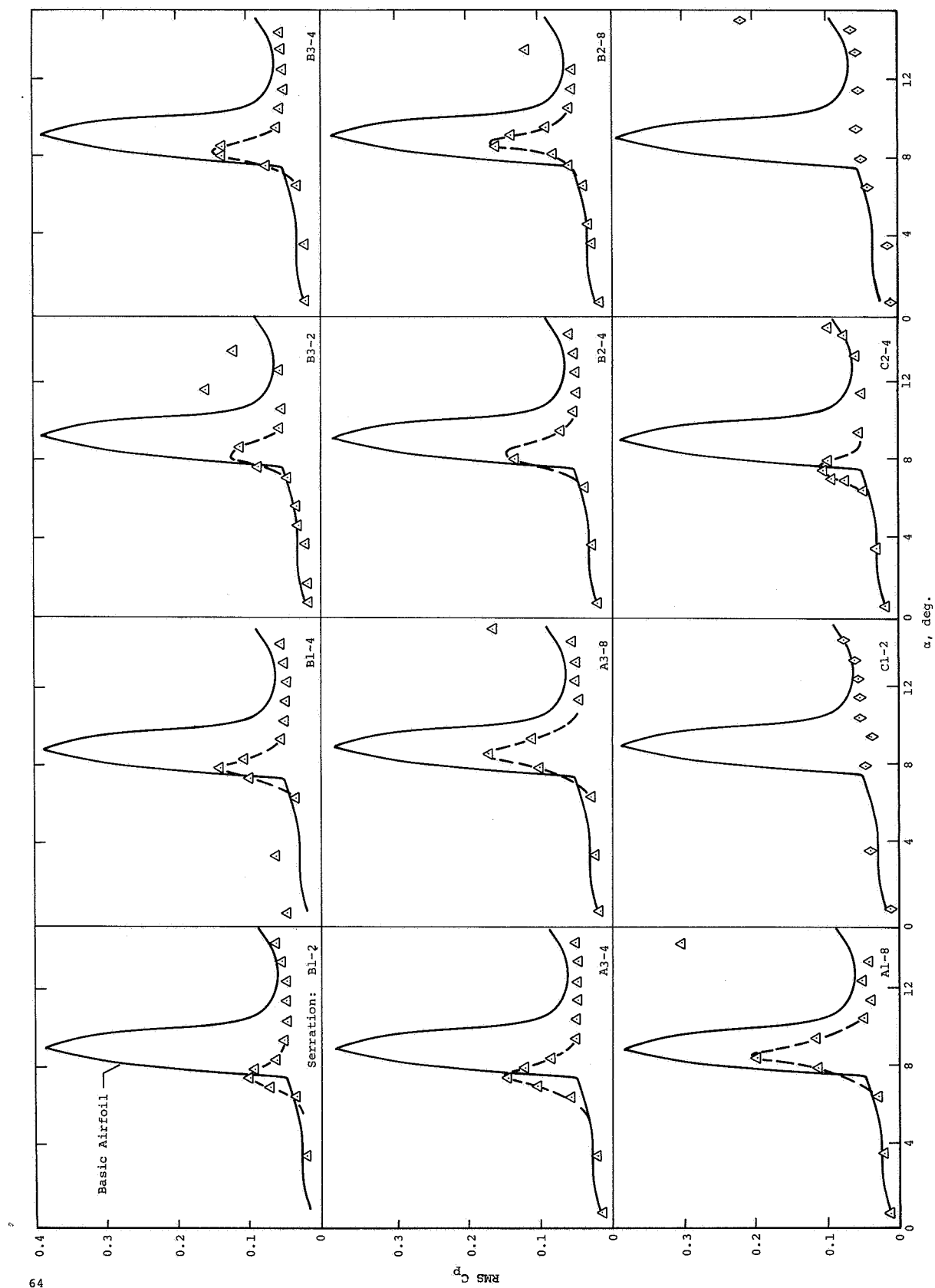


Figure 13.- Effects of serrations on root-mean-square pressure at $x/c = 0.0083$.

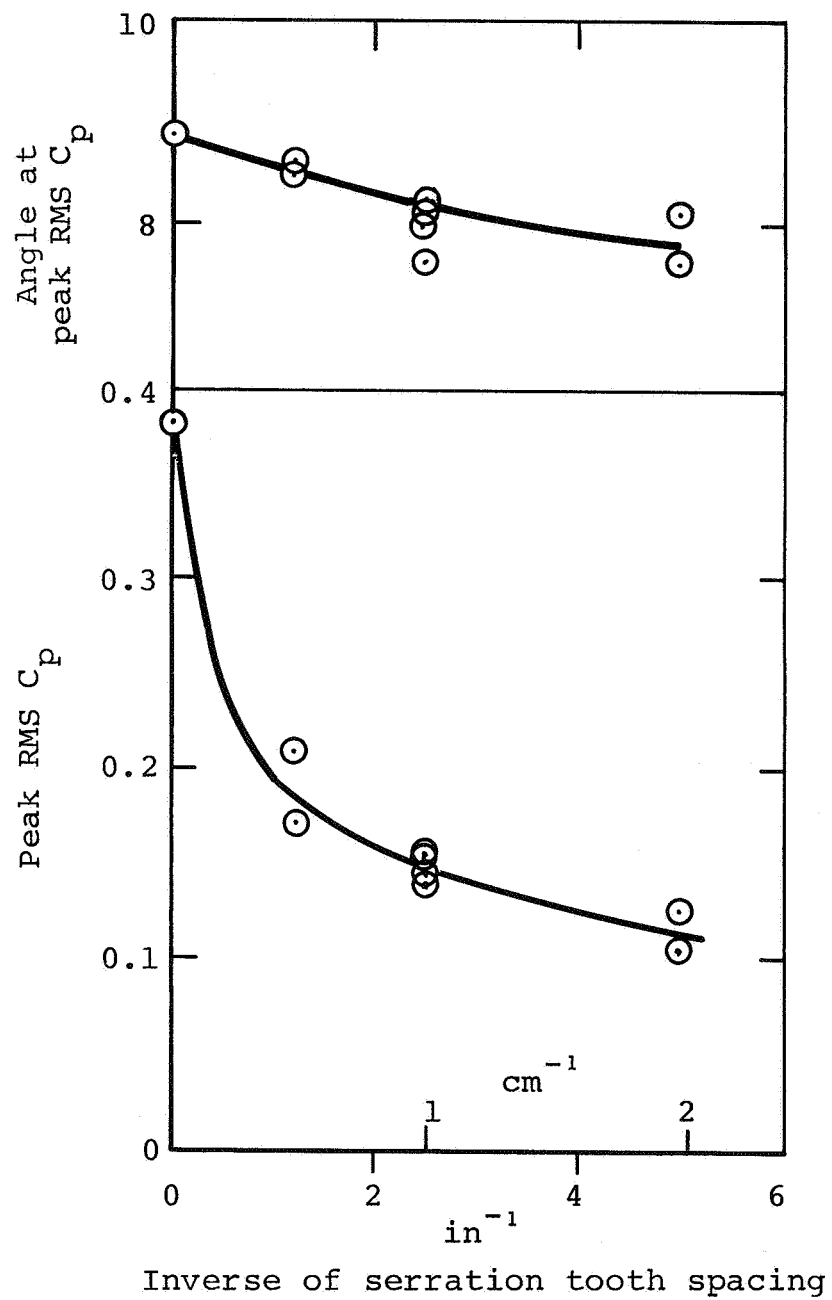


Figure 14.- Effect of serration spacing on peak RMS C_p .

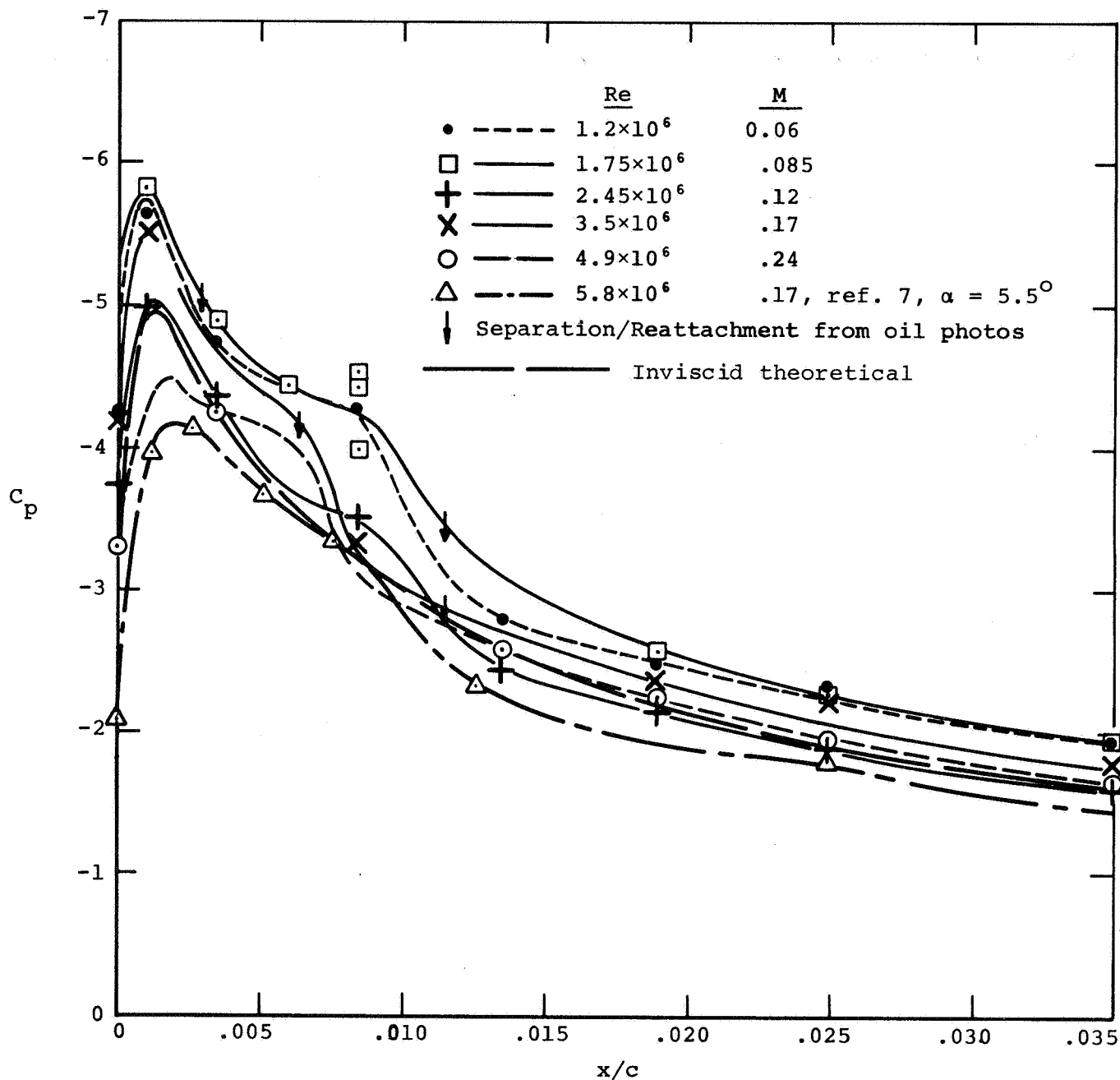


Figure 15.- Pressure distribution at 40% span, suction side of leading-edge region; basic airfoil, $\alpha = 9.4^\circ$, $c_l = 0.67$.

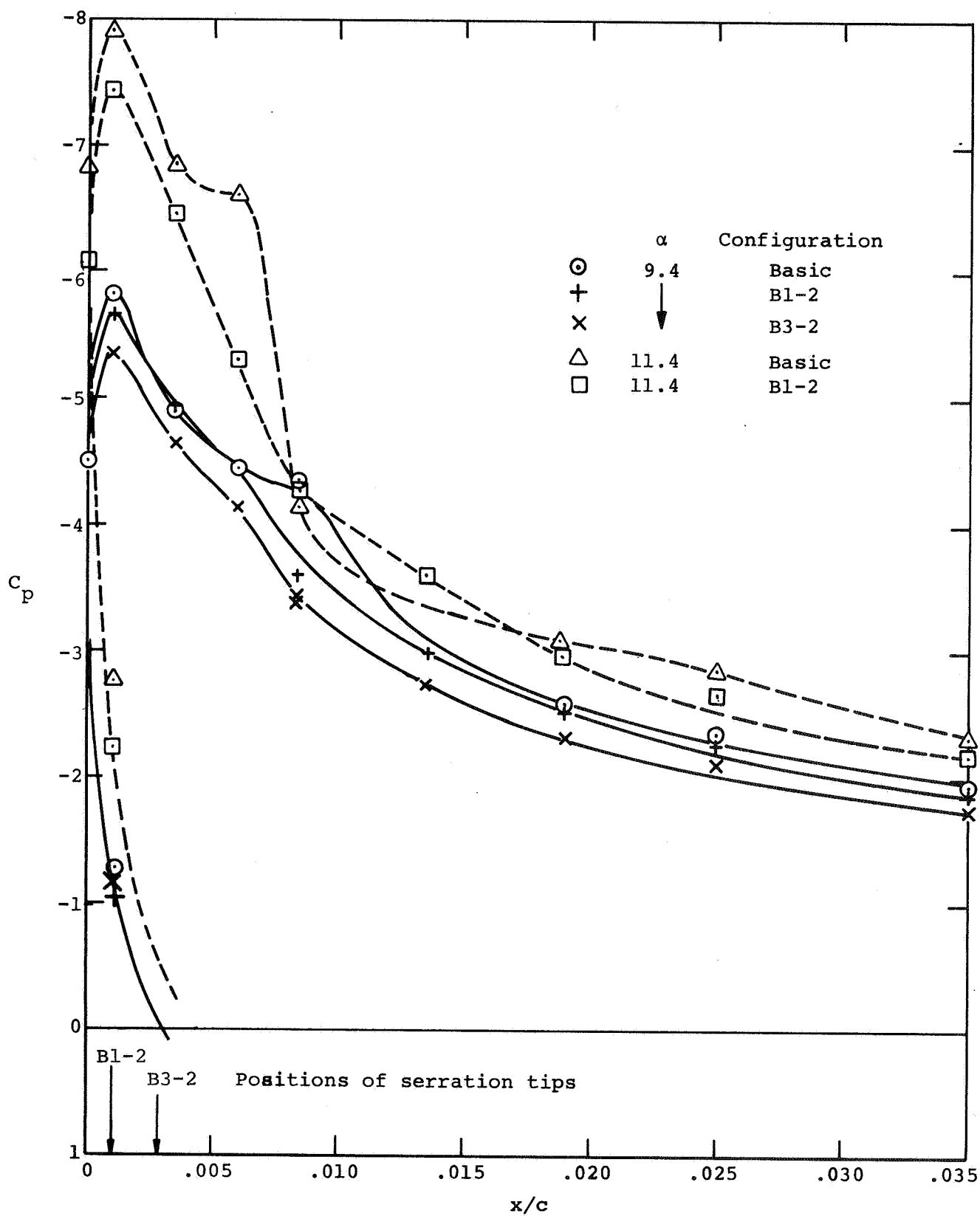


Figure 16.- Pressure distribution at 40% span, leading-edge region, with and without serrations, $Re = 1.75 \times 10^6$.

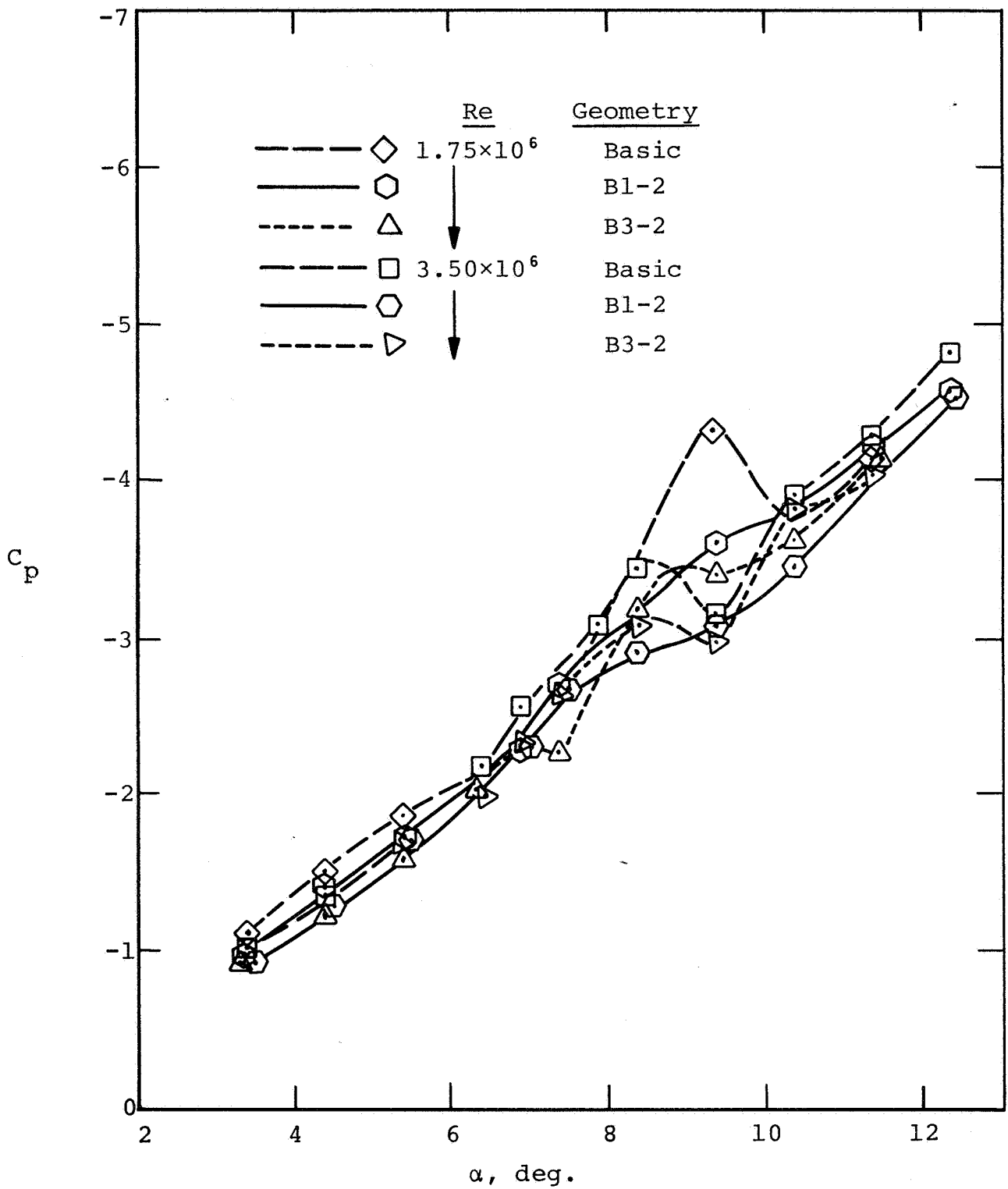
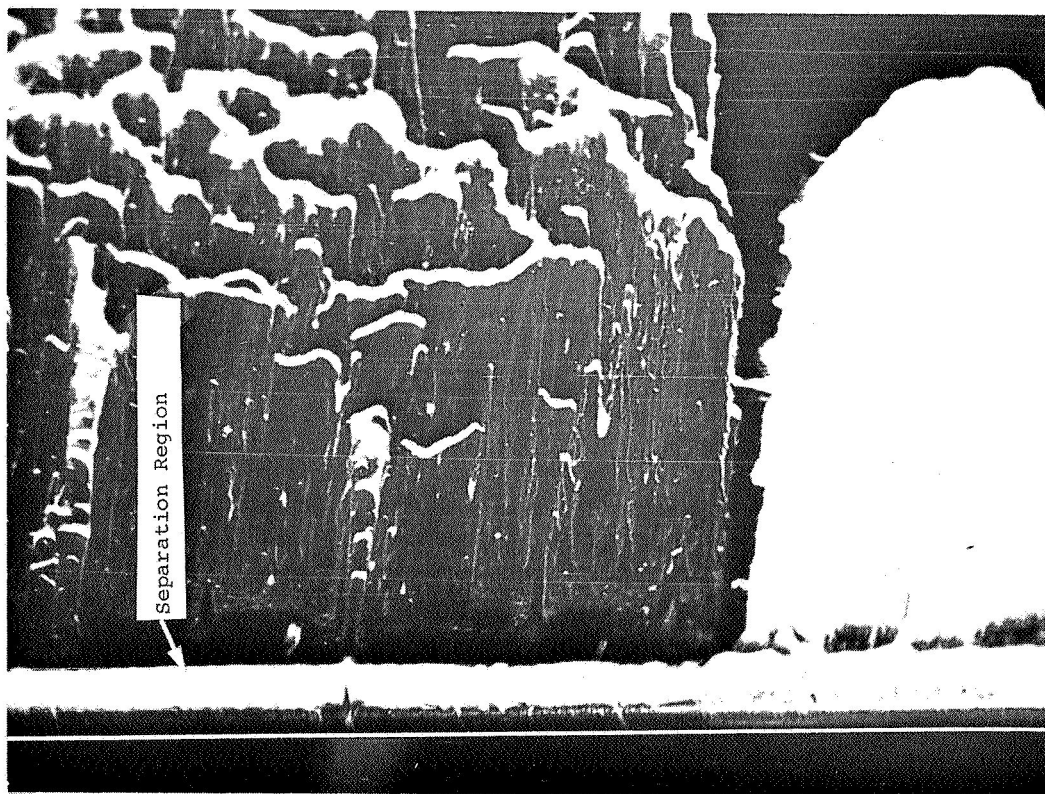
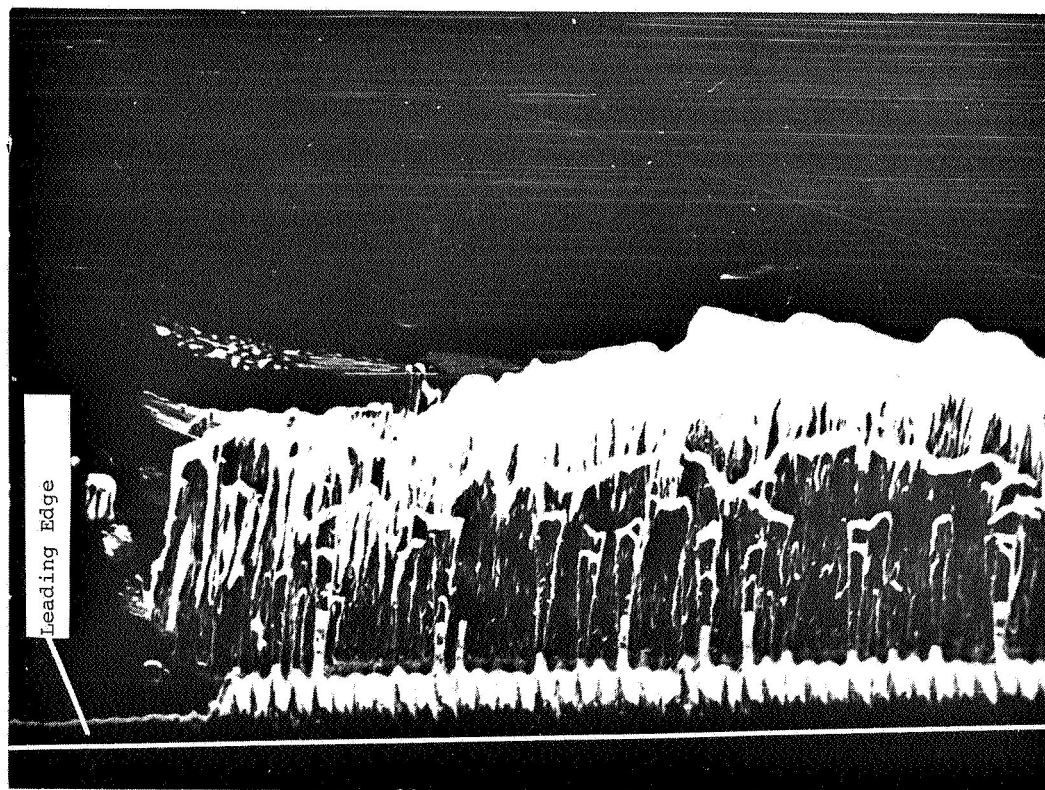


Figure 17.- C_p at $x/c = 0.0083$ versus angle of attack.

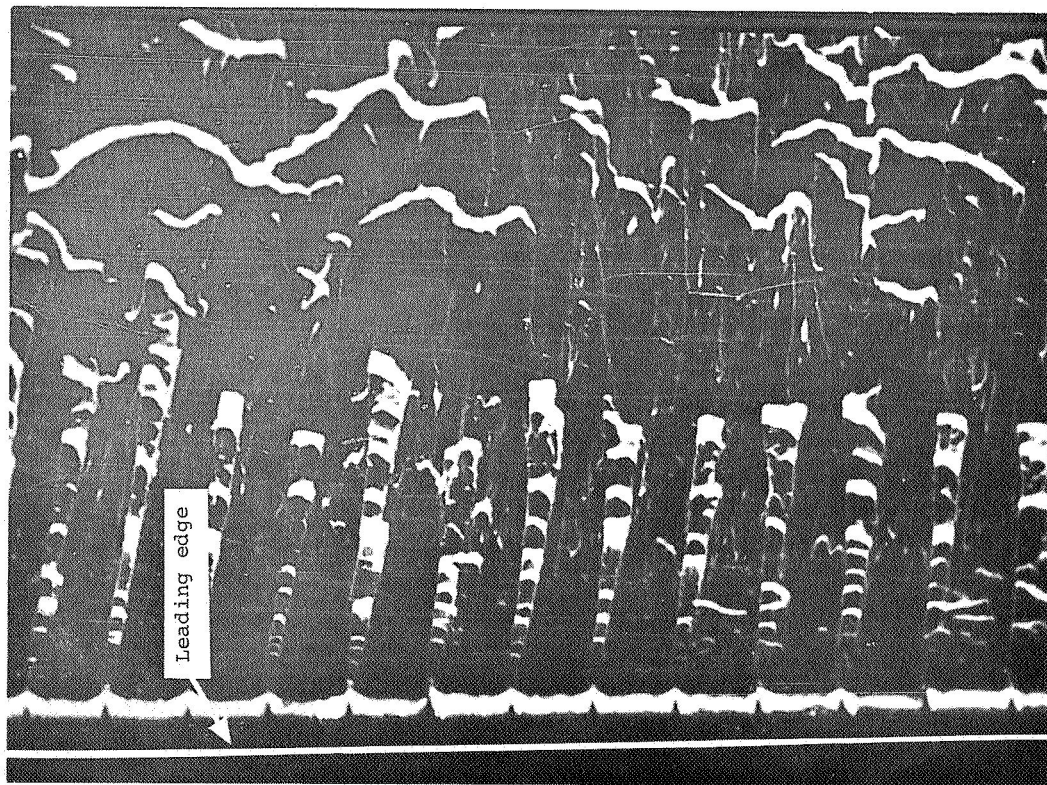


(a) Clean airfoil - two patterns from two viscosities of oil.

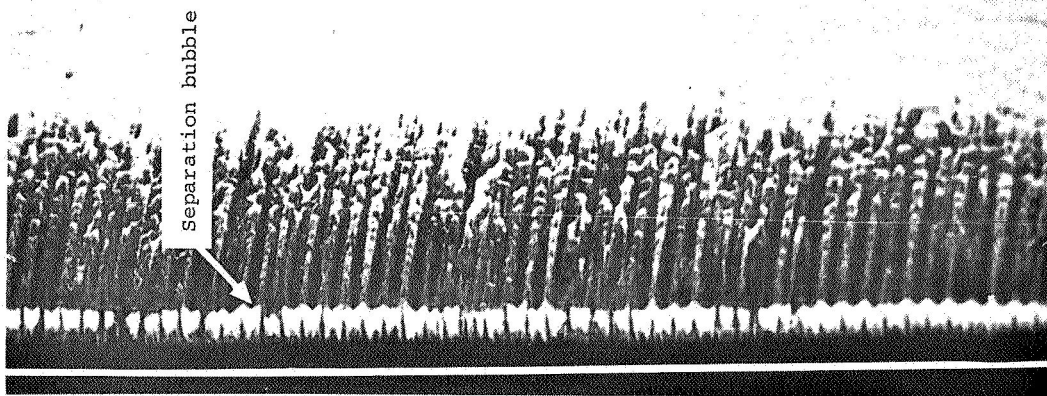


(b) With serrated edge Bl-2.

Figure 18.- Airfoil suction surface flow patterns using phosphorescent oil, flow is left to right; $\alpha = 90^\circ$, $Re = 1.75 \times 10^6$.



(a) With serrated edge B2-8, $Re = 1.75 \times 10^6$.



(b) With serrated edge B1-2, $Re = 3.5 \times 10^6$.

Figure 19.- Airfoil suction surface flow patterns using phosphorescent oil, $\alpha = 90^\circ$.

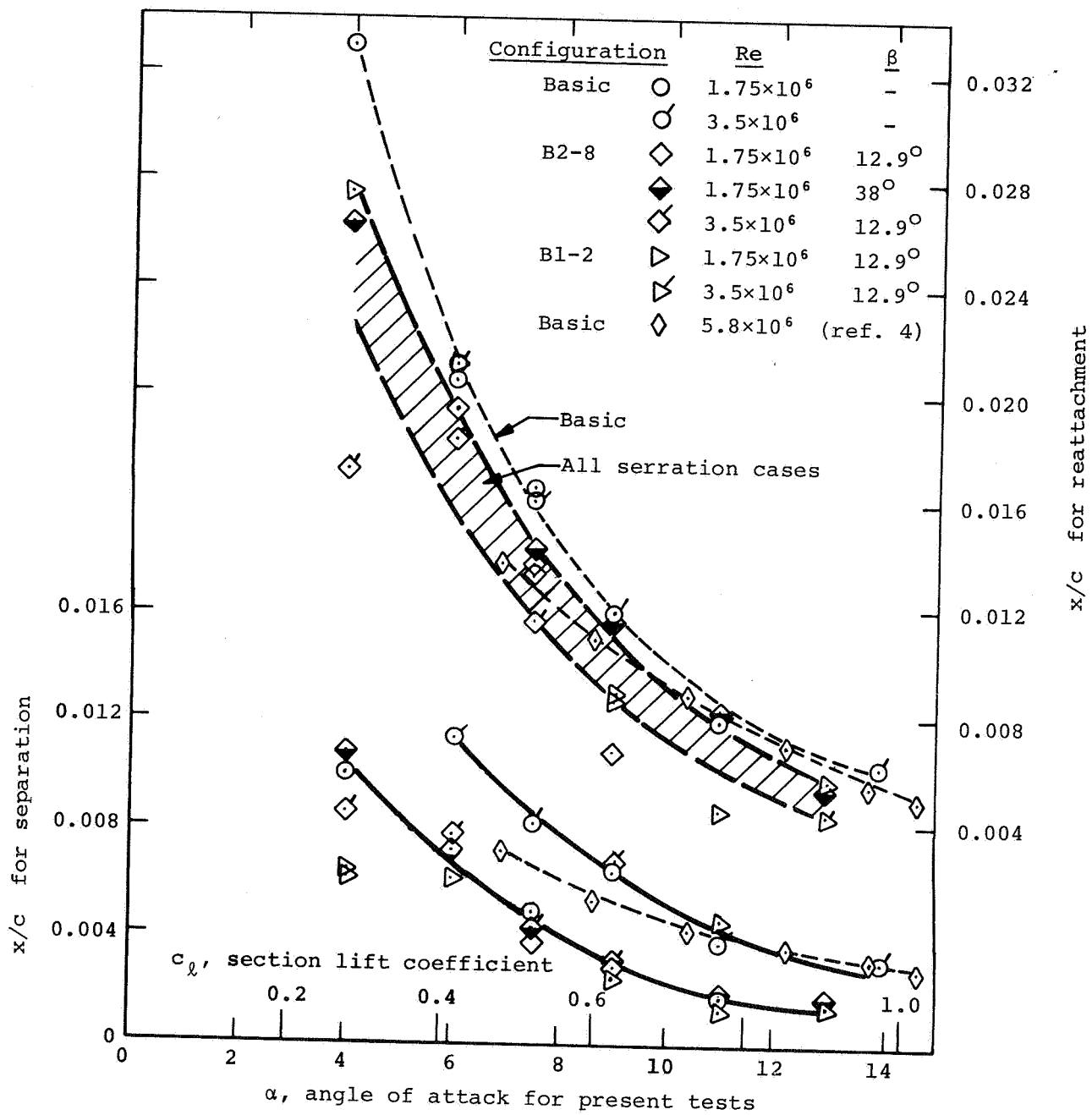


Figure 20.- Bubble separation and reattachment positions on NACA 63-009.

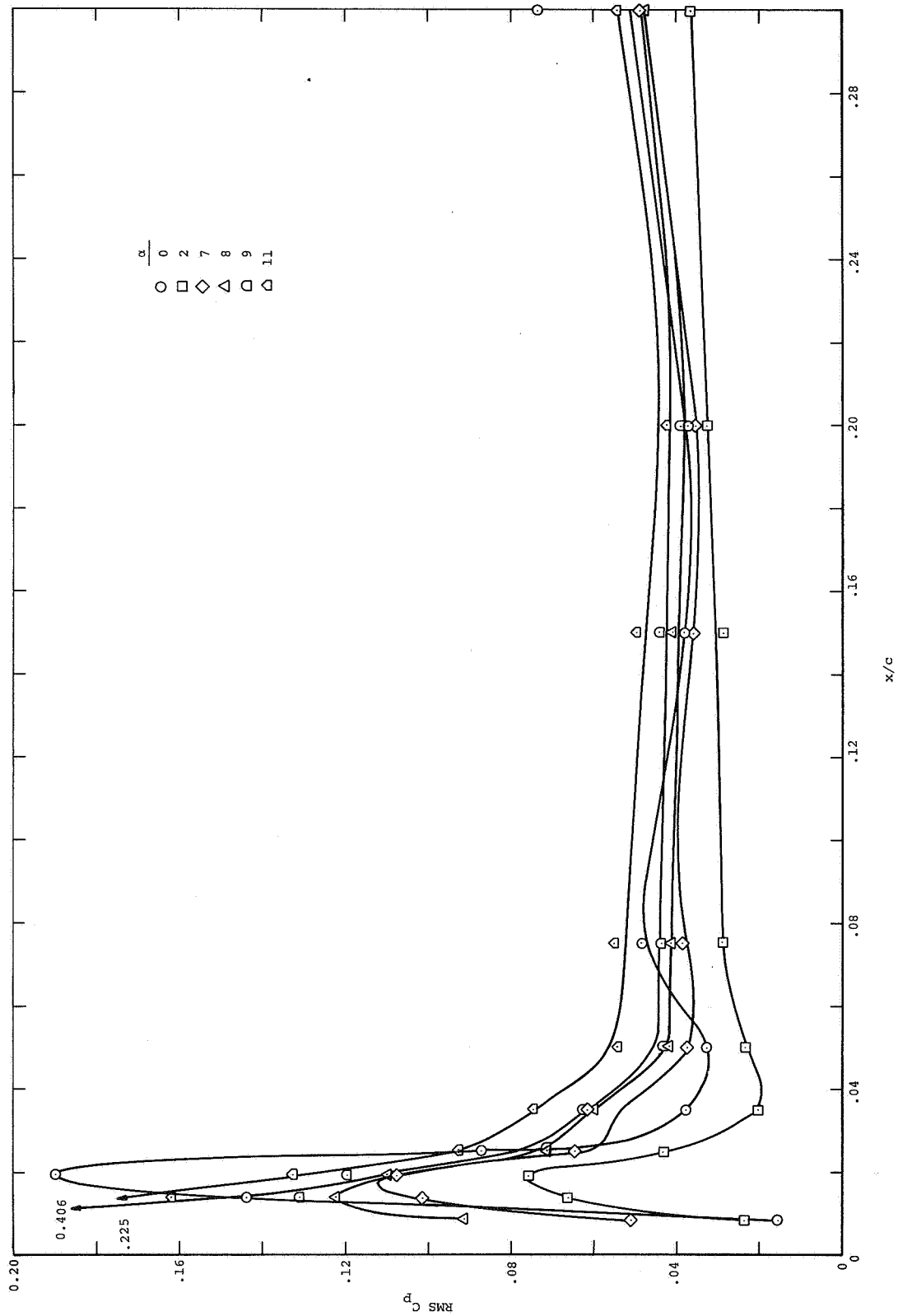


Figure 21.- Root mean square C_p along airfoil surface;
basic airfoil, $Re = 1.75 \times 10^6$.

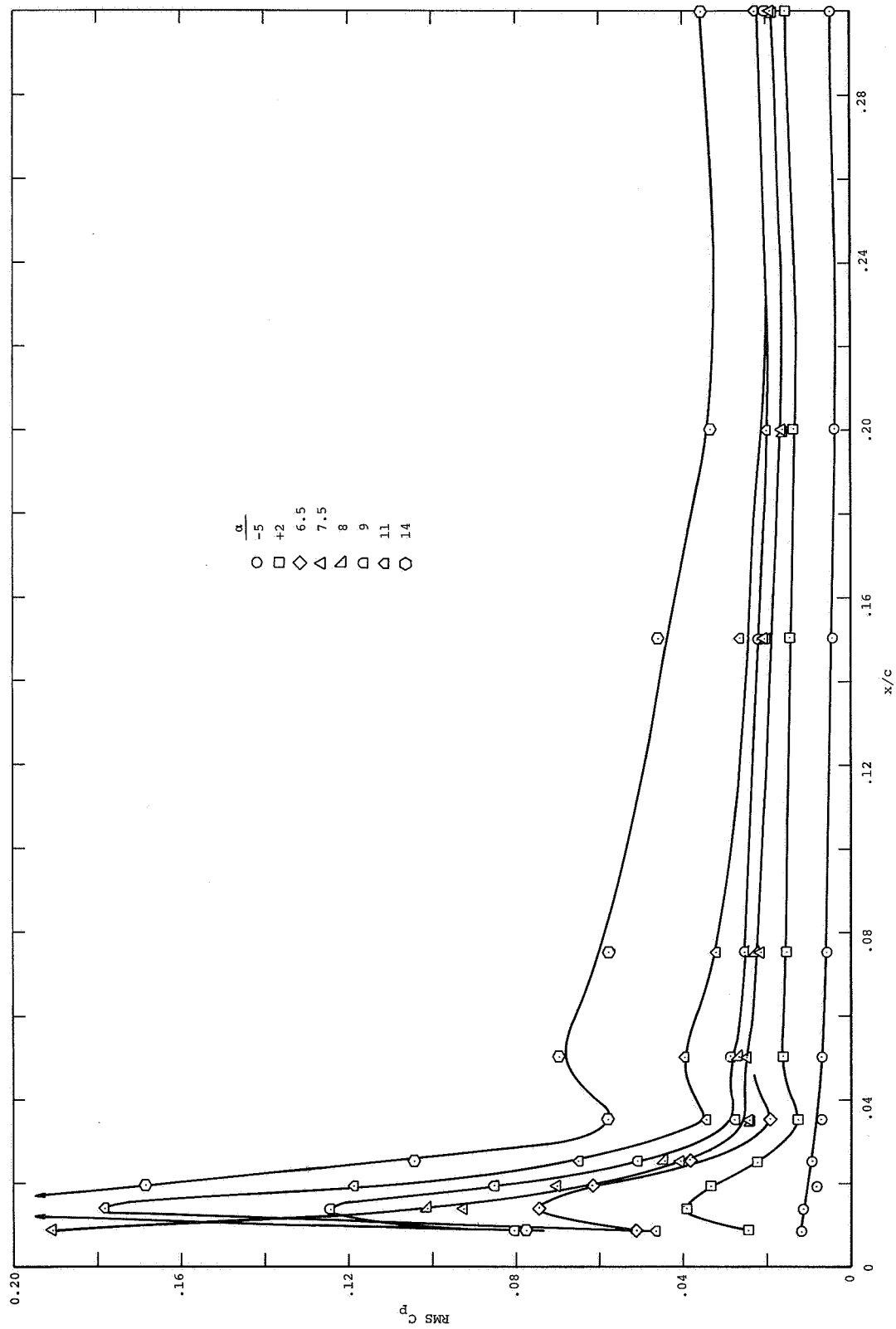


Figure 22.- Root mean square C_p along airfoil surface,
basic airfoil, $Re = 3.5 \times 10^6$.

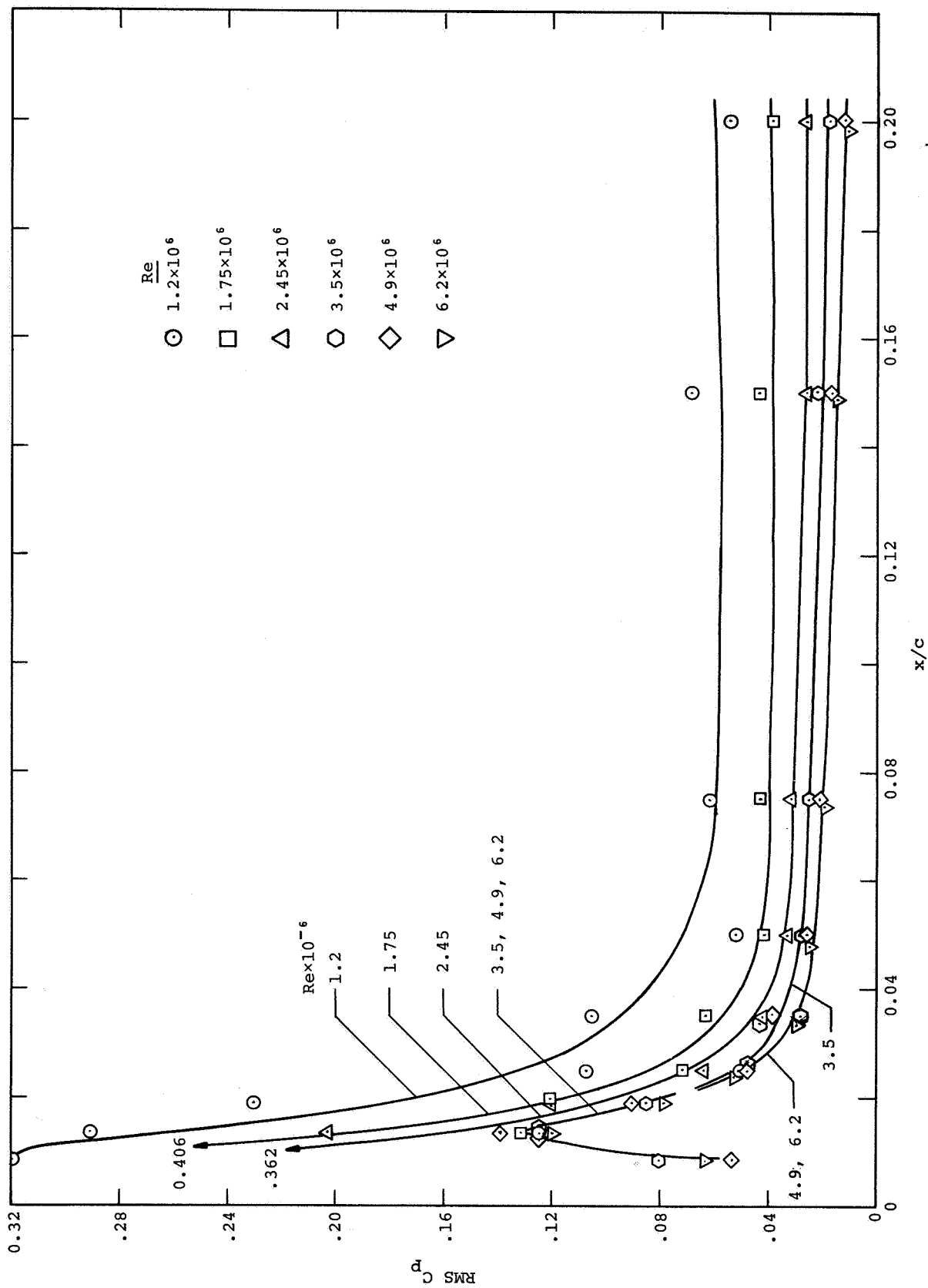


Figure 23.- Root mean square C_p along airfoil surface; basic airfoil, $\alpha = 9^\circ$.

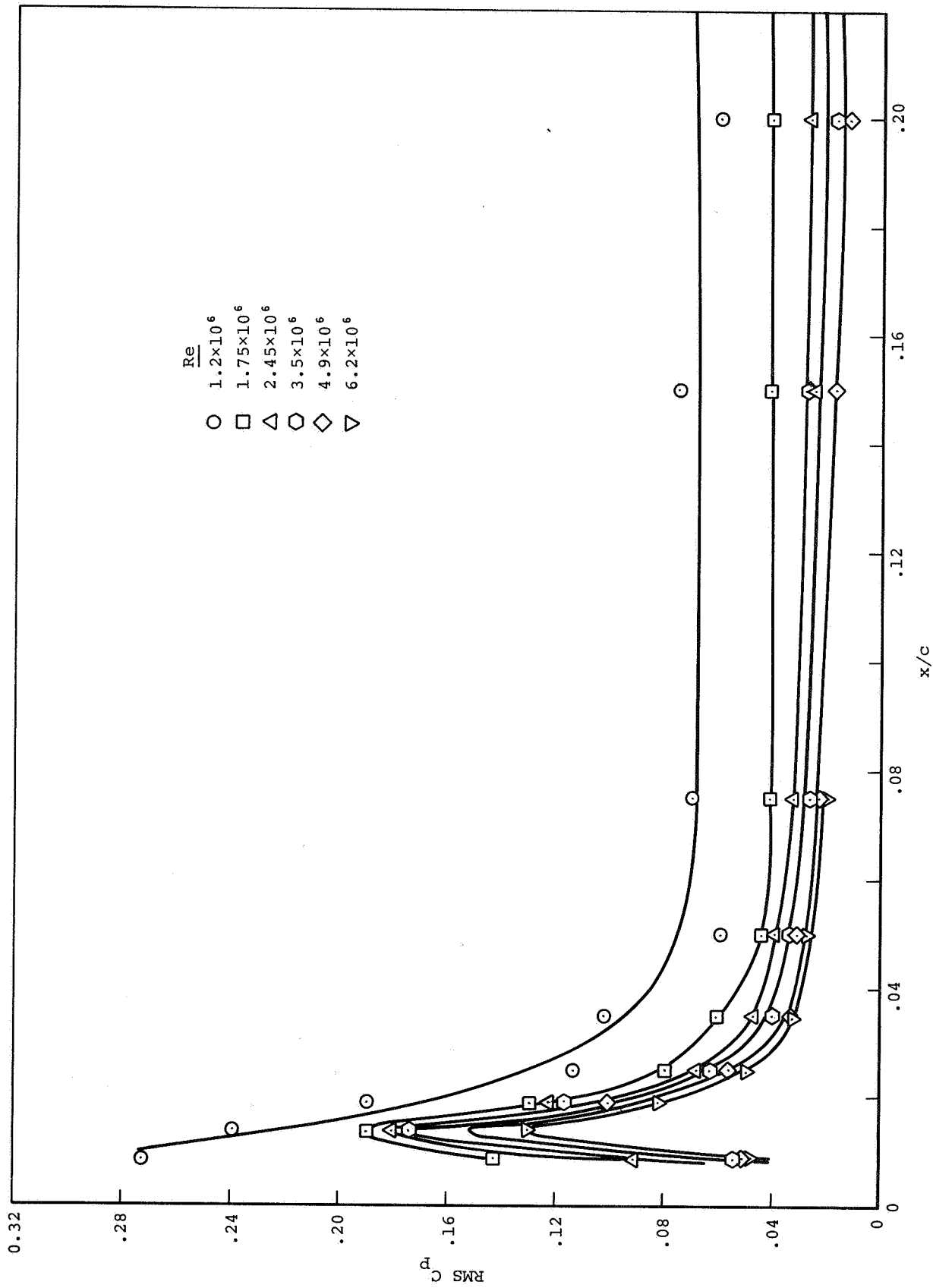


Figure 24.- Root mean square C_p along airfoil surface for serration Bl-2, $\alpha = 9^\circ$.

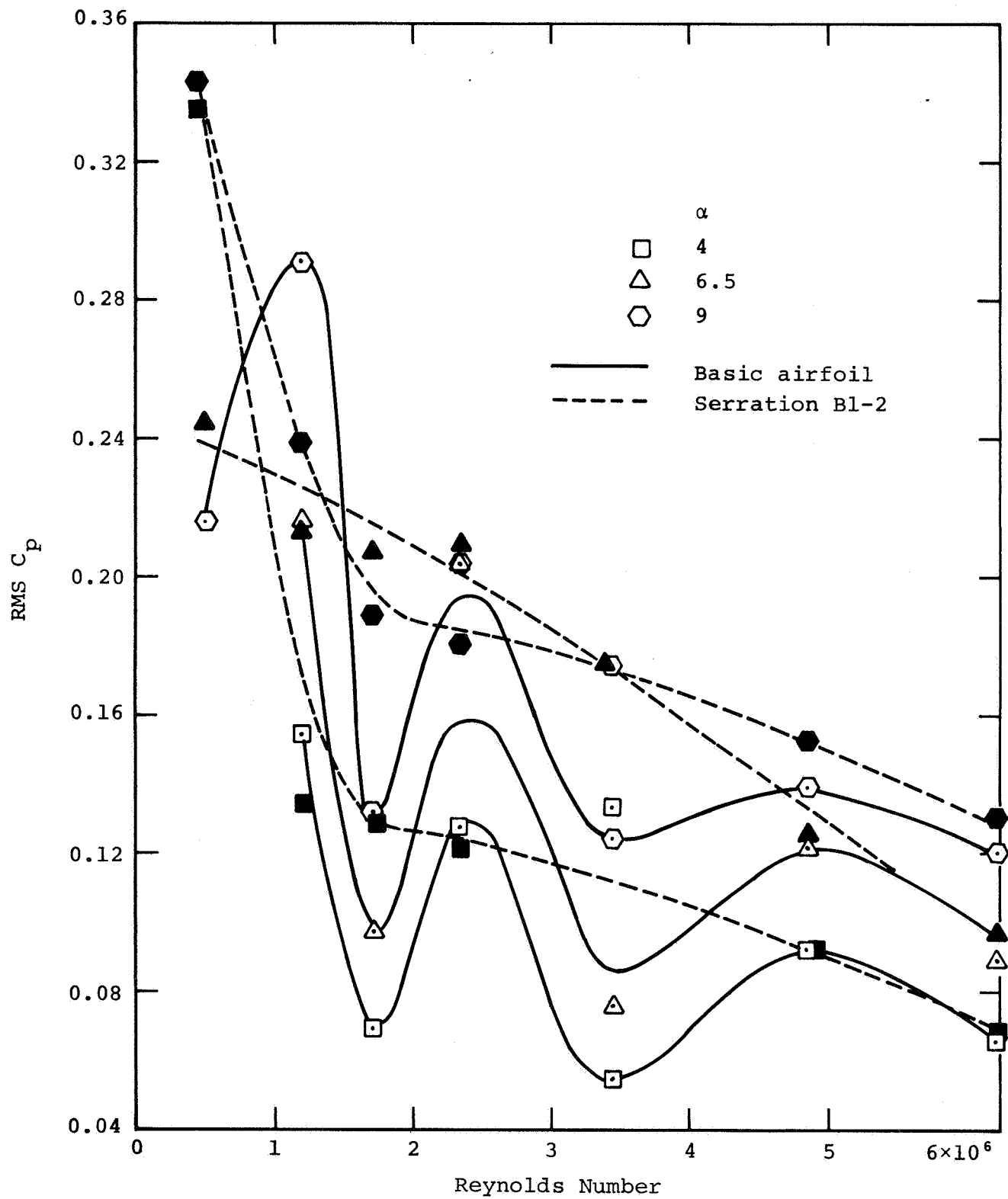


Figure 25.- Root mean square C_p at $x/c = 0.0136$ versus Reynolds Number.

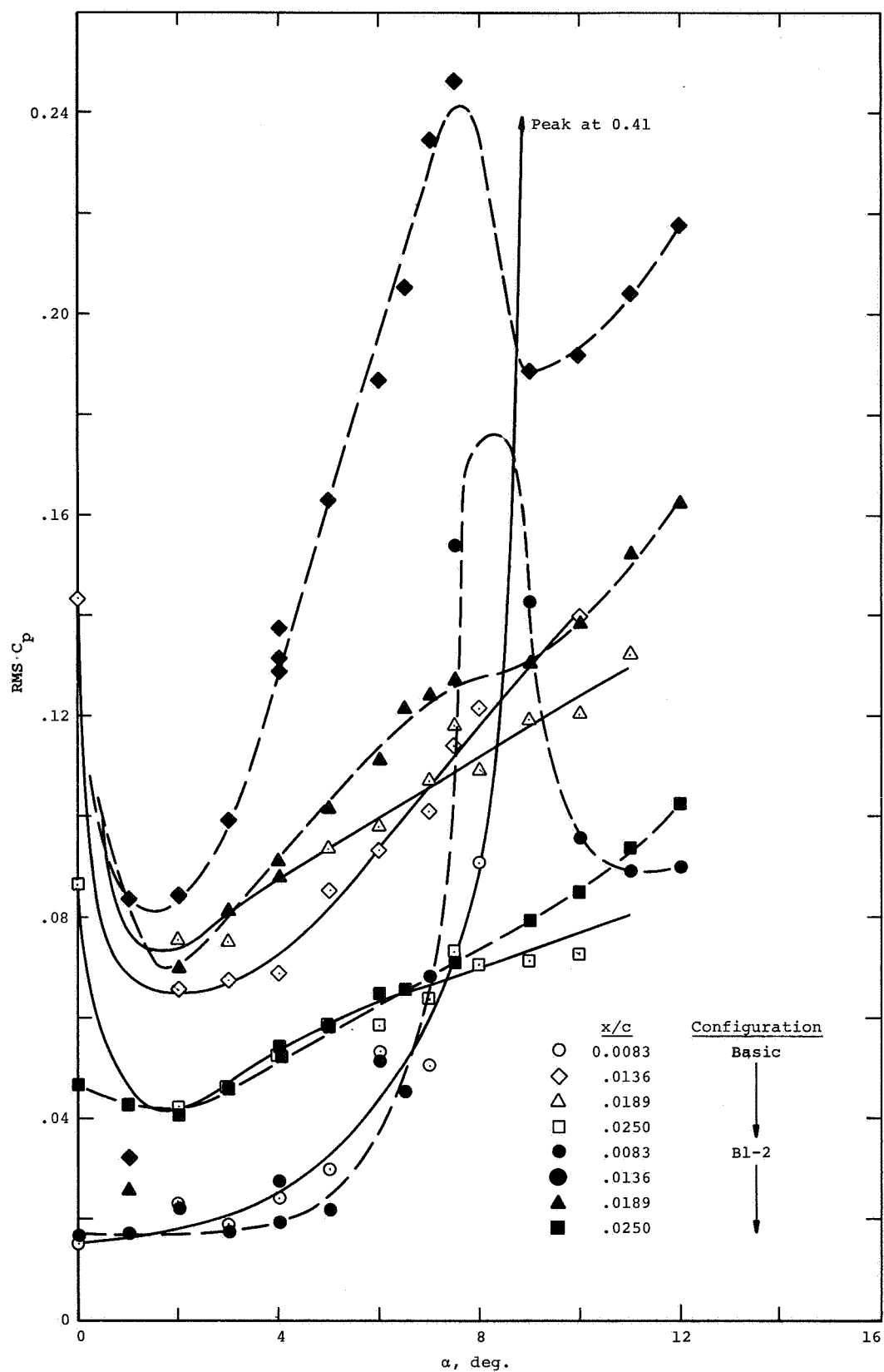


Figure 26.- Root mean square C_p versus angle of attack, $Re = 1.75 \times 10^6$.

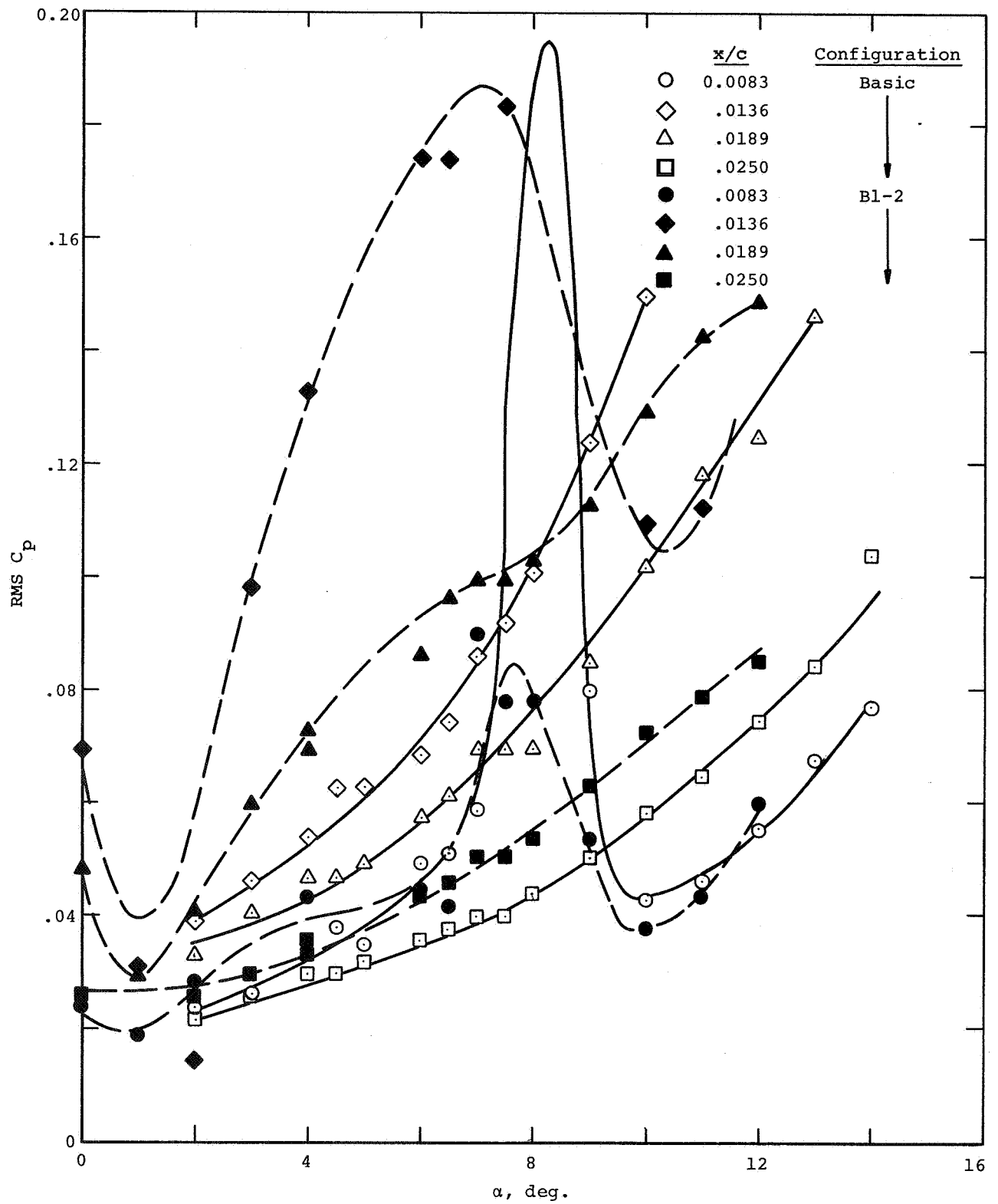


Figure 27.- Root mean square C_p versus angle of attack, $Re = 3.5 \times 10^6$.

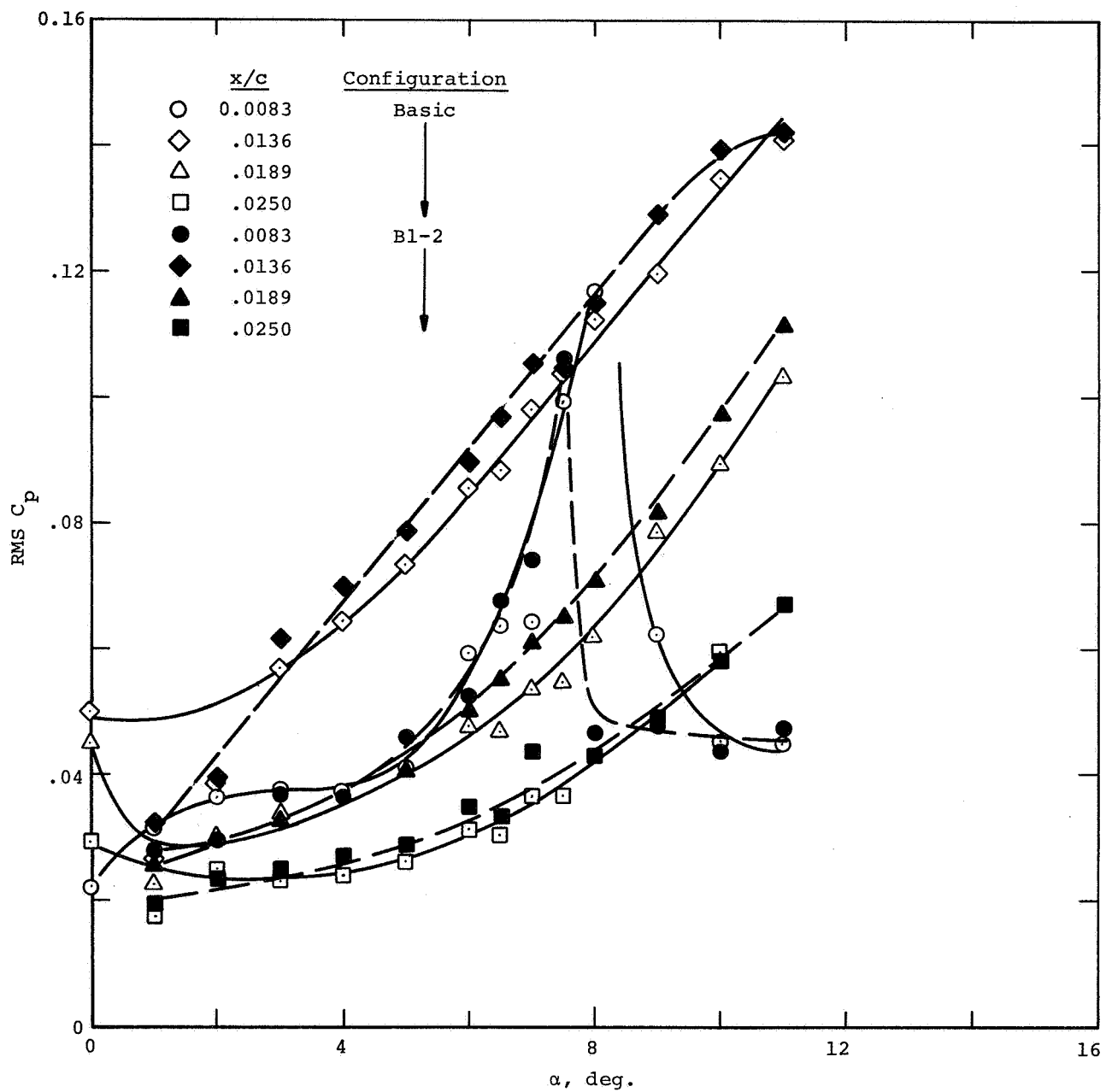
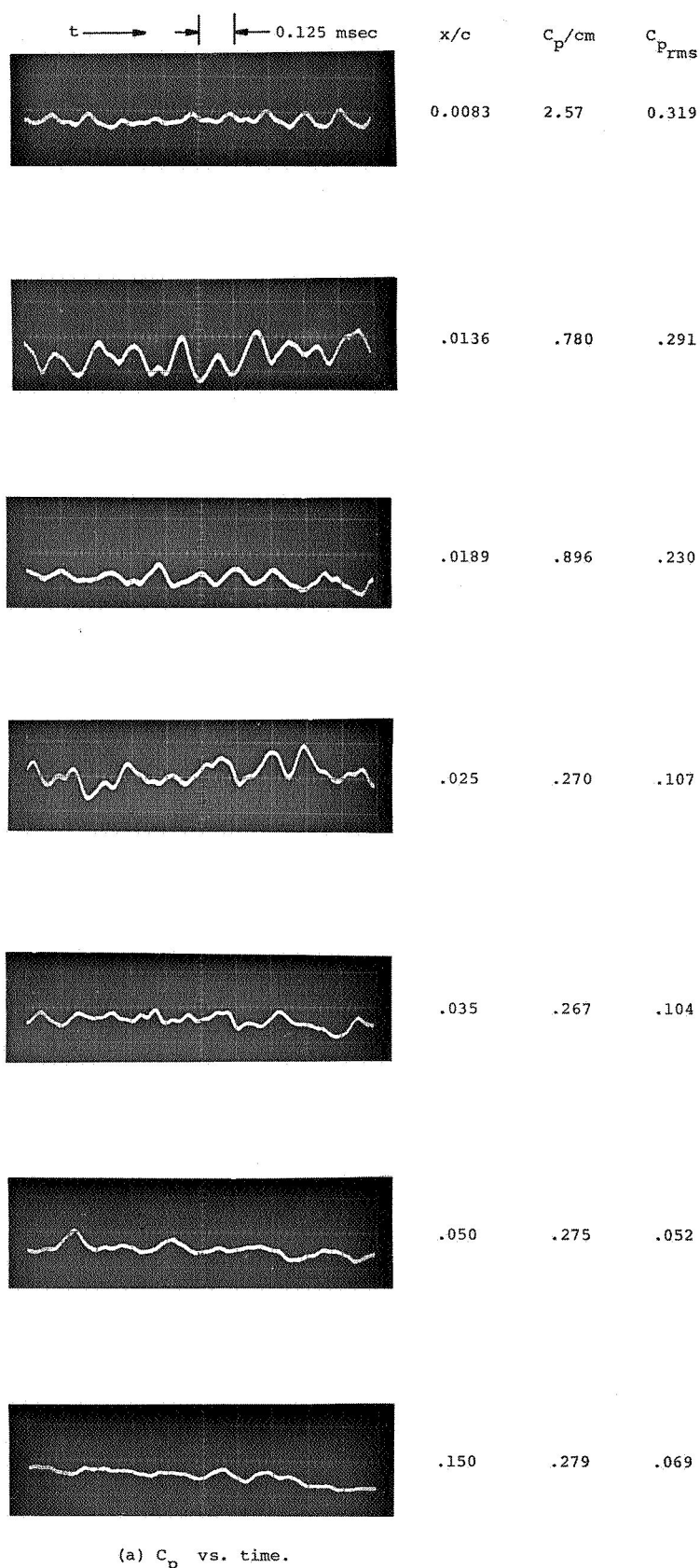
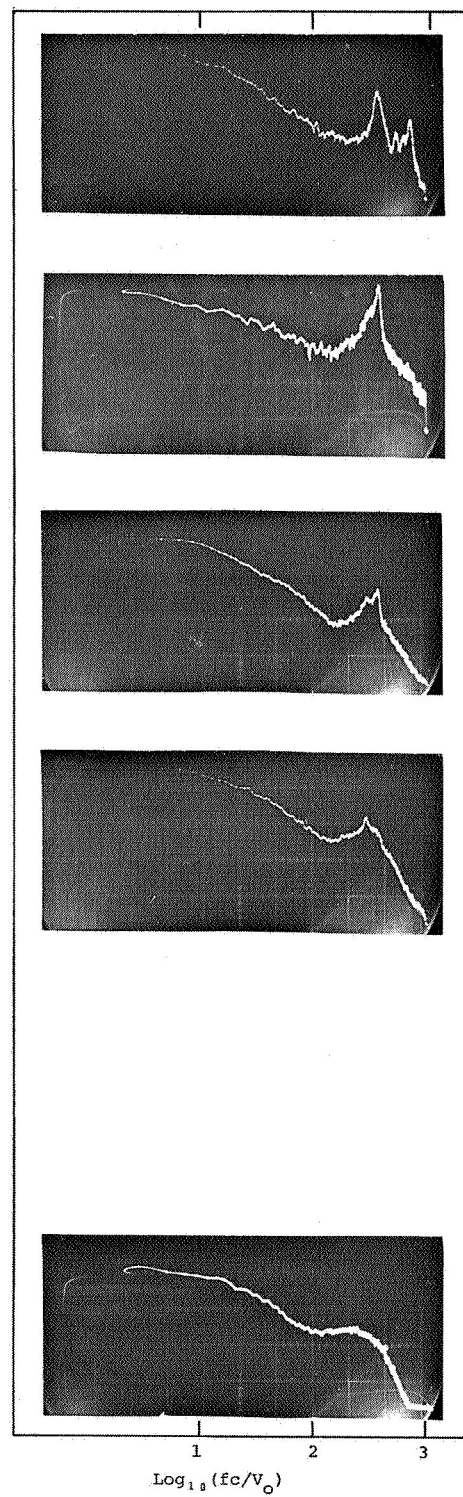


Figure 28.- Root mean square C_p versus angle of attack, $Re = 6.2 \times 10^6$.

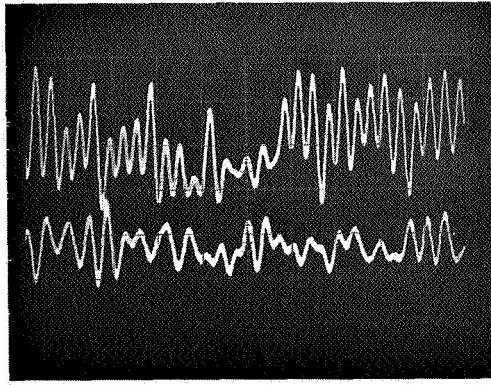


(a) C_p vs. time.



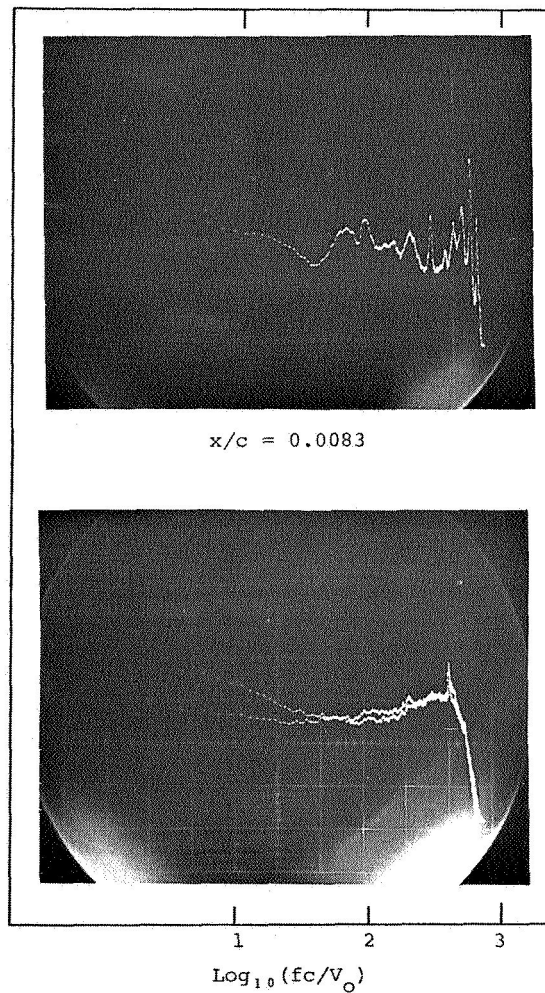
(b) Power spectra.

Figure 29.- Pressure transducer signals and power spectra on airfoil surface; basic airfoil, $\alpha = 9^\circ$, $Re = 1.22 \times 10^6$.



	x/c	C_p/cm
Upper trace	0.0083	0.680
Lower trace	.0136	.654

(a) C_p vs. time.



$x/c = 0.0083$

$\text{Log}_{10}(fc/V_0)$

$x/c = 0.0136$: Trace that is lower on left, higher on right
 $x/c = 0.0189$: Other trace

(b) Power spectra.

Figure 30.- Pressure transducer signals and power spectra on airfoil surface; basic airfoil, $\alpha = 9^\circ$, $Re = 2.45 \times 10^6$.

x/c
0.0083

.0136

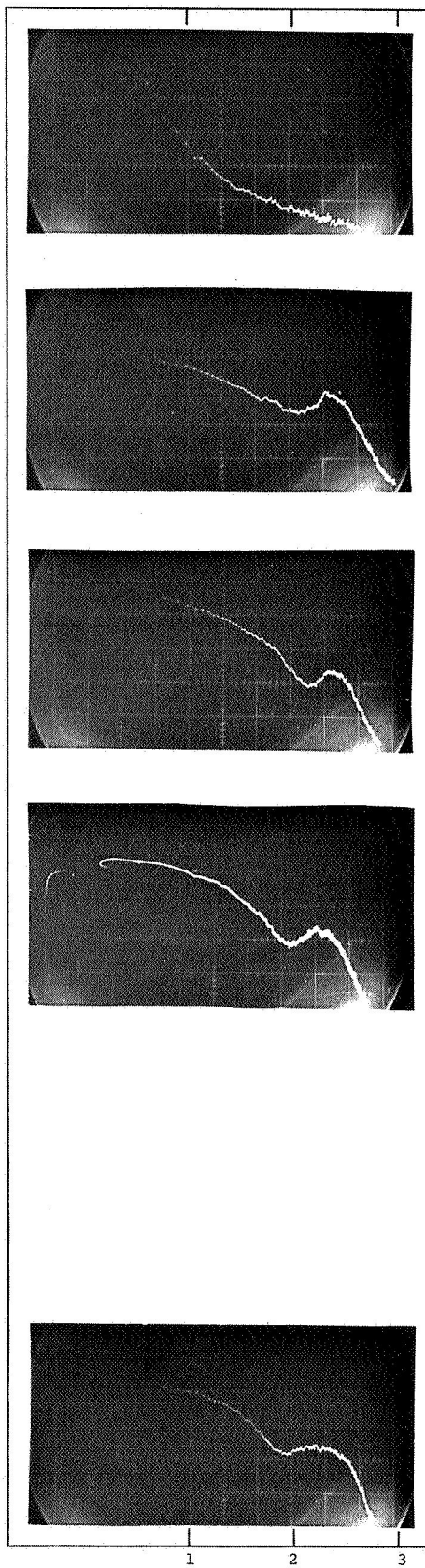
.0189

.025

.035

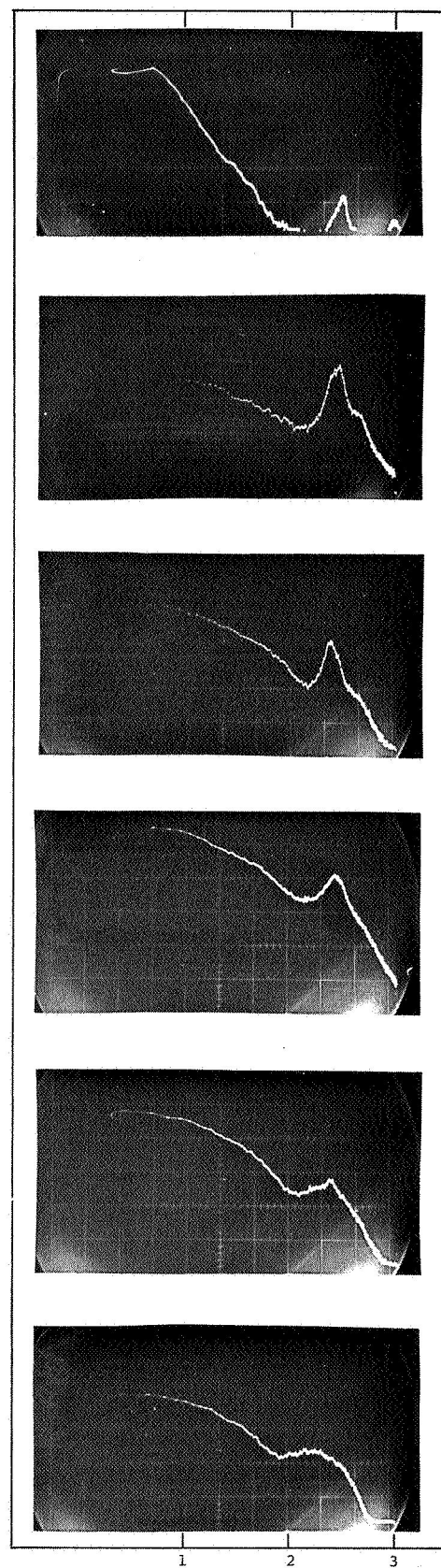
.050

$\log_{10}(4G_x/\rho^2 c V_0^2)$



$\log_{10}(fc/V_0)$

(a) $\alpha = 4^\circ$.



$\log_{10}(fc/V_0)$

(b) $\alpha = 6.5^\circ$.

Figure 31.- Power spectra on airfoil surface;
basic airfoil, $Re = 1.2 \times 10^6$.

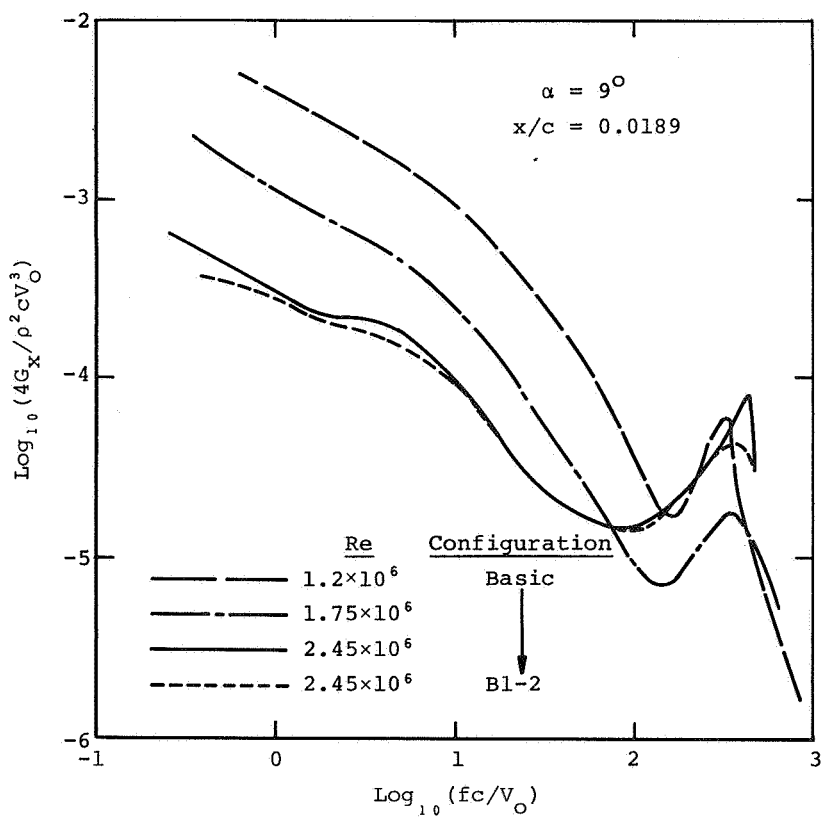
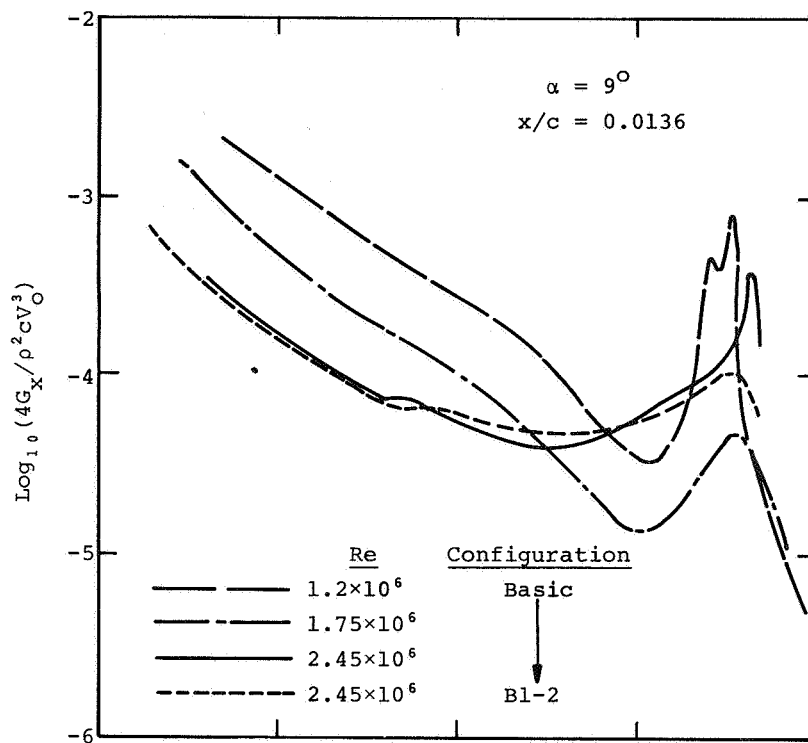


Figure 32.- Power spectra of surface pressure fluctuations.

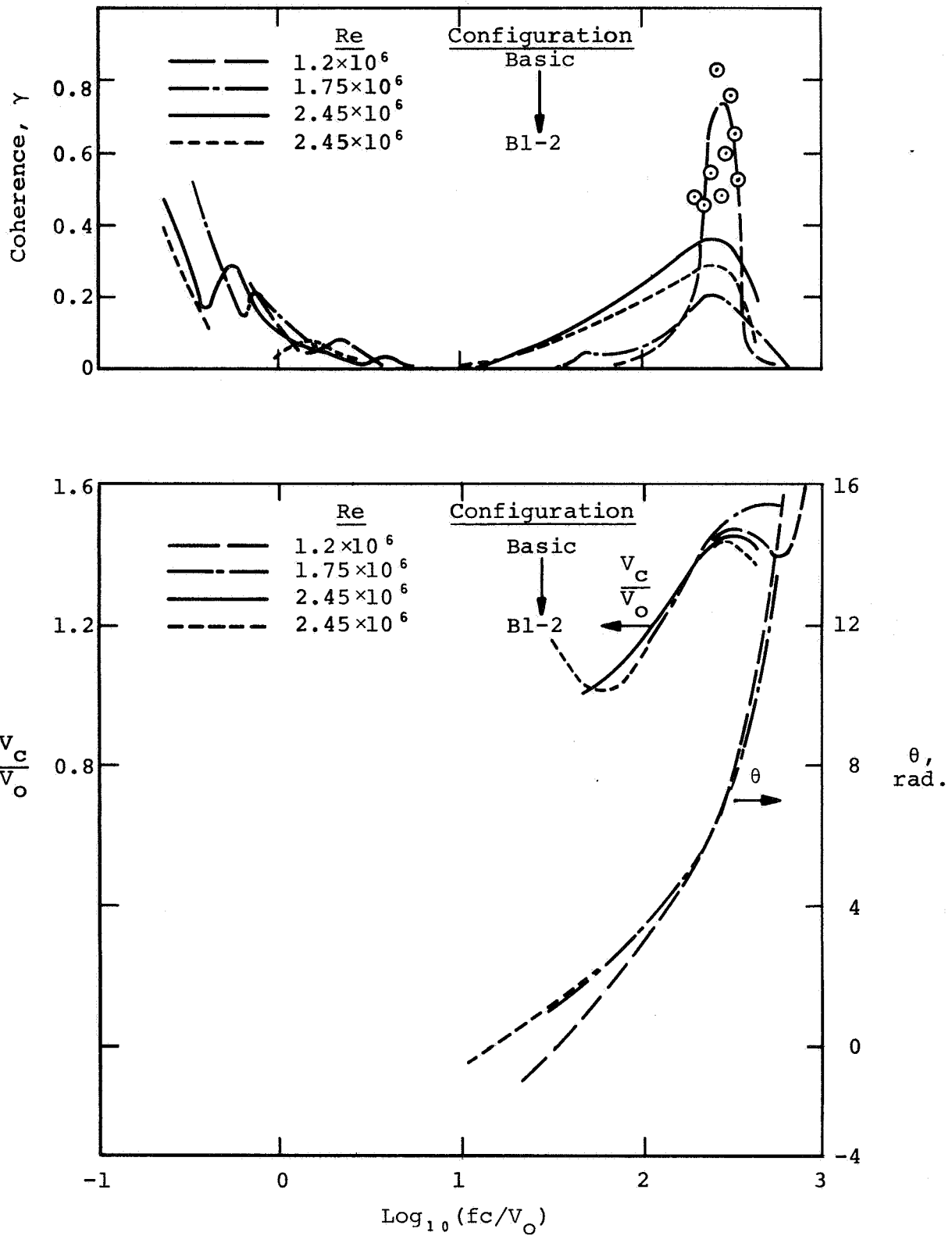
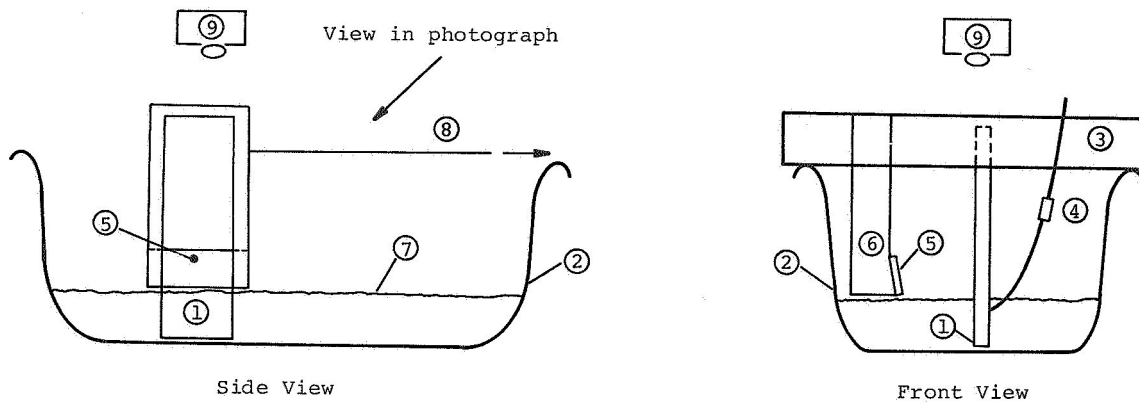
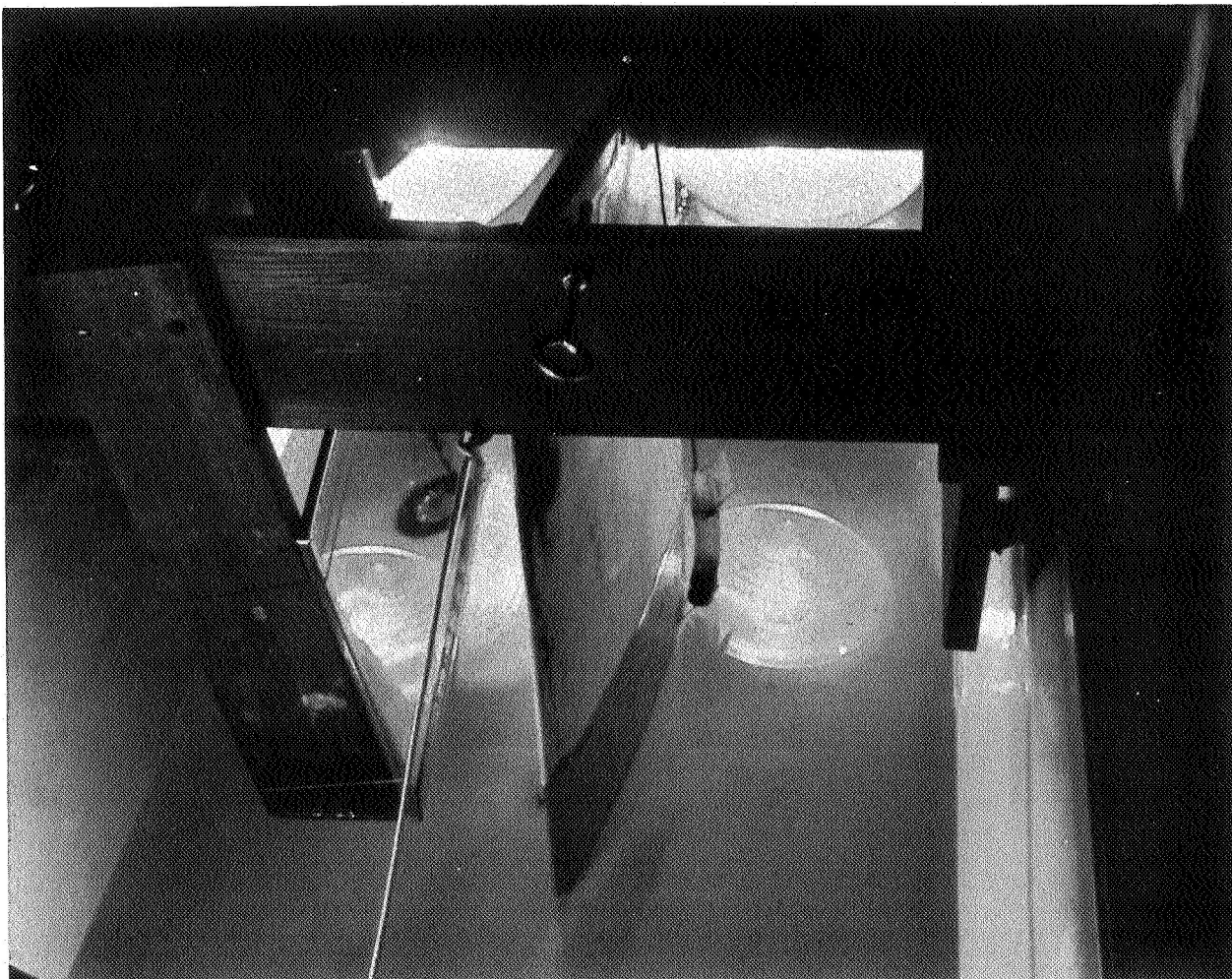


Figure 33.- Coherence, phase angle, and convection velocity between $x/c = 0.0083$ and 0.0136 .



1. Hydrofoil, suction side; 2. Bathtub; 3. Carriage frame; 4. Dye dispenser;
5. Mirror; 6. Mirror support; 7. Water surface; 8. Pull line; 9. Camera.

(a) Schematic of apparatus.



(b) Photograph of apparatus.

Figure 34.- Hydrofoil and traversing mechanism for bathtub experiment.

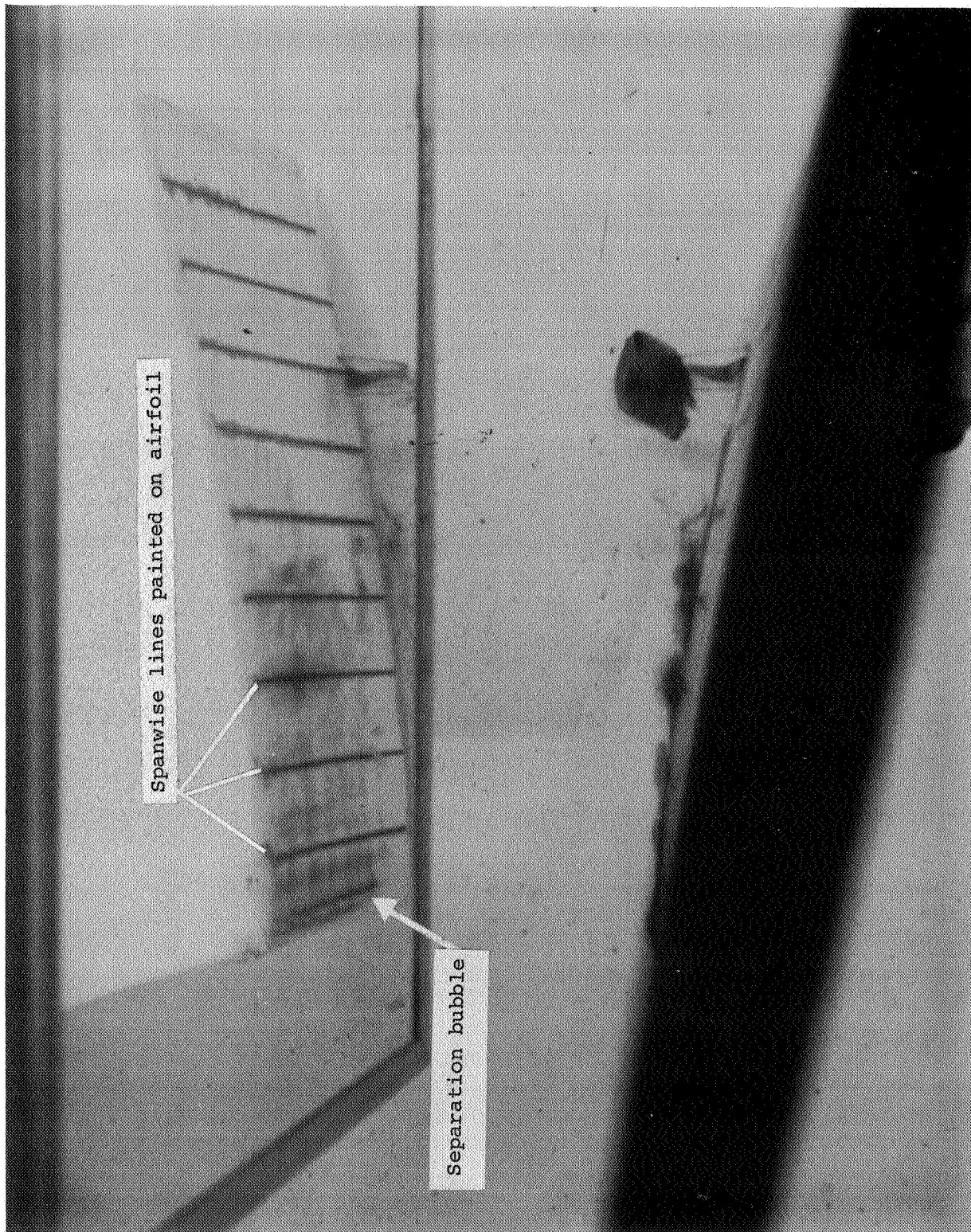
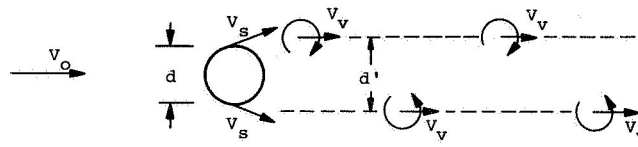
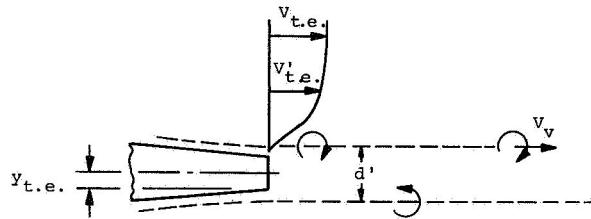


Figure 35.- Vortex shedding from basic hydrofoil.



(a) Roshko's model.



(b) Low Re trailing-edge model.

Figure 36.- Vortex shedding from a bluff body trailing edge.

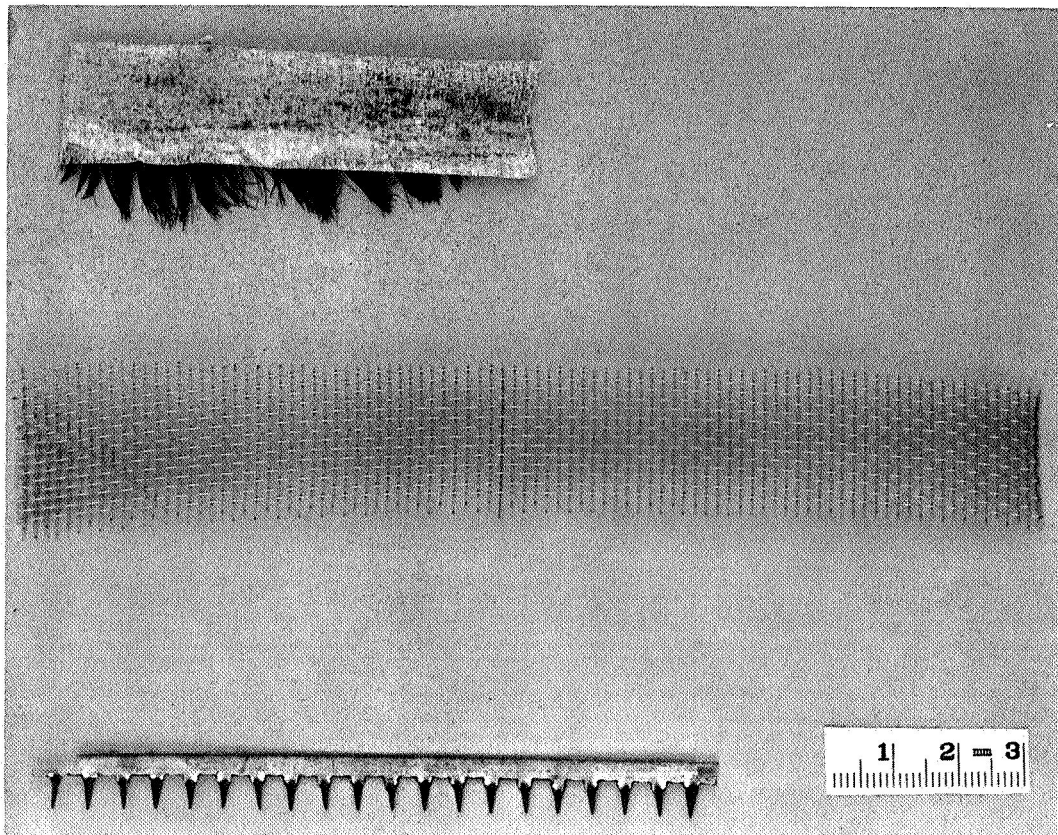


Figure 37.- Three leading-edge serrations tested.

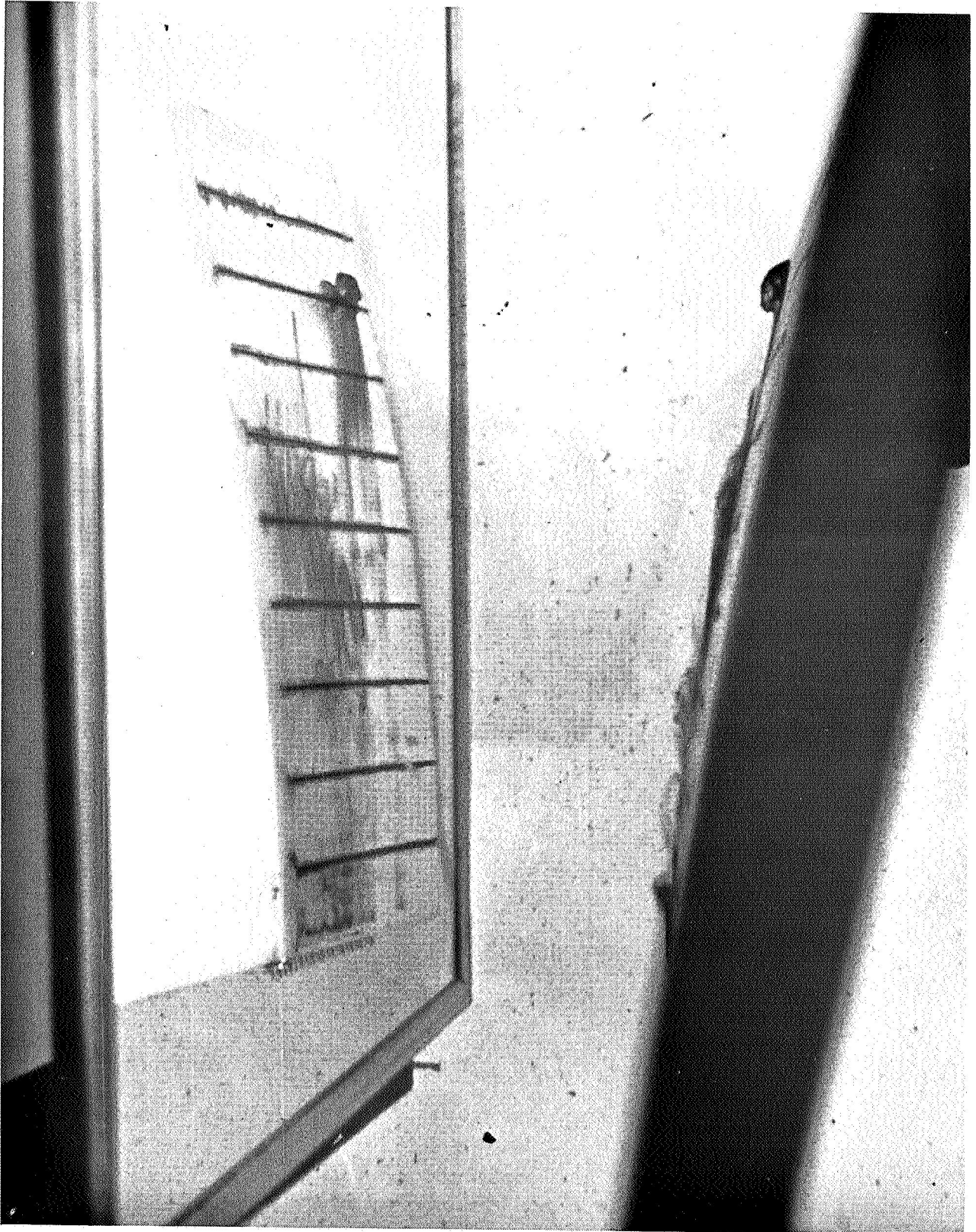


Figure 38.- Flow with V-tooth serration.

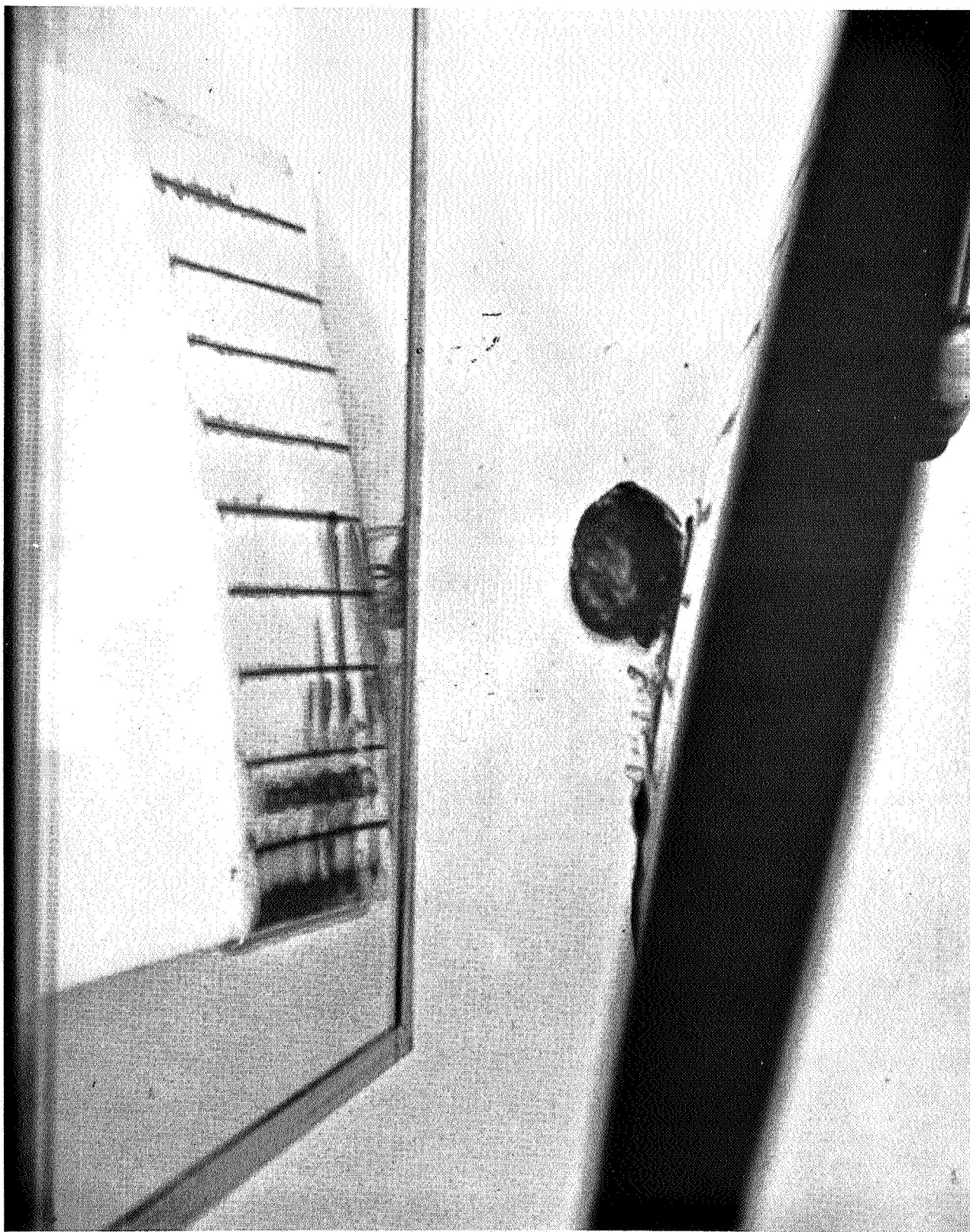


Figure 39.- Flow with wire tine serration.

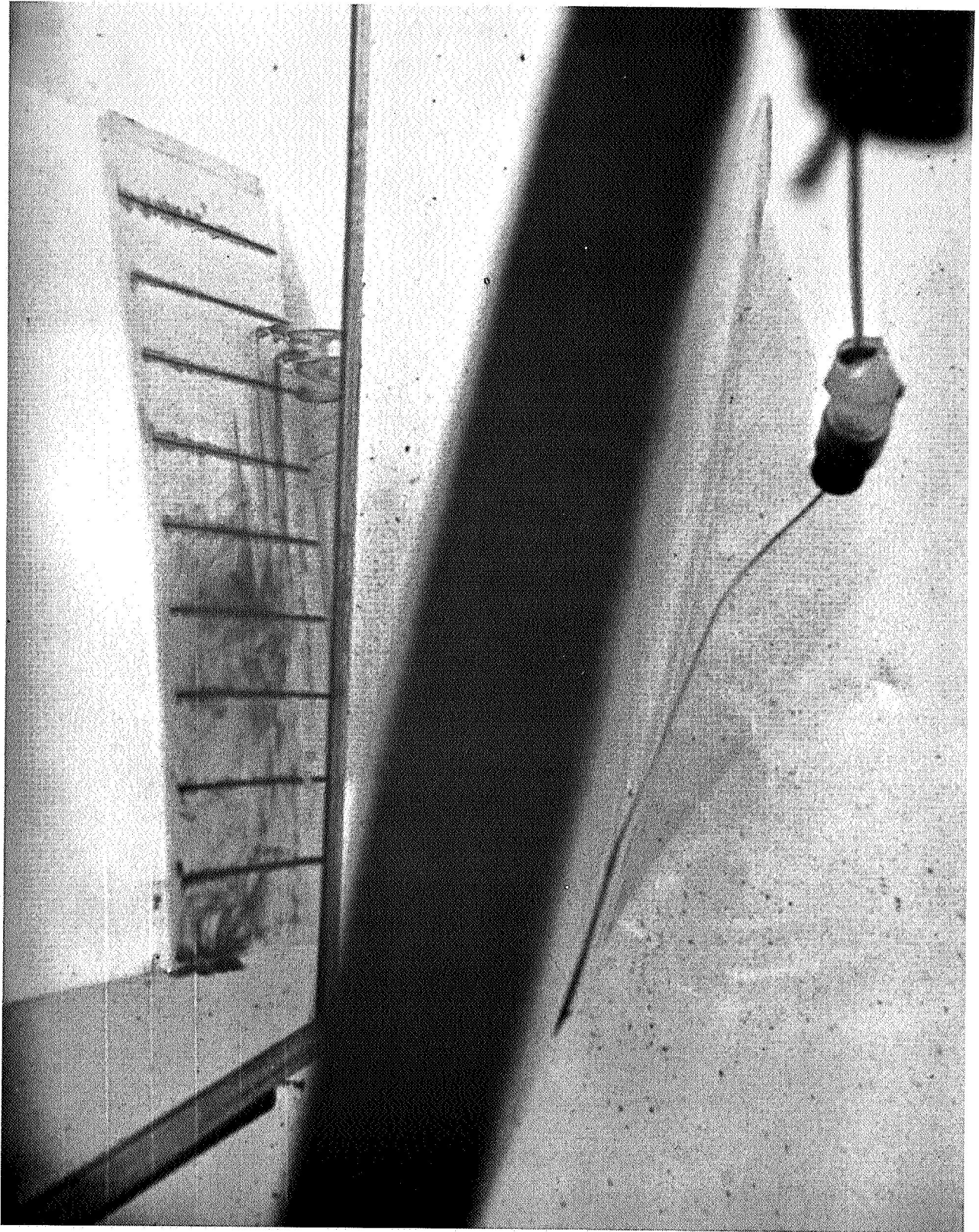


Figure 40.- Flow with artificial eyelash serration.

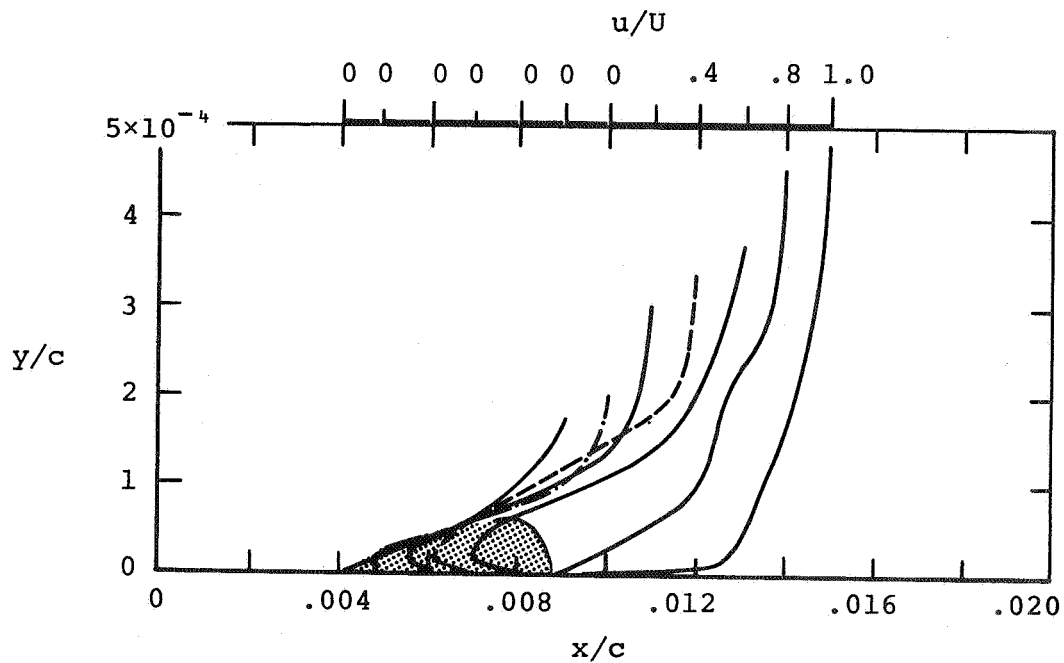


Figure 41.- Boundary-layer velocity profiles of Gault, $c_l = 0.72$.

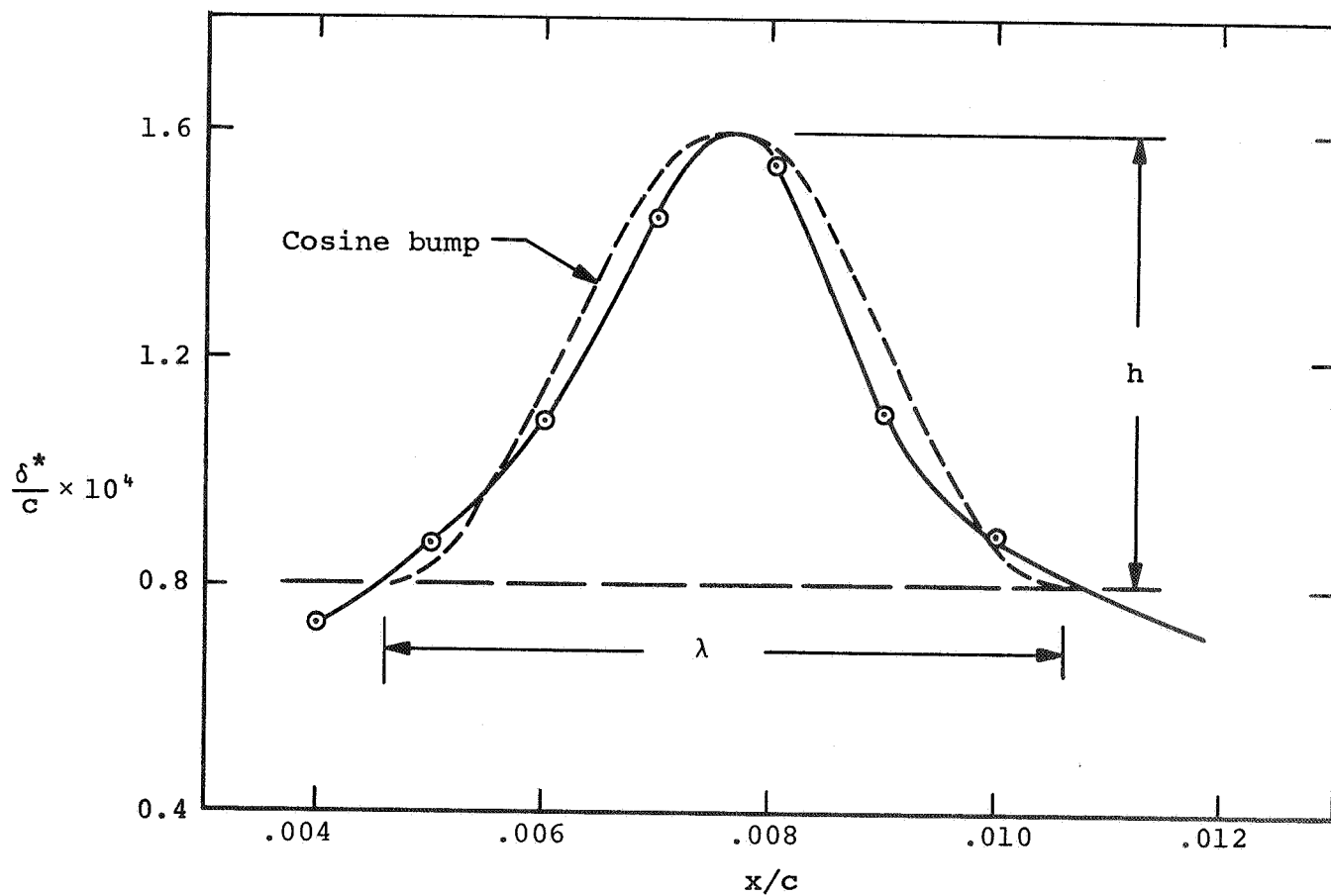


Figure 42.- Comparison of δ^* distribution with cosine bump.

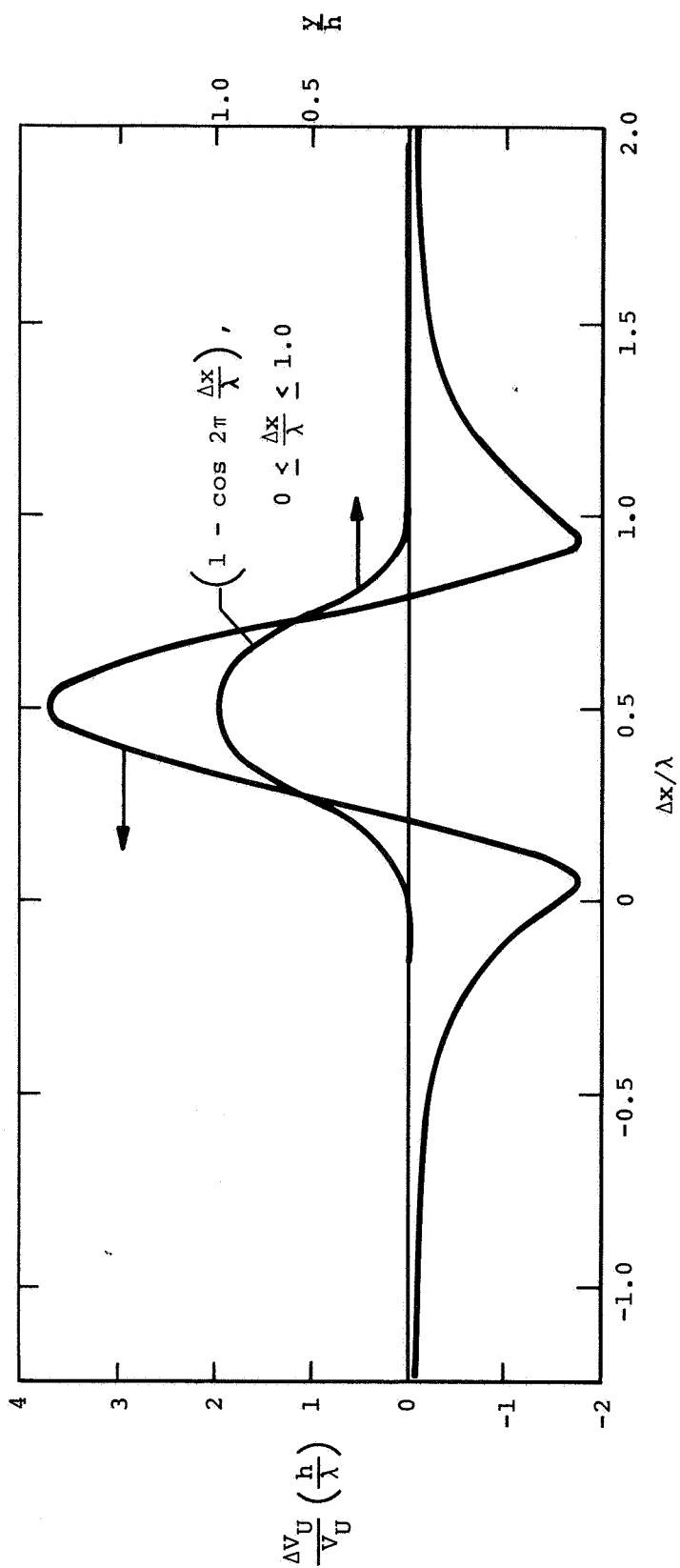


Figure 43.- Cosine bump on a flat plate and its velocity response.

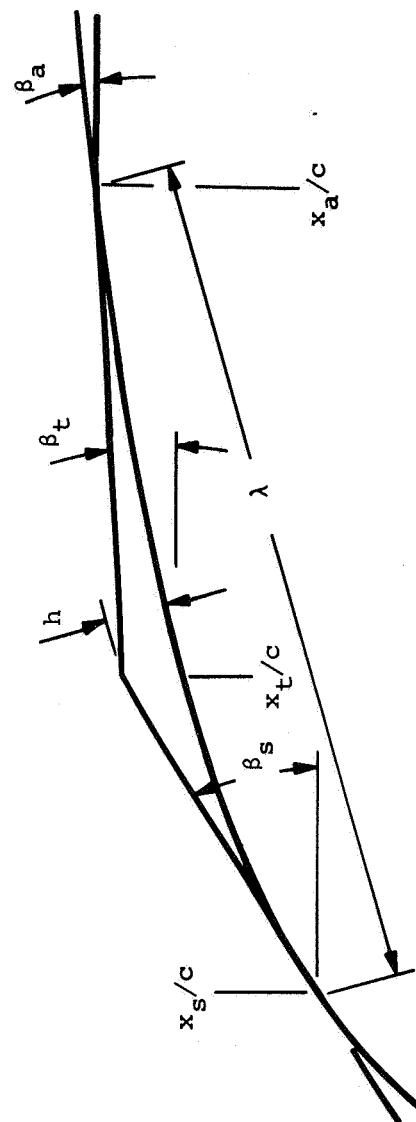


Figure 44.- Diagram of separation δ^* distribution.

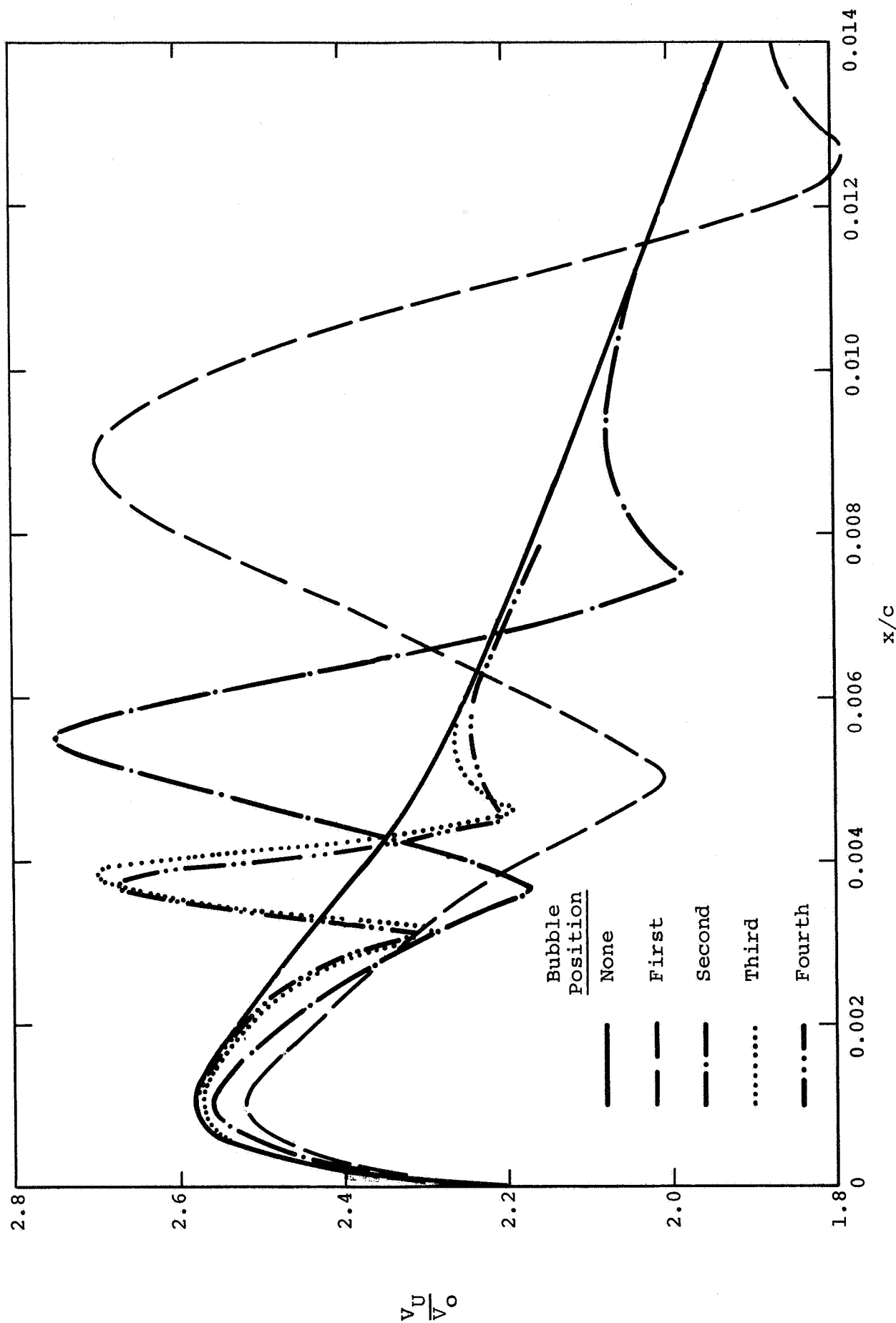


Figure 45.- Velocity distributions on NACA 63-009 Airfoil
with various bubble positions.

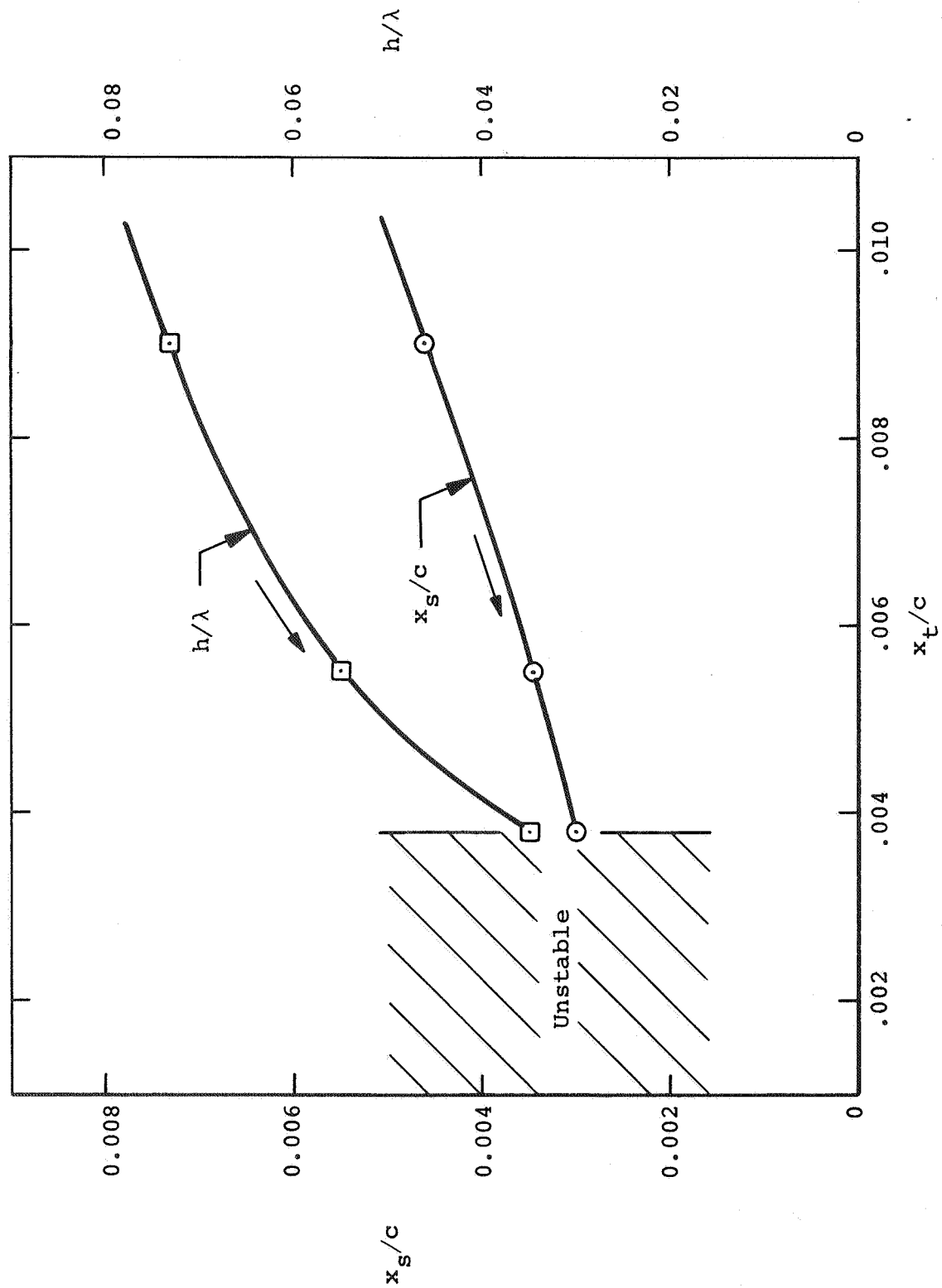


Figure 46.- h/λ and x_s/c for NACA 63-009 for assumed separation bubbles.

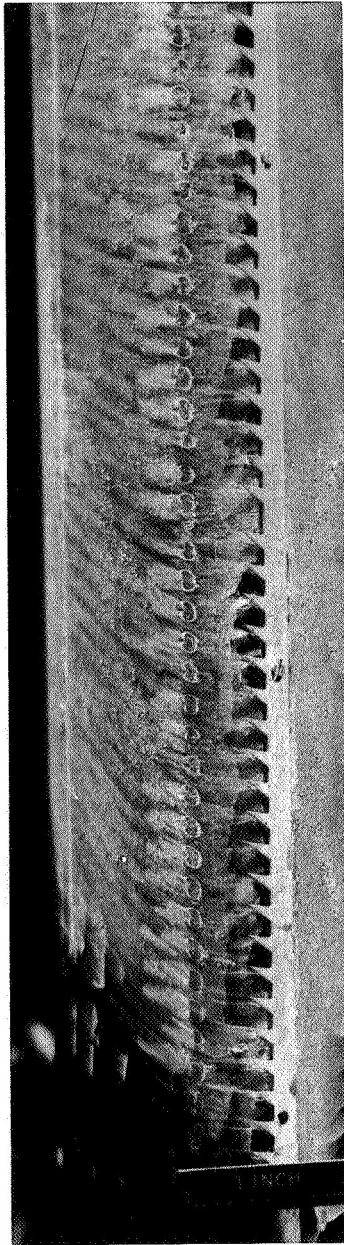


Figure 47.- Front view of NACA 66₁-012 airfoil with
serration attached. Surface flow visualization
of leading-edge region by Soderman (ref. 3).
Serration tips spaced 0.508 cm (0.2 in) and
pointed toward suction surface.
 $Re = 2.3 \times 10^6$.

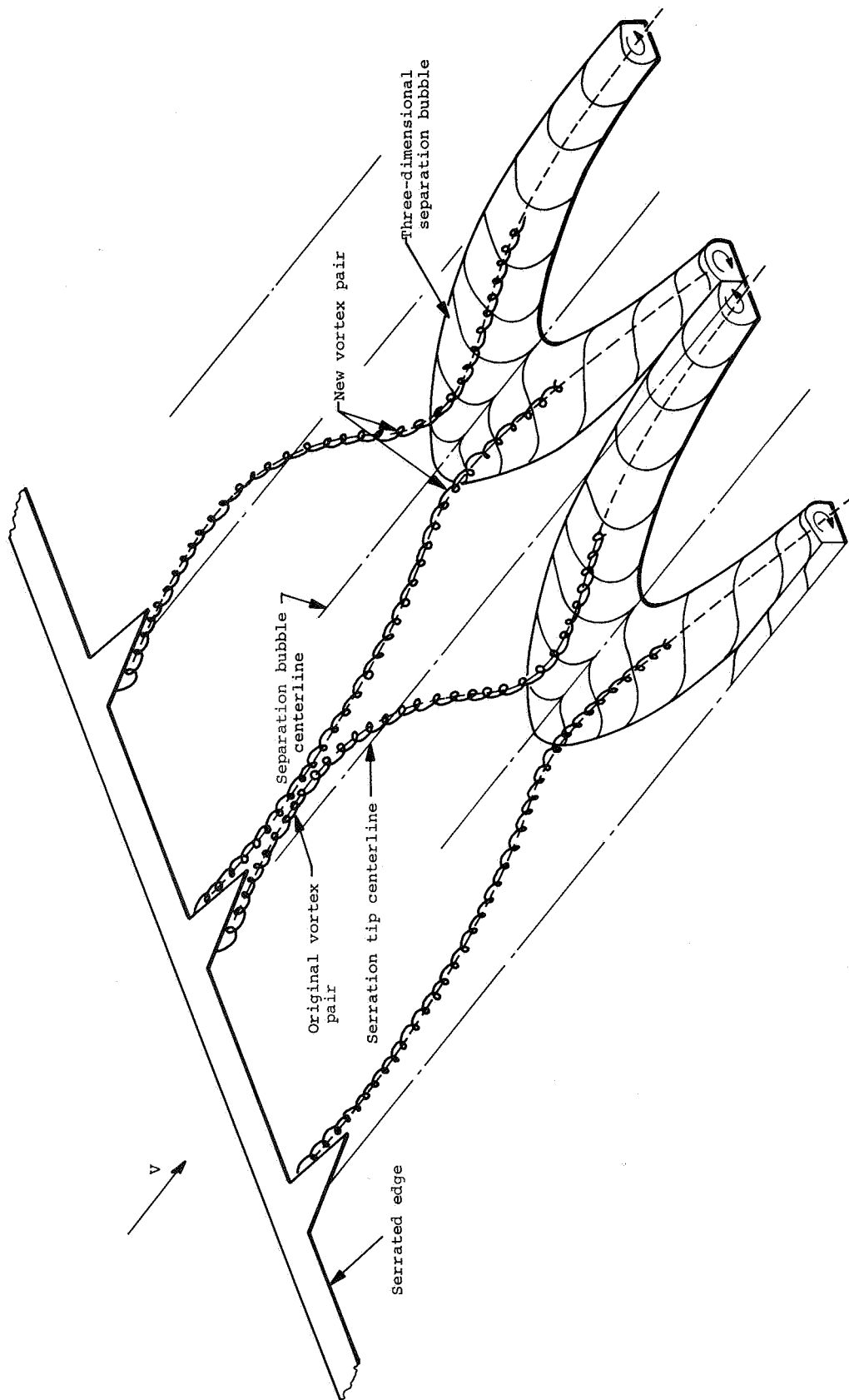
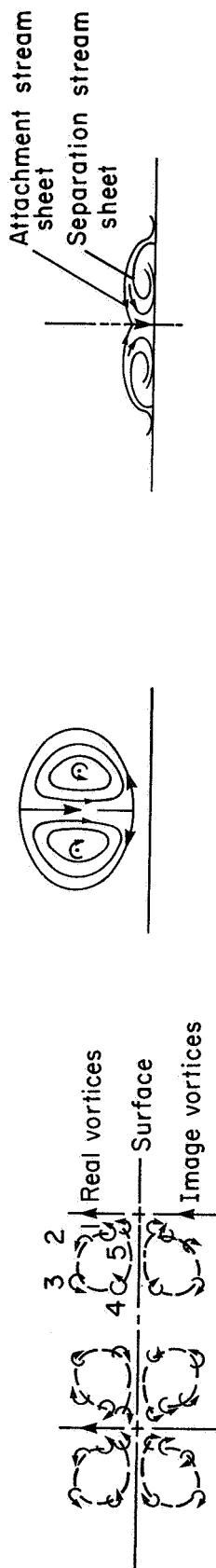


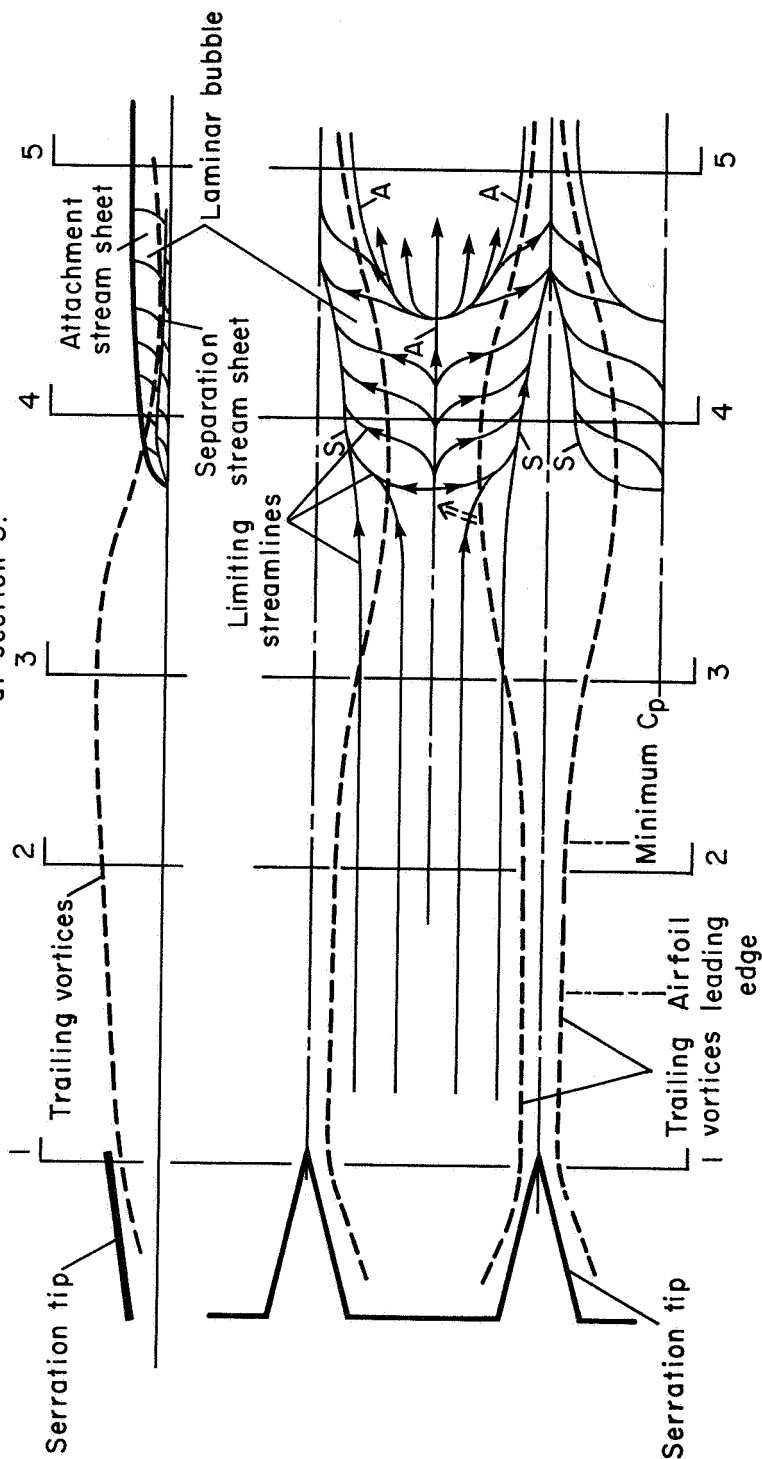
Figure 48.- Schematic of serration tip vortices and separation bubble -- overall view.



(c) End view of vortex cores.

(d) Cross section of vortices and induced crossflow at section 3.

(e) Cross section of separation bubble at section 4.



(a) Top view of vortices and limiting streamlines

Dotted arrow between 3 and 4 indicates local direction of boundary-layer vorticity.

Figure 49.- Schematic views of serration vortices and separation bubble.



POSTMASTER: If Undeliverable (Section 158
Postal Manual) Do Not Return

"The aeronautical and space activities of the United States shall be conducted so as to contribute . . . to the expansion of human knowledge of phenomena in the atmosphere and space. The Administration shall provide for the widest practicable and appropriate dissemination of information concerning its activities and the results thereof."

—NATIONAL AERONAUTICS AND SPACE ACT OF 1958

NASA SCIENTIFIC AND TECHNICAL PUBLICATIONS

TECHNICAL REPORTS: Scientific and technical information considered important, complete, and a lasting contribution to existing knowledge.

TECHNICAL NOTES: Information less broad in scope but nevertheless of importance as a contribution to existing knowledge.

TECHNICAL MEMORANDUMS: Information receiving limited distribution because of preliminary data, security classification, or other reasons. Also includes conference proceedings with either limited or unlimited distribution.

CONTRACTOR REPORTS: Scientific and technical information generated under a NASA contract or grant and considered an important contribution to existing knowledge.

TECHNICAL TRANSLATIONS: Information published in a foreign language considered to merit NASA distribution in English.

SPECIAL PUBLICATIONS: Information derived from or of value to NASA activities. Publications include final reports of major projects, monographs, data compilations, handbooks, sourcebooks, and special bibliographies.

TECHNOLOGY UTILIZATION PUBLICATIONS: Information on technology used by NASA that may be of particular interest in commercial and other non-aerospace applications. Publications include Tech Briefs, Technology Utilization Reports and Technology Surveys.

Details on the availability of these publications may be obtained from:

SCIENTIFIC AND TECHNICAL INFORMATION OFFICE

NATIONAL AERONAUTICS AND SPACE ADMINISTRATION
Washington, D.C. 20546